Hamiltonian Implementation using Photonic Coupled Cavity Arrays

Abhi Saxena

A dissertation
submitted in partial fulfillment of the
requirements for the degree of

Doctor of Philosophy

University of Washington

2023

Reading Committee:
Arka Majumdar, Chair
Rahul Trivedi, Chair
Mo Li

Program Authorized to Offer Degree:
Electrical & Computer Engineering

University of Washington

Abstract

Hamiltonian Implementation using
Photonic Coupled Cavity Arrays

Abhi Saxena

Co-Chairs of the Supervisory Committee:
Arka Majumdar
Department of Electrical & Computer Engineering, Department of Physics

Rahul Trivedi
Department of Electrical & Computer Engineering

Quantum simulators are devices made up of quantum mechanical components that can be used to study otherwise hard-to-probe quantum systems in a laboratory environment. These work by implementing Hamiltonians that accurately describe complex quantum phenomena and allow full control over the underlying parameters dictating the physics. Using photons as particles to study various physical phenomena forms the basis of some of the most promising paradigms for realizing these quantum simulators. A typical photonic quantum simulator consists of a lattice of programmable non-linear resonators, also called coupled cavity arrays (CCAs), with complete access to the Hamiltonian being simulated. While recently, numerous works on quantum simulation with microwave photons have attracted popular attention, using higher-energy optical photons can provide several additional advantages. In this thesis, we engineer photonic CCAs operating in the optical regime, which can be used for various quantum applications. For photonic CCAs to be used as quantum simulators, they need to be scalable, measurable, and controllable. In this work, we go over approaches satisfying each of these criteria.

First, we tackle the scalability requirement by demonstrating photonic CCAs implementing the Su-Schrieffer-Heeger (SSH) model describing a polyacetylene molecule. We discuss the

operation regime we need to be in for optical CCAs to be scalable to a large number of sites and use the SSH Hamiltonian as a toy model to depict the photonic design requirements that need to be met to do so. We then discuss the measurability of the realized CCAs by proposing algorithms to perform tomography of the implemented Hamiltonians by measuring only at the sites forming the outermost boundaries of these lattices. Next, we focus on adding controllability to our photonic CCAs and, to that end, develop novel thermo-optical heaters that allow us to have active control over the implemented Hamiltonian parameters. Finally, we conclude the thesis by briefly proposing a paradigm whereby, following the approach outlined in this work and utilizing the recent advancements in integrating novel quantum emitters with photonic cavities, we can realize truly scalable photonic quantum simulators.

TABLE OF CONTENTS

LIST OF FIGURES

LIST OF TABLES

ACKNOWLEDGMENTS

This thesis marks the end of my school-life. I would not have been able to make this journey without the help of a lot of people I came across during my time here. I would like to thank,

My advisor, Prof. Arka Majumdar, for being a wonderful guide and giving me the freedom to explore any new idea I wanted. He was always available for help, and his hands-on approach made transitioning into a research work environment straight out of undergrad very straightforward.

Yueyang Chen from whom I got introduced to fabrication, material integration, and optics lab experiments. I enjoyed our chats we had in office and in lab while measuring umpteen samples.

David Rosser and Albert Ryou for helping me get up to speed with lab culture and quantum optics when I joined the group.

Maksym Zhelyeznyakov and Zhuoran Fang who joined the group with me. Starting as officemates together, we had a lot of great conversations over the years.

James Whitehead who was the first person I met when I arrived here in the US. He picked me up from the airport and turned out to be one of the nicest people I know. He helped me move between apartments and later became my officemate before he graduated.

Arnab Manna, who joined our group when I was in my third year. He has been a constant companion ever since. From the clean room, where we pulled several late-nighters, to our office, where we had our grumpy sessions about new problems arising in one of our projects. Our weekly trips to Trader Joes to pick groceries became habitual, and I wish him the best in his project.

Johannes Fröch who joined our group as a post-doc right after Covid and became my

officemate, He educated me a lot about culture in academia and diversified my outlook on research. His persistence and work ethic have helped shape me as a researcher, and it is something I will carry with me going forward.

Rui Chen, Zheyi Han and David Sharp for being wonderful group mates.

Prof. Rahul Trivedi, who with his expertise in quantum optics, helped me tackle a theoretical problem I had grown interested in during the latter stages of grad school and became my co-advisor. Rahul is one of the most brilliant researchers I know, and he has played a significant role in shaping me as a researcher since my undergraduate days.

Erfan Abbasgholinejad from Rahul's group, with whom I had great fun on our trip to Denver and on our theory project.

Prof. Mo Li for being my committee member and recommending me for a number of awards/positions.

Bingzhao Li from Prof. Mo's group, whom I got to know over time. He helped me smooth my fab flows in the clean room, and we had great discussions over almost everything in grad school. I wish him the best for his career ahead.

Forrest Miller and Hannah Rarick for all their efforts in making my routine in Seattle a lot more fun, teaching me about American culture, and our daily crossword sessions.

Akshit, Utkarsha for being the best of friends over the years, and Hobbes for being there to cheer me up on the most distressing days in grad school.

Most of all, I would like to thank my parents and brother for their support for the longest time. My grandparents, who were always supportive, and, at the end, Fufu, for guiding me in life.

Chapter 1

INTRODUCTION

1.1 Overview

Solid-state materials consist of lattices of atoms arranged at fixed locations, which create an electrical potential profile for the electrons to hop around. Since, electrons are fermionic and negatively charged, they experience both short- and long-range interactions when moving around, making these systems highly correlated. To study these solids and their underlying physics or to engineer new materials with unique properties, we need to simulate these systems. However, simulating these on classical computers becomes intractable as the size of the underlying lattices increases. Hence, there exists a need to realize devices that are specifically designed to simulate such systems. We know that a system's Hamiltonian describes its eigenenergies and the evolution of its quantum state according to the Schrödinger's equation [1]. Therefore, we need devices that have the capability to implement a variety of desired Hamiltonians.

This is where quantum simulation comes in. Since we are wanting to simulate physics at the single electron and atomic level, we are squarely inside the quantum regime. Hence, in his paper [2], Richard Feynman suggested that to efficiently simulate these systems we need computers that are themselves build with quantum mechanical components. Typically, these devices are now called quantum simulators.

Quantum simulators are scalable, measurable and controllable devices that are used to implement Hamiltonians to study other quantum systems which are otherwise hard to probe experimentally. Several platforms have been used to demonstrate prototypical quantum simulators [3] including laser-trapped cold atoms [4], scalable ion traps [5,6] and photo-detection based photonics [7]. However, the platform that has attracted the most attention recently

to realize quantum simulators is the superconducting coupled cavity arrays operating in the microwave regime [8–11].

1.2 Coupled Cavity Arrays

Coupled Cavity Arrays or CCAs are one-dimensional ($1D$) or two-dimensional ($2D$) lattices of coupled resonators which typically operate in superconducting microwave or optical domain (Fig. 1.1). These can be accurately described by the following Hamiltonian:

$$H = \sum_{v} \mu_v a_v^\dagger a_v + \sum_{v,u} J_{v,u} a_v^\dagger a_u \tag{1.1}$$

where a_v ($a_v^\dagger$) denotes onsite photonic destruction (creation) operator, μ_v denotes the onsite potential which is equivalent to the resonant frequency of the resonator and $J_{v,u}$ denotes the hopping rate between sites v, u which is equivalent to the coupling strength between the pair of resonators.

Additionally, these CCAs can be engineered in case of superconducting systems/integrated with emitters in case of optics to realize non-linear Hamiltonians, for example, of the form:

$$H_{nl} = H + \sum_{v} \frac{\chi_v}{2} a_v^{\dagger 2} a_v^2 \tag{1.2}$$

where χ_v denotes the onsite non-linearity. Depending on the relative values of these quantities namely the μ's, the J's and the χ's; the CCAs can be engineered to mimic various physical systems by providing a tailored environment for photons to move around the lattice. This makes them an ideal platform for both classical and quantum simulation.

In fact, both optical and superconducting microwave CCAs have been used to demonstrate various classical phenomena like Anderson localization [12] and hyperbolic lattices [13]. Recently, to popular success, these have also been used to simulate various topological phenomena including, but not limited to, demonstration of: topological phases in $2D$ optical lattices [14], the Su-Schrieffer-Heeger model [10, 15], topological semimetals [16], strained graphene model [17] and topological lasing [18].

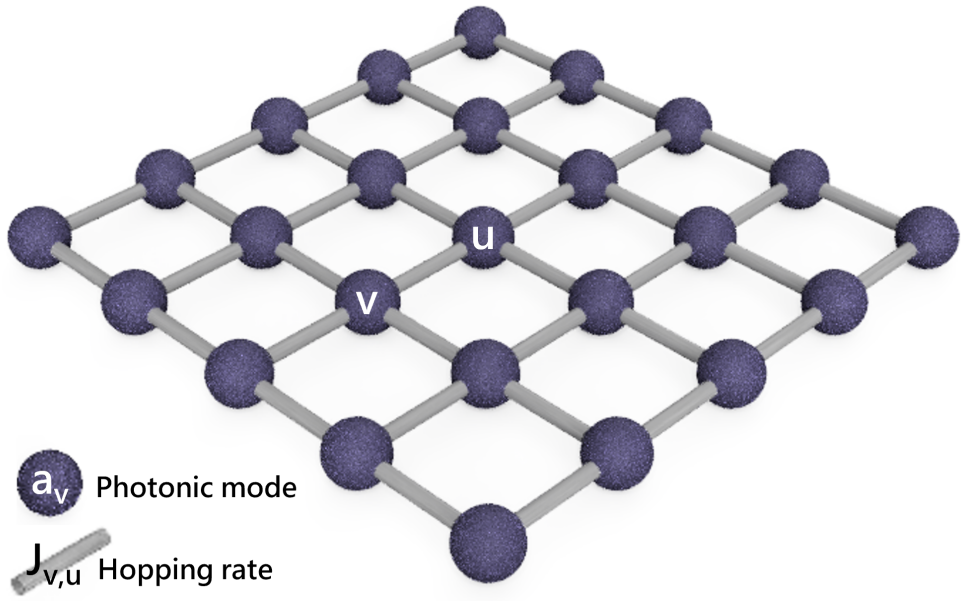

Figure 1.1: Schematic depicting a CCA. Each cavity forming the lattice and it's corresponding photonic mode is denoted by a purple node. The gray bars depict the nearest neighbor coupling strengths or equivalently the hopping rates $J_{v,u}$ between any two sites v, u in the lattice.

However, when it comes to quantum simulation only superconducting microwave coupled cavity arrays have been successful in simulating quantum physics like localization of interacting photons [8], Mott insulators [9] and Bose-Hubbard model with long range hopping [11].

1.3 Motivation

In this thesis, we want to lay the foundation for realizing quantum simulators using photonic CCAs. The first question that naturally arises is why do we want to use photonics? This is because integrated photonic circuits can provide several advantages over the superconducting systems, namely:

(a) Photonic performability at higher temperatures: The higher energy of optical photons

means that they can retain their quantum state [19] at much higher temperatures than the cryostat bound superconducting microwave circuits. This significantly eases the experiment and reduces the cost of building the system.

(b) Scalability: While superconducting CCAs have been used to demonstrate prototypical quantum simulators, these are typically restricted to a maximum of few 100s of sites. Though these sizes are okay for proof of principle demonstrations, in order to actually simulate a material and its properties we need quantum simulators with a lot larger number of sites. Access to mature foundry processes leveraging on the immense advancements made in the electronic fabrication means that photonic integrated circuits can be scaled to truly large sizes and number of sites [7, 20]. Combined with a possibility of not operating at cryogenic temperatures, small size and high speed of operation, nanophotonics presents one of the most promising pathways to scale to "practical quantum advantage" [21].

(c) Availability of single photon detectors: As optics has access to single photon detectors, we can measure single/multi particle correlations directly during experiments [22]. As these are a key set of experiments that allow to determine the quantumness of the realized state, this denotes a fundamental advantage that optics enjoys over microwave photon based circuits.

1.4 Outline

Despite the promise that photonic integrated circuits present, there are some key challenges that need to be addressed before we can utilize these for quantum simulation. Briefly, realization of photonic analog quantum simulators depends on realization of photonic CCAs that satisfy the following criteria of:

(i) Scalability: scalable to a large number of sites,

(ii) Measurability: ability to map the realized Hamiltonian with limited access,

(iii) Controllability: control over optical cavities while ensuring minimal additional losses,

(iv) Optical non-linearity: access to non-linearity.

Hence, firstly, we need to figure out pathways to scale photonic CCAs so that these are suitable for quantum simulation and are not limited by inherent nanofabrication disorder

commonly associated with solid-state devices. We address this issue in Chapter 3. Then in Chapter 4, we discuss protocols that can be used to characterize the Hamiltonians being implemented by the photonic CCAs. However, as photonic integrated circuits are confined in a $2D$ plane and hence allow reliable, accurate and scalable access to only the boundaries of the devices, we need algorithms that enable tomography of the realized Hamiltonians by measuring at sites forming the outermost perimeters of the photonic CCAs. Another major challenge faced while using photonics is the programmability of the realized devices. While the photonic cavities making the CCAs are great for confinement of photons for long durations in small physical dimensions, hence allowing access to strong light-matter interaction, the extremely confined nature and small sizes make it very hard to control their characteristics actively during operation. In Chapter 5 we demonstrate one approach based on thermo-optic tuning to achieve this controllability. Finally, in the last chapter, we discuss how, by following the approach outlined in the thesis and leveraging the advancements made in the integration of synthesized quantum emitters, color centers, etc., we can develop an approach towards realizing truly scalable and useful photonic quantum simulators. However, before delving into the subject, in Chapter 2, we begin with a short introduction about racetrack resonators, which act as the building blocks of the CCAs we use in the later chapters.

Chapter 2

RACETRACK RESONATORS

2.1 Introduction

The constituent sites of our photonic CCAs are racetrack resonators. At the most basic level, racetrack resonators consist of an optical waveguide looped onto itself, in, as the name suggests, a racetrack shape. This folding onto itself creates a photonic cavity where only specific wavelengths constructively interfere. The resonance condition for a racetrack resonator can be written as:

$$\frac{\mu_m}{c} n_{eff} l = 2\pi m \text{ or} \tag{2.1}$$

$$n_{eff} l = m\mu_m^{\lambda} \tag{2.2}$$

where n_{eff} denotes the effective refractive index of the photonic waveguide, l denotes the path length of the racetrack resonator, m denotes the mode number, μ_m denotes the resonant frequency or the onsite potential in the CCA terminology, and finally μ_m^{λ} denotes the resonant wavelength or the onsite potential in wavelength units.

Schematic of a typical racetrack resonator is depicted in Fig. 2.1. The racetrack resonator is coupled to two waveguides to couple light in/out of the resonator structure. Depending on which port is used to input the light into the device, the corresponding through port and drop port can be defined. These are named so because in case of a lossless resonator, at an off-resonant wavelength, all the light in the input arm passes through to the through port without coupling to the racetrack resonator whereas on-resonance, all the light gets coupled to the resonator and then exits through to the drop port. Note that a racetrack resonator at any frequency supports two degenerate, uncoupled modes: (i) clockwise circulating, and (ii) anticlockwise circulating. The direction of input light dictates which of the two modes gets

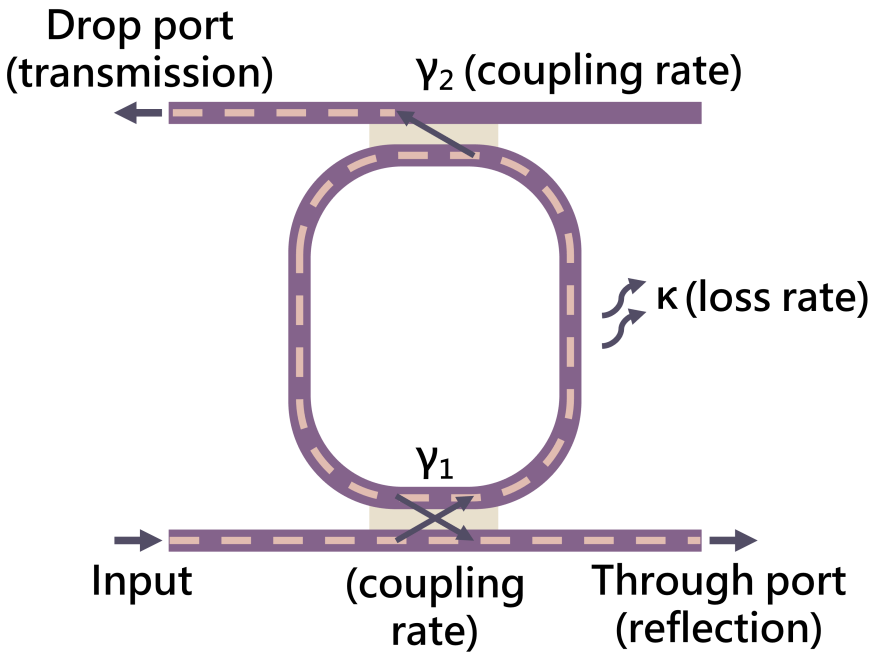

Figure 2.1: Schematic depicting a racetrack resonator. The racetrack resonator is coupled to two photonic waveguides on either side to couple light in/out of the resonator. γ_1, γ_2 denotes the coupling rates between these waveguides and the resonator. κ denotes the loss rate from the resonator.

excited. In the presence of back scattering, however, there can be coupling between these modes. For our work, we assume minimal back scattering in the racetracks and will only refer to one mode at a particular frequency going forward.

2.2 Modelling

We use input/output formalism to model the cavity and its coupling to the bus waveguides. The single photon Hamiltonian describing the resonator is simply ($\hbar = 1$):

$$H = \mu a^\dagger a \tag{2.3}$$

where a denote the photonic destruction operator of the racetrack cavity mode and μ denotes the resonant frequency. Using input-output formalism [23] we can then write that:

$$\frac{\mathrm{d}a}{\mathrm{d}t} = -j\mu a - \frac{\kappa}{2}a - \frac{\gamma_1 + \gamma_2}{2}a - \sqrt{\gamma_1}x_1 \tag{2.4}$$

where κ denotes the loss rate from the cavity to the surrounding environment, γ_1 and γ_2 denote the coupling rates to the bus waveguides and x_1 denotes the photonic destruction operator for the input mode. Taking Fourier transform of the equation then gives:

$$-j\omega a = -j\mu a - \frac{\kappa}{2}a - \frac{\gamma_1 + \gamma_2}{2}a - \sqrt{\gamma_1}x_1 \tag{2.5}$$

Rearranging terms then gives us:

$$\sqrt{\gamma_1}x_1 = j\left(\omega - \left(\mu - j\frac{\kappa}{2} - j\frac{\gamma_1 + \gamma_2}{2}\right)\right)a \tag{2.6}$$

Note that the second term in the bracket describes the effect of the effective Hamiltonian of the device on its scattering properties. The effective Hamiltonian of the above racetrack resonator can be written as:

$$H_{eff} = \left(\mu - j\frac{\kappa}{2} - j\frac{\gamma_1 + \gamma_2}{2}\right)a^{\dagger}a \tag{2.7}$$

The terms in the above equation can then be rearranged to give the following relation between the cavity state and the input:

$$a = \frac{-j\sqrt{\gamma_1}x_1}{(\omega - (\mu - j\frac{\kappa}{2} - j\frac{\gamma_1+\gamma_2}{2}))} \tag{2.8}$$

Let the output at the through port be denoted by y_1 (destruction operator for the output waveguide mode) and similarly at drop port be denoted by y_2. Then using input-output theory we can write:

$$y_1 = x_1 + \sqrt{\gamma_1}a \tag{2.9}$$

$$y_2 = \sqrt{\gamma_2}a \tag{2.10}$$

Experimentally though we are concerned about the reflection and transmission spectrum of the racetrack resonator which can be defined as:

$$|R(\omega)|^2 = \left|\frac{y_1}{x_1}\right|^2 ; \ |T(\omega)|^2 = \left|\frac{y_2}{x_1}\right|^2 \tag{2.11}$$

Substituting from above then first allows us to obtain the reflection spectrum as:

$$|R(\omega)|^2 = \left|\frac{y_1}{x_1}\right|^2 = \left|\frac{x_1 - j\gamma_1 x_1(\omega - (\mu - j\frac{\kappa}{2} - j\frac{\gamma_1+\gamma_2}{2}))^{-1}}{x_1}\right|^2 \tag{2.12}$$

$$\implies |R(\omega)|^2 = \left|1 - \frac{j\gamma_1}{\omega - (\mu - j\frac{\kappa}{2} - j\frac{\gamma_1+\gamma_2}{2})}\right|^2 \tag{2.13}$$

$$\implies |R(\omega)|^2 = \frac{(\omega-\mu)^2 + (\frac{\kappa+\gamma_2-\gamma_1}{2})^2}{(\omega-\mu)^2 + (\frac{\kappa+\gamma_1+\gamma_2}{2})^2} \tag{2.14}$$

It can be seen that for a lossless racetrack resonator ($\kappa = 0$) with equal coupling rates to the bus waveguides ($\gamma_1 = \gamma_2$), reflection spectrum at resonance drops to zero i.e. $|R(\omega = \mu)|^2 = 0$. Next, the transmission spectrum of the racetrack resonator can be written as:

$$|T(\omega)|^2 = \left|\frac{y_2}{x_1}\right|^2 = \left|\frac{-j\sqrt{\gamma_1\gamma_2}x_1(\omega - (\mu - j\frac{\kappa}{2} - j\frac{\gamma_1+\gamma_2}{2}))^{-1}}{x_1}\right|^2 \tag{2.15}$$

$$\implies |T(\omega)|^2 = \left|\frac{\sqrt{\gamma_1\gamma_2}}{\omega - (\mu - j\frac{\kappa}{2} - j\frac{\gamma_1+\gamma_2}{2})}\right|^2 \tag{2.16}$$

$$\implies |T(\omega)|^2 = \frac{\gamma_1\gamma_2}{(\omega-\mu)^2 + (\frac{\kappa+\gamma_1+\gamma_2}{2})^2} \tag{2.17}$$

Similarly, for a lossless racetrack resonator ($\kappa = 0$) with equal coupling rates to the bus waveguides ($\gamma_1 = \gamma_2$), the transmission spectrum at resonance equals one i.e. $|T(\omega = \mu)|^2 = 1$.

We can see from the above equation that the transmission spectrum of a racetrack resonator is a Lorentzian function centered at cavity potential μ and with linewidth of $\kappa + \gamma_1 + \gamma_2$. This allows us to also calculate the Quality factor or Q of the resonator, defined as the ratio of resonator frequency to the linewidth:

$$Q = \frac{\omega_r}{\Delta\omega} = \frac{\mu}{\kappa + \gamma_1 + \gamma_2} \tag{2.18}$$

Even though we have derived the above model using input-output formalism, in absence of any modifications in Hamiltonian, the model remains valid in the classical regime by replacing the operators by their mean field approximations i.e. $a = \langle a \rangle$. Similarly, the energy stored in the cavity can be represented by $|a|^2$. This also allows us to show how the Q factor acts as a measure of resonator losses.

$$Q = \omega_r \frac{\text{Energy stored in the cavity}}{\text{Power loss}} = \mu \frac{|a|^2}{(\kappa + \gamma_1 + \gamma_2)||a|^2} = \frac{\mu}{\kappa + \gamma_1 + \gamma_2} \tag{2.19}$$

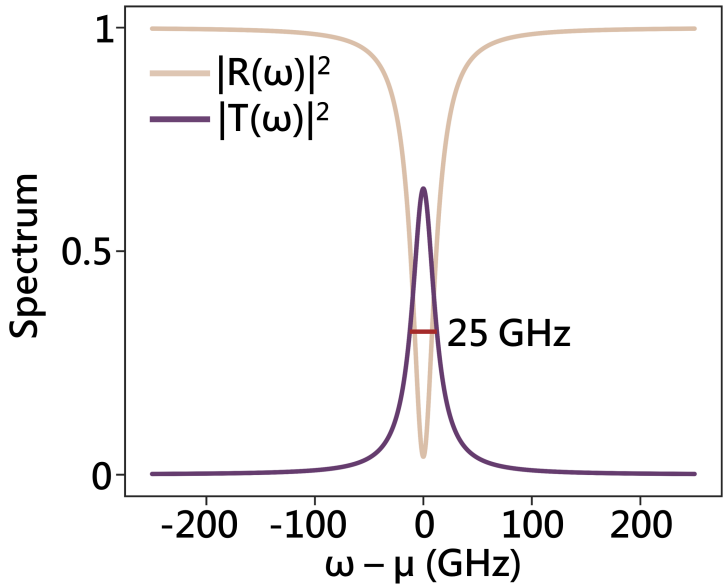

Figure 2.2: Sample reflection and transmission spectra of a racetrack resonator. The resonant wavelength is 1550 nm and hence $\mu \approx 193.4\ THz$. Loss rate $\kappa = 5\ GHz$ and coupling rates are $\gamma_1 = \gamma_2 = 10\ GHz$. The cavity linewidth is denoted by the red dash with $Q \approx \frac{193.4}{0.025} \approx 7800$.

In Fig.2.2 we plot the reflection and transmission spectrum of a typical racetrack resonator operating at optical frequencies. Note, that we are using the single mode approximation here and the racetrack resonators in general support multiple modes satisfying the Eq. 2.1. This approximation is valid as long as we excite the resonator near its resonant frequency [24]

and particularly useful while extending this model to simulate CCAs made up of multiple coupled racetrack resonators.

Chapter 3

SCALABILITY

The contents of this chapter are adapted from [15]; *Abhi Saxena, Yueyang Chen, Zhuoran Fang, and Arka Majumdar. "Photonic topological baths for quantum simulation" ACS Photonics 9, no. 2 (2022)*: 682-687; with permission from the authors.

3.1 Introduction

The first condition that needs to be met for photonic coupled cavity arrays (CCAs) to be used for quantum simulation is that these must be scalable. Motivated by the recent interest in controlling the topological properties of photonic lattices to utilize the topological protection of the resulting quantum many body states to realize novel forms of light-matter interaction in such systems [25–28], in this chapter we focus on realizing scalable photonic CCAs that implement topological phases on photonic lattices made with high quality (Q) factor and low mode volume resonators with spectral accessibility to individual super-modes making them suitable for quantum simulation in the optical domain [29]. Due to unavoidable imperfections in nanofabrication, these high-Q optical resonator arrays are inherently prone to disorder in their resonant frequencies. Without undertaking suitable mitigating steps in design of these arrays, this uncontrolled disorder can be a serious impediment in constructing photonic CCAs suitable for studying various quantum optical phenomena. Typical CCAs used to demonstrate topological states in the optical domain [14, 18, 24, 30–34] operate in a regime where fabrication induced disorder is comparable or greater than the relevant hopping rates between the cavities. While such a regime is sufficient for observing the topological modes, it is not suitable for estimating all the parameters of a Hamiltonian, as needed for quantum simulation.

Here, by increasing the effective mode overlap between resonator sites, we overcome the effects of the underlying disorder and experimentally realize topological quantum electrodynamics baths which are photonic analogs of the Su-Schrieffer-Heeger (SSH) model [35]. We show that these CCAs (with individual Q-factor exceeding 3.1×10^4) operate in a regime which is suitable for quantum simulation and can be used to impart special topological properties to interacting photons, as discussed in depth by Bello *et al.* [25]. Note that while the microwave photons in superconducting circuits have already been used to exhibit these unconventional quantum phenomena [10], such a demonstration is missing in optical domain. As discussed in the Ch. 1, observing similar effects in optics will not only significantly simplify the experiments due to performability at much higher temperatures, but will also allow measurements of multi-particle correlations due to the availability of single photon detectors.

3.2 Description of a SSH Photonic bath

The SSH model describing the topological photonic bath is illustrated in Fig. 3.1(a). The photonic lattice consists of sub-lattices A and B of the array, respectively, made up of cavities with resonant frequency ω_0. The intracell hopping rate between the sites A and B of a unit cell is given by J_1 and the intercell hopping rate between the unit cells is denoted by J_2. The Hamiltonian of this bath can be written as ($\hbar = 1$):

$$\mathcal{H} = \sum_i \omega_0(a_i^\dagger a_i + b_i^\dagger b_i) + J_1(b_i^\dagger a_i + a_i^\dagger b_i) + J_2(b_i^\dagger a_{i+1} + a_{i+1}^\dagger b_i) \tag{3.1}$$

where $a_i^\dagger(a_i)$ and $b_i^\dagger(b_i)$ denote the site bosonic creation (destruction) operators at site A and B of the i^{th} unit cell. Assuming periodic boundary conditions, the Hamiltonian in momentum space can be written as

$$\tilde{\mathcal{H}}(k) = \begin{bmatrix} \omega_0 & J_1 + J_2 e^{-jk} \\ J_1 + J_2 e^{jk} & \omega_0 \end{bmatrix} \tag{3.2}$$

The properties of this disorder free bath can be summarized as follows:

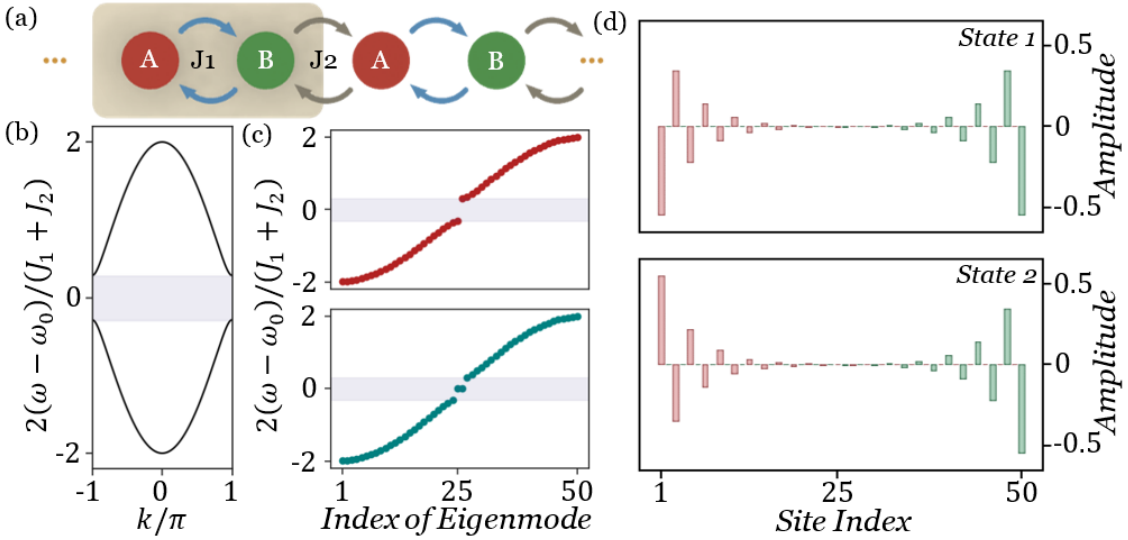

Figure 3.1: (a) Schematic of the SSH bath. The photonic lattice consists of two sub-lattices A (red) and B (green). The intracell hopping rate is J_1 and intercell hopping rate is J_2. (b) Dispersion relation of the SSH baths, where the shaded region denotes the band gap. (c) Resonant frequencies of finite baths consisting of $N = 50$ sites. Trivial phase (red) is characterized by $J_1 > J_2$, whereas the topological phase (blue) characterized by $J_1 < J_2$. (d) Wave function of the hybridized edge modes of a topological bath with $N = 50$ sites. Left edge state is localized on sub-lattice A (red), right edge state is localized on sub-lattice B (green).

(i) The bath has a chiral symmetry [36] owing to which the eigenstates of the Hamiltonian $\tilde{\mathcal{H}}(k)$ form two symmetric bands about ω_0 given by

$$\omega_{\pm}(k) = \omega_0 \pm \sqrt{J_1^2 + J_2^2 + 2J_1J_2cos(k)} \tag{3.3}$$

where the $\pm$ denotes the upper/lower pass bands [Fig. 3.1(b)] with a band gap of $2|J_1 - J_2|$.

(ii) This bath supports topologically non-trivial phases [36] depending on whether $J_1 < J_2$ which is termed as the 'topological' phase or $J_1 > J_2$ which is termed as the 'trivial'

phase. In a finite bath, these phases lead to formation of topological states localized at the edges of the lattice with an exponential decay into the bulk [32,36]. These edge states lie in the middle of the band gap centered around ω_0 for the topological phase and disappear for the trivial phase [Fig. 3.1(c)]. They have non-vanishing amplitude over only one of the two sub-lattices A or B and the small amount of overlap in the bulk causes these edge modes to hybridize as even and odd eigenstates of the system [Fig. 3.1(d)].

(iii) Bello *et al.* [25] and Kim *et al.* [10] have shown that if a quantum emitter with transition frequency lying at the center of band gap (ω_0) is coupled to a site of this SSH bath, the resulting photonic bound state mimics an effective topological edge state in the middle of the bath. This bound state inherits all the properties of the topological edge states, localizing the photon to one direction and sub-lattice depending on the site type (A or B) to which the emitter is coupled. In the presence of several emitters these states can be used to mediate directional, topological interactions between them which can give rise to exotic many body phases.

3.3 Effects of fabrication disorder

These properties, which are critical to realize unconventional quantum phenomena using a topological bath, are adversely affected in the presence of fabrication disorder. In optical domain, a scalable implementation of the SSH bath relies on nanofabrication to create solid state optical CCAs. The major form of disorder that exists in solid state photonic systems is in the resonance frequencies of the cavities, arising from the inconsistencies in lithography and etching as well as from the non-uniformities in the film thickness of the bare wafer itself. This disorder is modelled by modifying the diagonal terms of the Hamiltonian to include random δ_i' s drawn from a zero-mean Gaussian distribution with a standard deviation σ [37, 38]. Thus, the modified bath's Hamiltonian in presence of this diagonal disorder can be written

as

$$\mathcal{H}^{\sigma} = \mathcal{H} + \sum_{i} \left(\delta_{a,i} a_i^{\dagger} a_i + \delta_{b,i} b_i^{\dagger} b_i \right) \tag{3.4}$$

It is straightforward to see that the eigen-properties of this Hamiltonian depend on relative values of $J_1 - J_2$, σ and $J_1 + J_2$. Hence, we define a dimensionless parameter

$$\eta = 2\sigma/(J_1 + J_2) \tag{3.5}$$

as the measure of relative disorder present in our system. We study the effect of the diagonal disorder on the key properties of the bath by looking at the evolution of topological bound states and the transmission spectrum as we sweep across σ keeping J_1, J_2 constant.

As mentioned in property (iii), the presence of a quantum emitter lying in the middle of the band gap (ω_0) induces formation of bound directional states, which are akin to topological edge states in their properties [25]. We first study the effect of disorder on this type of bound state. In Fig. 3.2, we consider a bath made of 50 resonators configured in trivial phase with a quantum emitter coupled to a type A site in the middle of the array. For this system, we plot the modulus of the amplitude of the induced bound state wave function averaged across 10^4 disorder realizations per η. Without any disorder, the bound state envelope extends towards the right direction and occupies only the B sub-lattice. The presence of diagonal disorder breaks the chiral symmetry of the Hamiltonian and protection to the bound state weakens. Despite this, in the region where $\eta << 1$ the bound state exists with strong localization towards one direction and vanishing amplitudes on the conjugate sub-lattice. As the value η increases, the bound state becomes more delocalized and has weights over both the sub-lattices. When $\eta \to 1$ overall averaged bound state wave function over different realizations is spread across the array and loses all of its topological properties.

Fabricated photonic baths (CCAs) are experimentally characterized by measuring the transmission spectrum $|T(\omega)|^2$ as relevant Hamiltonian parameters can be extracted in a straightforward manner from such a measurement. To observe the effect of disorder on the transmission spectrum; we simulate and plot $|T(\omega)|^2$ of a photonic CCA with 8 sites for both topological and trivial phase, again averaging across 10^4 disorder realizations per η [Fig.

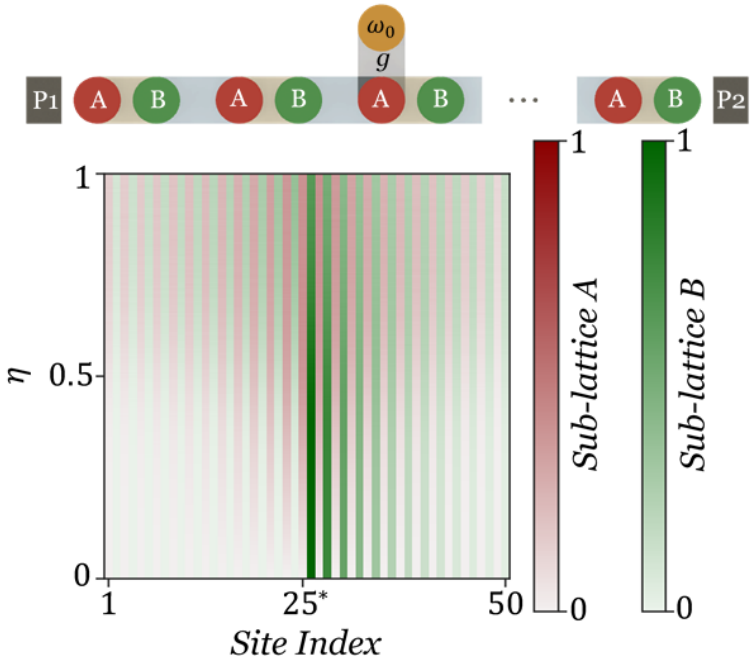

Figure 3.2: Modulus of amplitude of bound state wavefunction (normalized) as we sweep across η averaging over 10^4 disorder realizations per η. The schematic depicts a quantum emitter coupled to a SSH bath in trivial phase ($J_1/J_2 = 1.336$) at a site of sub-lattice A. The coherent emitter-cavity coupling rate is $g = (J_1 + J_2)/10$. In absence of any disorder, the bound state is localized towards the right with non-zero amplitude on sub-lattice B only. The direction of this envelope changes if the emitter is coupled to sub-lattice B instead of A. 25^* denotes the position of emitter in the array. Amplitudes on sub-lattice A are in red and on sub-lattice B are in green.

3.3]. The first thing that becomes immediately obvious is that the transmission amplitude of the modes farthest from the bare resonance is rather small, even when $\eta = 0$. This comes out naturally in the process of solving a set of coupled mode equations and combining it with the input-output formalism to express output field in terms of input fields. When the disorder is added to this model, we find that the transmission of the farthest modes gets rapidly less prominent, even in the region $\eta << 1$. Consequently, probing all super modes becomes very difficult in a cavity array with large number of sites. As the value of η further

increases, the modal peaks start to merge, and in the region with $\eta >> 1$ the averaged plot approaches a broad Gaussian distribution. This behavior clearly indicates that $\eta < 1$ is a necessary condition when using the transmission spectrum for accurately identifying eigenmodes of the simulated Hamiltonian and calculating relevant parameters like location and size of band gaps which play a critical role in determining quantum properties of the system. Thus, looking at the behavior of both the topological bound states and the transmission spectrum with increasing disorder, we can conclude that operating in the regime $\eta << 1$ can mitigate the effects of inherent fabrication disorder and allows us to harness the unconventional topological properties of the SSH bath. This can be achieved by designing the CCA such that individual sites have much larger hopping rates than the disorder.

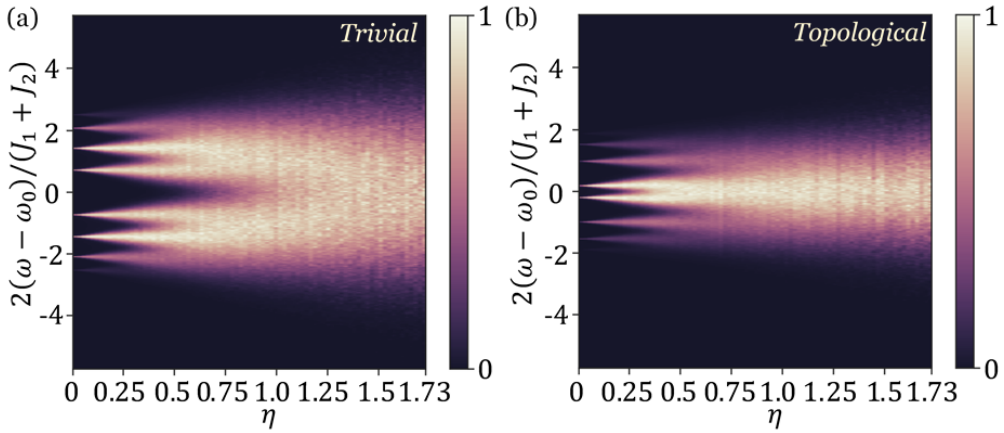

Figure 3.3: Transmission spectrum $|T(\omega)|^2$ of a photonic bath with 8 sites; averaged across 10^4 disorder realizations per η (a) Trivial phase ($J_1/J_2 = 1.336$) (b) Topological phase ($J_2/J_1 = 1.336$).

3.4 Experimental realization

To realize these baths, we implemented the photonic analog of SSH model as CCAs made from racetrack resonators fabricated in silicon photonics with 220 nm thick Si layer on a 3 μm thick SiO_2 film [Fig. 3.4(a)]. Each device is probed via a set of grating couplers located

at the first and last site to coherently measure its transmission and reflection spectra. A similar platform has been used before [14] to show the existence of higher order edge states in photonic lattices. Those devices were operated in a regime where localization lengths of the edge states were extremely small ($J_2/J_1 >> 1$) and the band gap ($2|J_1 - J_2|$) size was similar to the disorder magnitude. But their disorder to hopping rate ratio was, $\eta = 1.95$ which is $>> 1$. While edge states can be observed in this regime, as discussed above, it is not suitable for enabling bath mediated directional interactions between emitters for quantum simulation purposes. In order to reach the regime of $\eta << 1$ we need to increase the absolute value of hopping rates between the lattice sites. Hopping rates between optical cavities depend on the mode overlap of the two resonators $J \propto e_1^* e_2$ [39, 40] where e_1 and e_2 denote mode volume normalized field profiles of the resonator modes. This overlap can be increased in broadly three ways: (1) by reducing the physical distance between sites, (2) by increasing the length of the coupling region between the resonators, and (3) by reducing their mode volumes. The resolution of the lithography process limits the closest gap we can place two resonators without introducing additional disorder. Therefore, to increase the hopping rates further, we need to reduce the size of resonators and increase the length of interaction region between them. To this end, we fabricated device arrays made up of racetrack resonators which are 60 μm long with a 12 μm long coupling region. To obtain two differing hopping rates between the resonators, we kept the inter-resonator gap to be either 90 nm or 110 nm. The shorter length of the racetrack resonators not only helps in reduction of the mode volume but also ensures a large free spectral range for the devices to prevent interaction between different longitudinal modes of the same resonator. Then, we measured the transmission spectrum of these devices. It is well-known that the devices fabricated on different parts of the chip are more susceptible to disorder and suffer from an overall mean frequency shift owing to variations in nanofabrication processes across the chip area [24, 37, 38]. We label this as the global disorder and characterized it via a statistical study of spectral modes across devices and tracking their mean frequency [Table 3.1]. We fabricated arrays with varying number of racetrack resonator sites ranging from 1 to 16 on the same chip. Only devices in

Table 3.1: Disorder compilation of the SSH photonic CCA, $J_1/2\pi = 163\ GHz$, $J_2/2\pi = 122\ GHz$.

σ_{type}	$\sigma/2\pi(GHz)$	η	# Measured
Global	70.68	0.49	25
Local	8.02	0.056	18

which we could spectrally resolve all the modes, were used to calculate the disorder. Usually this global disorder, calculated from statistics of the mean frequency of modes is subtracted from the spectrum as an overall shift to the origin [37]. This approach is strictly valid only if we are dealing with arrays that have small footprint on a chip. As the cavity arrays have an increasing number of sites, the device area starts to grow, and therefore within one big device global disorder cannot just be ignored as an overall origin shift.

We also calculated and characterized local disorder, which persists even after shifting the spectra to a common origin. To calculate this disorder, we measured the deviation of each individual mode across instances of similar devices across the chip:

$$\sigma_{local} = \frac{1}{2\pi}\sqrt{\sum \frac{(\omega_i - \omega_i^{mean} - \omega_{shift}^{g})^2}{n}} \tag{3.6}$$

where ω_i is the frequency of the i^{th} super-mode, ω_{shift}^{g} is the global frequency shift to align the origins and ω_i^{mean} is the mean position of the super-mode across the same device design made at different locations of the chip. This method allowed us to combine statistical data for disorder from devices with various number of sites and with varying phases (topological/trivial). The calculated value of η for local disorder was 0.056 ($<< 1$).

The larger hopping rates present in these arrays allow for reduction of the effects of disorder. In lattices with up to 8 sites we observe spectral accessibility to all the modes and global

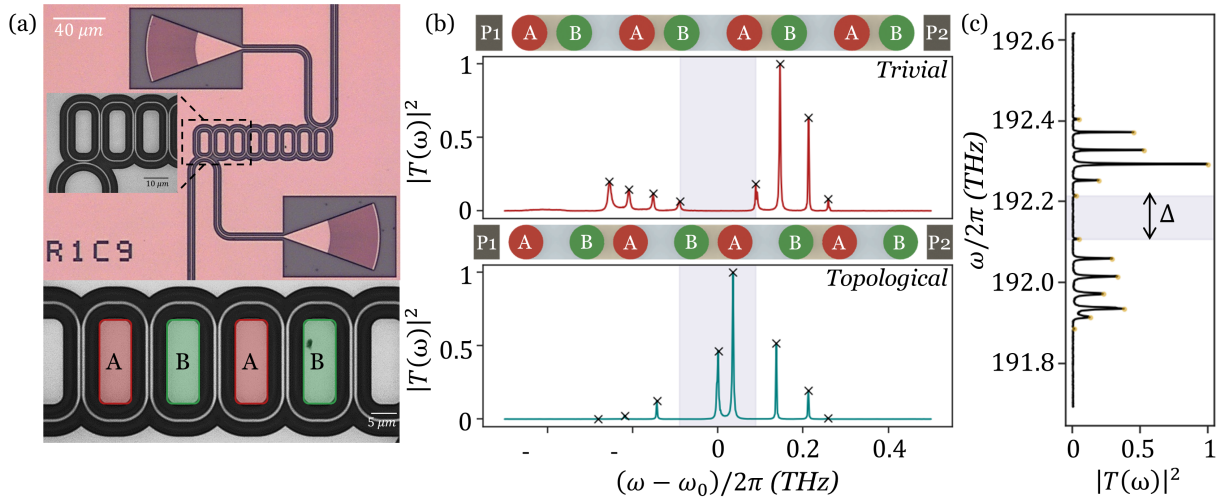

Figure 3.4: (a) Optical micrographs of a photonic SSH CCA. (b) Normalized transmission spectrum of a SSH photonic CCA with 8 sites. The upper plot (red) depicts the trivial phase, whereas the lower plot (blue) depicts the topological phase. We can observe the band gap (shaded) formation in trivial phase, and the existence of edge modes in the middle of the band gap in topological phase. The schematic depicts the ports i.e., the grating couplers used for transmission measurement. (c) A SSH photonic CCA made of 8 unit cells i.e., 16 sites in trivial phase. Measured band gap is $\Delta = 0.107\ THz$ which closely matches the theoretical prediction of 0.11 THz.

disorder has minimal effects on devices. This allows for clear comparison of band gap formation in the case of trivial phase and existence of two edge modes lying inside the band gap in the topological phase [Fig. 3.4(b)]. For photonic baths with more than 8 sites all modes are not clearly observable due to vanishing amplitudes further away from the mean frequency and increasing effects of global disorder on the spectrum. Despite this, the device design allows for realization of photonic baths (here, trivial phase) with up to 16 sites [Fig. 3.4(c)]. We can observe a clear band gap formation with $\Delta = 0.107\ THz$ which is within 3% of the theoretical prediction. As discussed before, such a photonic bath can be used to endow

several special properties to coupled emitters also described in detail by Bello *et al.* [25].

3.5 Effects of off-diagonal disorder

In principle, in addition to the diagonal disorder in the resonant frequencies of each site, off-diagonal disorder in the hopping rates between individual sites of the bath also exists in such devices. For example, this might arise due to inconsistencies in the gaps between sites of a photonic bath. We can model this disorder by modifying the off-diagonal terms of the Hamiltonian to include random $\delta_{J_{1/2},i}$' s drawn from a Gaussian distribution with a standard deviation χ. Thus, the Hamiltonian of the SSH bath in presence of off-diagonal disorder can be written as

$$\mathcal{H}^{\chi} = \mathcal{H} + \sum_{i} \Big(\delta_{J_1,i}(b_i^{\dagger} a_i + a_i^{\dagger} b_i) + \delta_{J_2,i}(b_i^{\dagger} a_{i+1} + a_{i+1}^{\dagger} b_i) \Big) \tag{3.7}$$

The eigen-properties of this Hamiltonian depend on the relative values of $J_1 - J_2$, χ and $J_1 + J_2$. Hence, to study the effect of this disorder we can define a new dimensionless parameter

$$\eta^J = 2\chi/(J_1 + J_2) \tag{3.8}$$

Practically though, this form of disorder is expected to have minimal effect on the key properties of a SSH bath. Both the edge states in the topological phase bath and the photonic bound state formed via an emitter coupled to a trivial phase bath are protected from the effects of off-diagonal disorder owing to the preservation of chirality of the modified SSH Hamiltonian. To illustrate this, in Fig. 3.5 we plot the modulus of the amplitude of the induced bound state wave function arising from a coherent emitter coupled to the trivial SSH bath averaged across 10^4 off-diagonal disorder realizations per η^J.

As evident, unlike the case of diagonal disorder where the breaking of chirality caused loss of directional and sub-lattice localization, even for increased values of η^J, the bound state formed still enjoys topological protection from the underlying Hamiltonian (Eq. 3.7). Next up, we look at the effect of off-diagonal disorder on the transmission spectra of the CCA mimicking the bath. From engineering considerations, we do not expect this to have signifi-

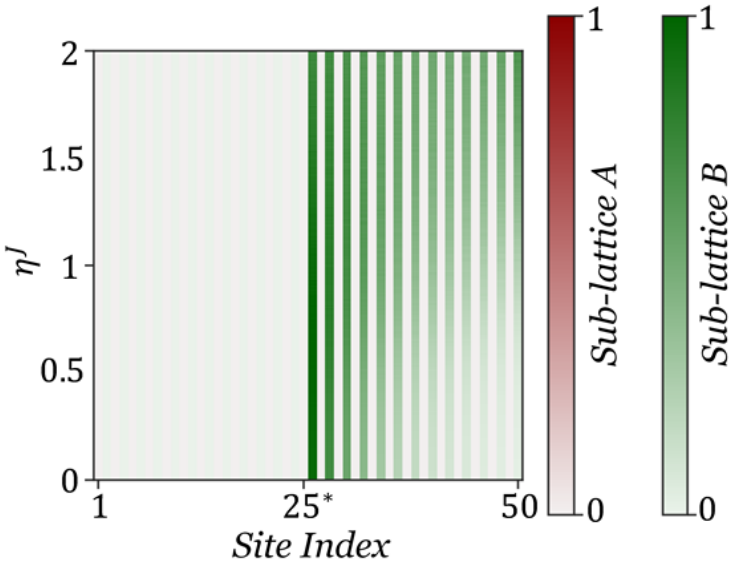

Figure 3.5: Modulus of amplitude of bound state wavefunction (normalized) as we sweep across η^J averaging over 10^4 disorder realizations per η^J. The quantum emitter is coupled to a SSH bath in trivial phase at a site of sub-lattice A at site 25. Amplitudes on sub-lattice A are in red and on sub-lattice B are in green.

cant experimental effect because of the high reliability with which electron beam lithography can attain gaps of the size 90 nm. A maximum upper bound on the off-diagonal disorder can be obtained by assuming the local disorder to be zero in the statistical analysis of eigenmodes extracted from the devices. For example, in a CCA made of two coupled resonators with resonant frequencies ω_0, hopping rate J and local diagonal disorder δ; the difference between eigenmodes of the device can be written as

$$\lambda_2 - \lambda_1 = 2\sqrt{J^2 + \delta^2/4} \tag{3.9}$$

It is easy to see that any additional disorder in J that is χ, is always $\leq$ standard deviation of $(\lambda_2 - \lambda_1)/2$. Following this approach, the experimental maximum value of η^J (the disorder metric for the coupling rate) was obtained to be $max(\eta^J) = 0.1$ by finding the deviations in hopping rates from mode positions assuming local disorder to be zero. In Fig. 3.6 we

simulate and plot the effect of off-diagonal disorder on the transmission spectra of the bath around this value. It is clear from the figure that even for the experimental maximum value of η^J which is obtained assuming local disorder $\sigma_{local} = 0$, the effect of the off-diagonal disorder is minimal.

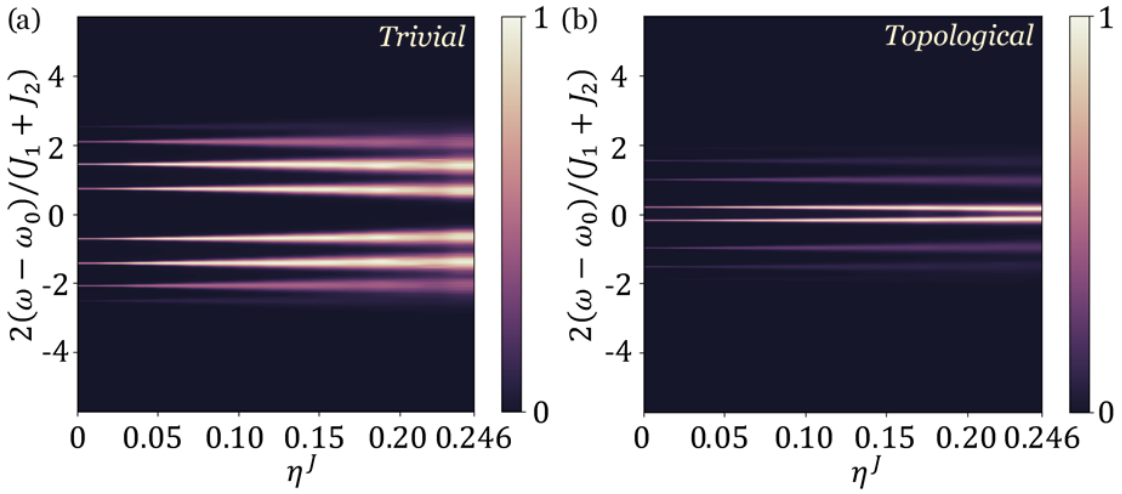

Figure 3.6: Transmission spectrum $|T(\omega)|^2$ of a photonic bath with 8 sites; averaged across 10^4 disorder realizations per η^J (a) Trivial phase (b) Topological phase.

3.6 Additional properties of the SSH photonic baths

3.6.1 Band gap & disorder

The band gap of a SSH photonic bath is given by $2|J_1 - J_2|$. If the requirement from an experiment is only observation of topological states of the photonic bath, the condition on η can be somewhat loosened for a transmission spectrum measurement. For example, in Fig. 3.7 we plot the transmission spectra $|T(\omega)|^2$ of a SSH CCA with 8 sites in topological phase averaging across 10^4 disorder realizations per η, but this time mark the point where disorder magnitude σ equals the band gap or $\eta = 4|J_1 - J_2|/(J_1 + J_2)$. It can be seen that if the measurement is only to be used to validate the existence of topological edge states, it is

sufficient to operate in a regime where $\eta < 4|J_1 - J_2|/(J_1 + J_2)$. Similar idea has been used in other works to demonstrate existence of edge sates [14]. But as demonstrated by Fig. 3.7, if the experiment involves working with devices for quantum simulation purposes, then $\eta << 1$ is a necessary condition when using the transmission spectrum for accurately identifying the eigenstates of the simulated Hamiltonian and extracting other relevant information like the band gap of the photonic bath.

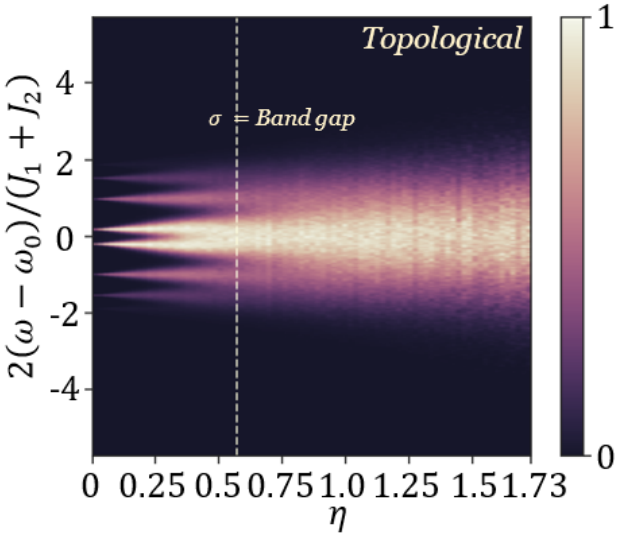

Figure 3.7: Transmission spectrum $|T(\omega)|^2$ of a SSH photonic CCA in topological phase ($J_2/J_1 = 1.336$) with 8 sites; averaged across 10^4 disorder realizations per η. The vertical line denotes the value where $\sigma = 2|J_1 - J_2|$.

3.6.2 Localization length

Another important property of the SSH photonic bath is the edge state localization length ξ in the topological phase which depends on the ratio of the hopping rates J_2/J_1 as [36]

$$\xi = \frac{1}{log(\frac{J_2}{J_1})} \tag{3.10}$$

where $J_2 > J_1$ for the topological phase. In Fig. 3.8 we plot the effect of this ratio on the edge states keeping $J_2 - J_1$ constant (this ensures that band gap $= 2|J_1 - J_2|$ does not change).

The wave function of the edge states is localized on either side on respective sub-lattices, with an exponential tail into the bulk. As J_2/J_1 increases, the localization length decreases and when $J_2/J_1 >> 1$, the edge modes are almost entirely localized on the first and last sites.

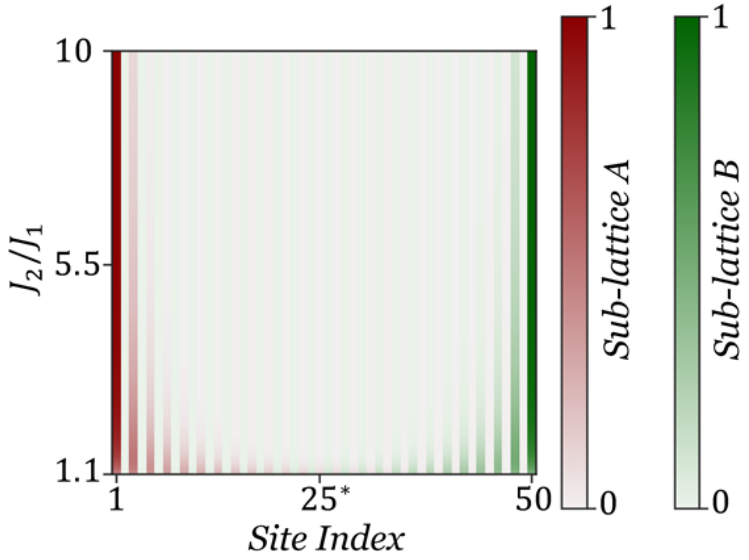

Figure 3.8: Modulus of amplitude of wavefunctions (normalized) for hybridized edge states as we sweep across J_2/J_1 keeping $J_2 - J_1$ constant. Sub-lattice A in red and sub-lattice B in green.

In Figs. 3.9(a), 3.9(b) we plot the effect of disorder on the edge states for two cases $J_2/J_1 = 6.25$ and $J_2/J_1 = 1.33$. As seen, a large J_2/J_1 causes the amplitude on each successive site to decay very rapidly. This approach is again useful to demonstrate topological edge states [14] despite a large disorder to hopping rate ratio η. But as discussed in the chapter such a regime of operation, though useful for observation of edge states, is not suitable for quantum simulation purposes. For using a photonic bath to mediate long range topological interactions of quantum emitters $\eta < 1$ is required. In Fig. 3.10 we demonstrate the effect of disorder for a bound state arising when an emitter with zero detuning is coupled to a trivial SSH bath ($J_1 > J_2$) with $J_1/J_2 = 6.25$. As evident, the bound state loses it special properties

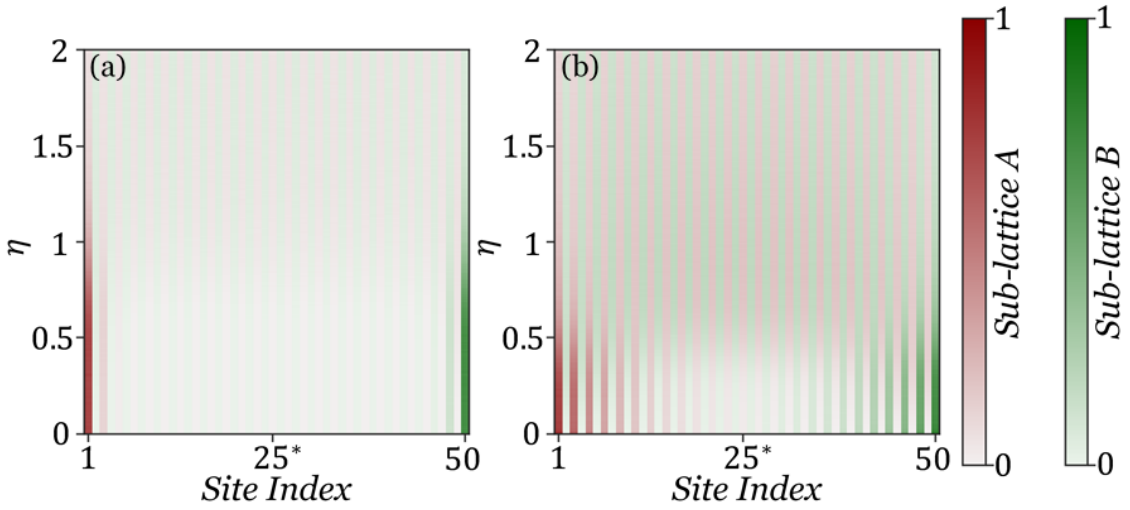

Figure 3.9: Disorder study for edge states. Modulus of amplitude of wavefunctions (normalized) for: (a) Hybridized edge state amplitude averaged across 10^4 disorder realizations per η with $J_2/J_1 = 6.25$. (b) Hybridized edge state amplitude averaged across 10^4 disorder realizations per η with $J_2/J_1 = 1.33$. Sub-lattice A in red and sub-lattice B in green.

like chirality and sub-lattice localization when $\eta \to 1$. This plot is a counterpart to Fig. 2 in the main text where we plotted a similar figure but with $J_1/J_2 = 1.33$. A longer localization length allows the bath to mediate interactions over a longer range, which was the motivation for keeping a low J_1/J_2 ratio in our work. Additionally, by using the scheme proposed in the chapter, we get a free control over J_2/J_1 and consequently the localization length. This allows for realization of topological quantum photonic baths with varying physical range of interactions, as long as we operate in $\eta << 1$ regime.

3.7 Methods

In order to calculate the local and global disorder of the SSH photonic CCA, devices with varying number of sites ranging $1 - 16$ were fabricated. In Figs. 3.11(a), 3.11(b) we plot the transmission spectra $|T(\omega)|^2$ of SSH baths with 4 sites in trivial and topological phase respectively. Different colors in the plots represent a distinct realization of the same sized

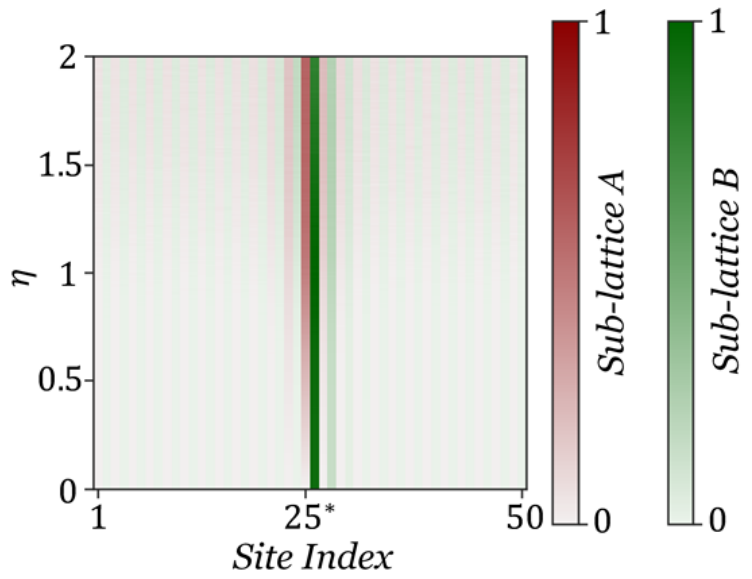

Figure 3.10: Disorder study for photonic bound state when $J_1/J_2 = 6.25$. Modulus of amplitude of photonic bound state wavefunction (normalized) averaged across 10^4 disorder realizations per η. The zero detuned emitter is coupled to trivial bath at site 25. Sub-lattice A in red and sub-lattice B in green.

bath in a separate area on the chip. For example, Fig. 3.11(a) shows transmission spectra of 3 separate SSH photonic CCAs with 4 sites in trivial phase. Similarly, Figs. 3.11(c), 3.11(d) show the transmission spectrum of baths with 6 sites in trivial and topological phase respectively.

Compiled results from these baths of varying sizes are then used to estimate the disorder. In Fig. 3.12(a) we plot deviations of the mean frequencies of various CCAs which were used to calculate the global disorder. Similarly, in Fig. 3.12(b) we plot the deviations in the mode frequencies after adjusting for the global origin shift. These were then used to calculate the local disorder present in these devices.

Fabricating CCAs of different sizes has two advantages: first, it allows us to observe how global disorder starts to have increased effect on the bath properties as the number of sites

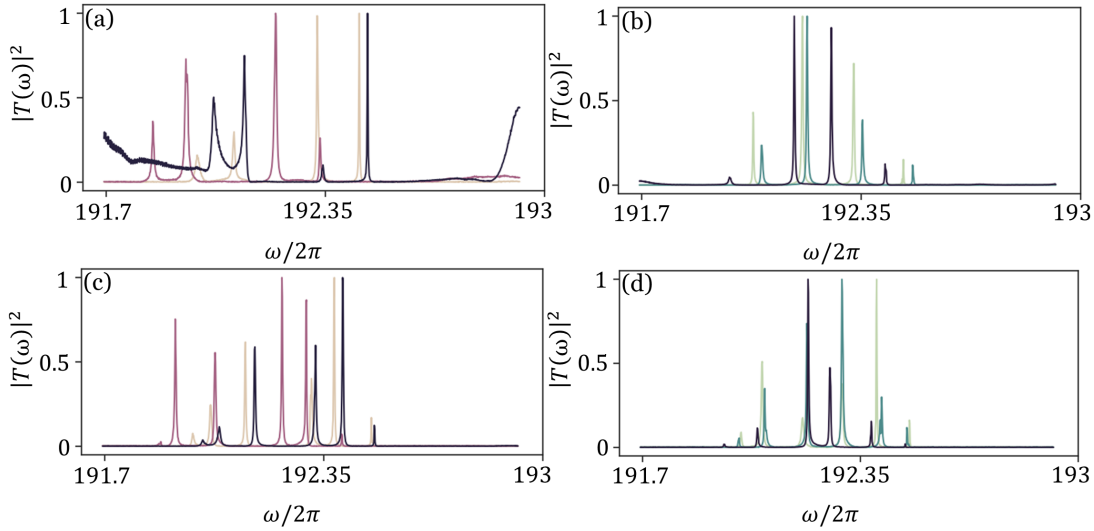

Figure 3.11: Transmission spectra of some selected CCAs. CCAs with 4 resonator sites in (a) trivial phase, (b) topological phase. CCAs with 6 resonator sites in (c) trivial phase, (d) topological phase. Different colors in each plot represent a completely distinct realization of the same sized bath in a separate area on the chip. Compiled results from CCAs with different sizes are used to calculate the disorder in system.

get larger. Second, smaller sized CCAs unlike their larger counterparts have significant amplitudes for all the super-modes. This makes them more suitable for calculating the global and local disorder arising due to fabrication.

3.8 Conclusion

In conclusion, using CCAs we experimentally demonstrated topological photonic baths which are optical analogs of the SSH model. We studied the effect of fabrication induced disorder on these baths and demonstrated the steps required to overcome its effects. A similar, more detailed demonstration has been reported in superconducting systems [10] and our work enables a way to bring such topological baths to optics by developing a paradigm to harness recent advancements made in topological photonics and applying them to quantum

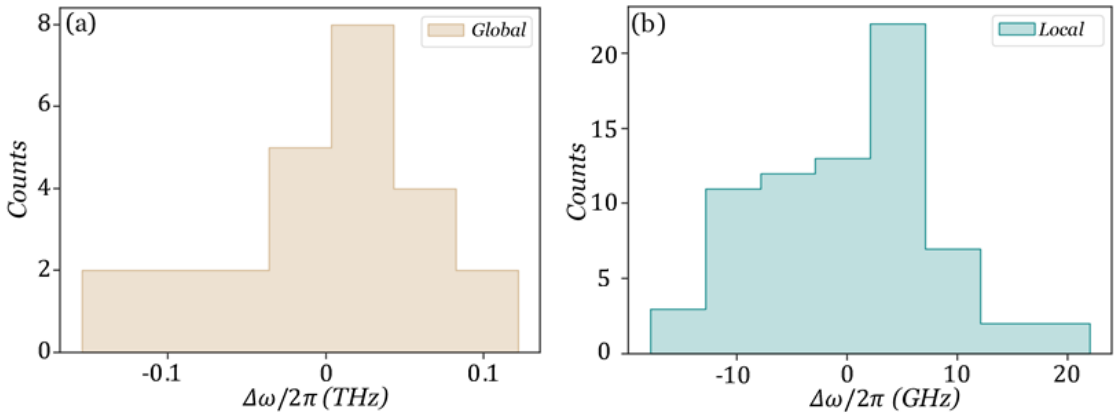

Figure 3.12: Disorder plots depicting deviations. (a) Histogram denoting deviations of mean frequency used to characterize the global disorder. (b) Histogram denoting deviations of mode frequencies from their respective mean positions after shifting to a common origin, used to characterize the local disorder.

simulation in optical domain. Through this chapter, we demonstrated the design principles and experimental approaches through which we could meet the scalability requirement for using photonic CCAs for quantum simulation purposes.

Chapter 4

MEASURABILITY

The contents of this chapter will appear in a manuscript currently being prepared.

4.1 Introduction

In the last chapter, we discussed how recent progress in controlling the topological properties of the photons by engineering synthetic magnetic fields in photonic lattices [26,31,41,42] has led to a considerable interest in photonic quantum simulation of topological many body effects like the fractional quantum Hall effect [43] and topological insulators [44]. We then discussed the methodology to scale these (topological) photonic CCAs to sizes where these can be utilized to study the underlying physics of interest.

Now in this chapter we tackle the next requirement of measurability. The first question that naturally arises is: what is meant by measurability in the context of photonic CCAs? It is as follows: once these large scale CCAs have been fabricated, in order for them to be useful for simulating nontrivial many-body phenomena, we need tomography protocols that accurately map the realized non-linear Hamiltonians. If the experiment allows single and two-photon measurements between any two arbitrary sites in the lattice, direct tomography can be performed to obtain both the linear couplings between the two sites, as well as the local anharmonicities at the site [45]. However, this protocol suffers from a crucial drawback that in most on-chip implementations of such lattices [10, 14, 46] measurement access of a node in the interior of the lattice is challenging and typically only the nodes on the outermost boundary can be accessed for accurate measurements.

These experimental requirements raise an important theoretical question — is it possible to perform tomography of the implemented Hamiltonian with access restricted to only the

boundaries of the lattice? This question has been considered in previous works, which have proposed tomography algorithms with restricted measurement access to the boundary or a subpart of the lattice for the setting of one-dimensional chains [47, 48] and two-dimensional lattices [49–51] with real-valued coupling strengths and known topologies. Subsequent work has been done to perform tomography of spin lattices with real-valued couplings and restricted number of probes through measurement of just the system time-traces, both for closed [52] and open quantum systems [53]. Additionally, work has been done to improve the efficiency of the tomography algorithms using Bell states [54], identify one-dimensional Hamiltonians through Zeeman markers [55] and perform entanglement tomography of many-body Hamiltonians [56].

However, none of these protocols would not be suitable for identification of many body Hamiltonians which are typically characterized by complex coupling strengths between modes to realize non-zero flux in closed loops [31, 41, 57] and onsite photonic interaction [10, 42]. In this chapter, we show that even under the setting of restricted access to only the outermost boundary of the lattice, both the linear couplings and onsite potentials can be measured from scattering matrix measurements. Moreover, we show that onsite anharmonicity can be measured from two-photon correlation function measurements at the boundaries. We then discuss the stability of the proposed tomography scheme and numerically establish that in typical cases, the errors in the linear algorithm scale polynomially with increasing number of sites in the lattice. Additionally, we demonstrate that under an additional assumption of the ability to toggle on/off the non-linearities, the anharmonicities in the lattice can also be determined in a stable manner. Furthermore, at the end we propose a protocol which by utilizing multi-photon Fock state scattering from the boundaries of the lattice allows to quantum-enhance the precision in the measured Hamiltonian parameters. To the best of our knowledge, our work is the first to solve this problem for general topologically non-trivial bosonic lattices with anharmonic lossy resonators and complex couplings. Moreover, as our tomography algorithm depends on steady-state measurements in the frequency domain, it avoids the need: (i) to measure time-resolved traces, which can be challenging for strongly

coupled systems, (ii) to utilize initial state preparation, or (iii) to perform quick qubit rotations. Several of the schemes mentioned earlier in the last paragraph suffer from one or more of these potential pitfalls. While our method unlike some quantum Hamiltonian tomography algorithms [45, 58] is not applicable for arbitrary photonic lattice geometries it allows precise identification of most common topological Hamiltonian models like the Hofstadter lattices [31, 41, 57, 59], strained graphene Hamiltonians [17], quantized quadrupole phase lattices [14] and SSH Hamiltonians [14, 15] without requiring experimental access to all the nodes of the lattice.

4.2 Tomography algorithm

4.2.1 Model

We consider N bosonic modes arranged on a graph $(\mathcal{V}, \mathcal{E})$, where $\mathcal{V}$ is the vertex set signifying the bosonic modes and $\mathcal{E}$ are edges which signify the linear couplings between the bosonic modes (Fig. 4.1). The effective Hamiltonian is given by ($\hbar = 1$):

$$H = \sum_{v \in \mathcal{V}} \mu_v a_v^\dagger a_v + \frac{\chi_v}{2} a_v^{\dagger 2} a_v^2 + \sum_{u,v \in \mathcal{E}} J_{v,u} a_v^\dagger a_u \tag{4.1}$$

where the parameters $J_{v,u} \in \mathbb{C}$ (the coupling strengths s.t. $J_{v,u} = J_{u,v}^*$), $\mu_v \in \mathbb{C}$ (the onsite potential including decay), $\chi_v \in \mathbb{R}$ (the onsite anharmonicity) need to be measured. Starting from the vertices at the boundary of the lattice denoted by $Bd(\mathcal{V}) = \mathcal{V}_0 \subset \mathcal{V}$, we can partition $\mathcal{V}$ into a sequence of vertices $\mathcal{V}_1, \mathcal{V}_2, \mathcal{V}_3$... such that $\mathcal{V}_0$ connects through edges only to $\mathcal{V}_1$, which connects through edges only to $\mathcal{V}_2$ (and $\mathcal{V}_0$), $\mathcal{V}_2$ connects through edges only to $\mathcal{V}_3$ (and $\mathcal{V}_1$) and so on. Through single and two-photon scattering theory [46, 60] we know that the single photon transmission spectrum $|T_{v,u}(\omega)|^2$ and second-order auto correlation function

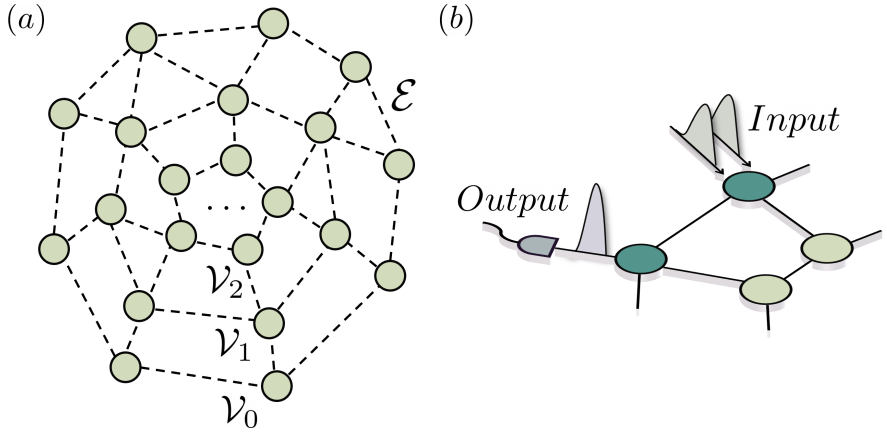

Figure 4.1: Schematic depicting the model of the photonic graph $(\mathcal{V}, \mathcal{E})$. The set $\mathcal{V} = \mathcal{V}_0 \cup \mathcal{V}_1 \cup \mathcal{V}_2 \cup \ldots$ can be broken into subsets such that $\mathcal{V}_0$ denotes the set of vertices forming the outermost boundary, $\mathcal{V}_1$ denotes the set of vertices forming the perimeter separated by one edge and so on. (b) Schematic depicting the measurement scheme where two photons are input on one of the sites in the outermost perimeter and the scattered photon wave packet is detected from an adjacent site.

$g^{(2)}(0,\omega)$ can be written as:

$$|T_{v,u}(\omega)|^2 = \gamma_v \gamma_u \left| \sum_{\alpha} \frac{\langle G|a_v|r_\alpha^{(1)}\rangle \langle l_\alpha^{(1)}|a_u^\dagger|G\rangle}{\omega - E_\alpha^{(1)}} \right|^2 \tag{4.2}$$

$$g_{v,u}^{(2)}(0,\omega) = \frac{\gamma_v \gamma_u}{|T_{v,u}(\omega)|^4} \left| \sum_{\alpha_1,\alpha_2,\alpha_3} \frac{\langle \mathrm{G}|a_v|r_{\alpha_1}^{(1)}\rangle \langle l_{\alpha_1}^{(1)}|a_v|r_{\alpha_2}^{(2)}\rangle \langle l_{\alpha_2}^{(2}|a_u^\dagger|r_{\alpha_3}^{(1)}\rangle \langle l_{\alpha_3}^{(1)}|a_u^\dagger|\mathrm{G}\rangle}{(E_{\alpha_2}^{(2)} - 2\omega)(E_{\alpha_3}^{(1)} - \omega)} \right|^2 \tag{4.3}$$

where γ_v, γ_u denote coupling rates to input/output ports at site u, v; $|l_\alpha^{(i)}\rangle, |r_\alpha^{(i)}\rangle$ denote the left and right eigenvectors of H in the i^{th} excitation subspace and $|G\rangle$ denotes the vacuum state of the lattice with zero photons. Fitting for the respective spectrum then allows determination of the eigen-energies of H within the single and two-photon subspace, $E_\alpha^{(1)}$ and $E_\alpha^{(2)}$, as well

as the coefficients:

$$M^{(1)}_{\alpha,v,u} = \langle G|a_v|r^{(1)}_\alpha\rangle\langle l^{(1)}_\alpha|a^\dagger_u|G\rangle, \tag{4.4}$$

$$M^{(2)}_{\vec{\alpha},v,u} = \langle G|a_v|r^{(1)}_{\alpha_1}\rangle\langle l^{(1)}_{\alpha_1}|a_v|r^{(2)}_{\alpha_2}\rangle\langle l^{(2)}_{\alpha_2}|a^\dagger_u|r^{(1)}_{\alpha_3}\rangle\langle l^{(1)}_{\alpha_3}|a^\dagger_u|G\rangle \ \forall\ u,v \in \mathcal{V}_0. \tag{4.5}$$

where $\vec{\alpha}$ denotes a list of coefficients $(\alpha_1, \alpha_2, \alpha_3)$. In the next sections, we propose a two-stage tomography scheme which allows reconstructing the Hamiltonian parameters $J_{v,u}$, μ_v and χ_v from single photon and two-photon boundary measurements.

4.2.2 Reconstructing J, μ

In the first stage of the scheme, we use $M^{(1)}_{\alpha,v,u}\ \forall\ v,u \in \mathcal{V}_0$ and eigen-energies $E^{(1)}_\alpha$ extracted from boundary single-photon measurements to reconstruct the linear terms of the Hamiltonian (J's, μ's). Beginning at the outermost perimeter, since we have access to all the sites in $\mathcal{V}_0$, the onsite potentials and the coupling strengths between them can be reconstructed using the standard method [45] (Fig. 4.2(a)):

$$\mu_v = \sum_\alpha E^{(1)}_\alpha M^{(1)}_{\alpha,v,v}\ , J_{v,u} = \sum_\alpha E^{(1)}_\alpha M^{(1)}_{\alpha,v,u} \tag{4.6}$$

The next step involves estimating the couplings along the edges joining $\mathcal{V}_0$ to $\mathcal{V}_1$ (Fig. 4.2(b)). While the phase of the complex couplings along the edges forming the perimeter ($\mathcal{V}_0$) is fixed by the measurements, the gauge freedom on the internal vertices leaves some arbitrariness in the phase of the remaining couplings. To fix a convenient gauge, consider first the sites in the interior of the lattice that are nearest neighbors to $\mathcal{V}_0$ — for each site, we can typically pick the phase of $J_{v,u}$ connecting it to a site on the boundary as 0. As an example, in Fig. 4.3(a), both the couplings $J_{v_1,v_1'}$ and $J_{v_2,v_2'}$ can be chosen to be positive, while in Fig. 4.3(b), only the coupling $J_{v_1,v'}$ can be chosen to be positive. Consider now a positive coupling $J_{v,v'}$, where $v \in \mathcal{V}_0$ and $v' \in \mathcal{V}_1$ — it follows straightforwardly from the eigenvalue equation for the Hamiltonian H that

$$\sum_\alpha (E^{(1)}_\alpha - \mu_v)^2 M^{(1)}_{\alpha,v,v} - \sum_{u\in\mathbb{N}_v - v'} |J_{v,u}|^2 = |J_{v,v'}|^2 \tag{4.7}$$

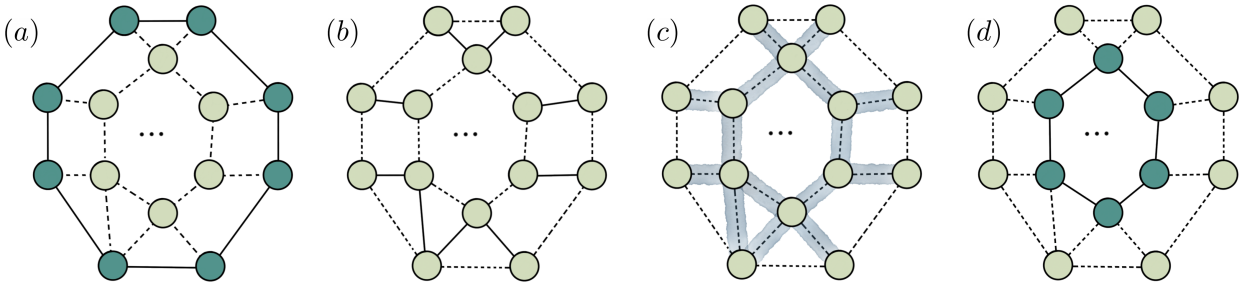

Step 1: Use boundary measurements to compute $\mu_v, J_{v,u} \forall\ u, v \in \mathcal{V}_0$

Step 2: Compute $J_{v,u}$ $\forall\ v \in \mathcal{V}_0,\ u \in\ \mathcal{V}_1$

Step 3: Compute $M^{(1)}_{\alpha,v|u,w}$ $\forall\ v \in \mathcal{V}_0, u, w \in \mathcal{V}_1$

Step 4: Repeat recursion.

Figure 4.2: Schematic depicting the tomography algorithm in the single photon space. Dark-colored sites and solid edges depict the values being computed in that step. In Step 3, shaded branches depict the sites under consideration for computing the next iteration of coefficients needed to complete the recursion.

where N_v denotes the neighborhood of site v, which is a set of all the sites separated from v by a single edge. Furthermore, the coefficients $M^{(1)}_{\alpha,v',v'}$ can now be calculated using

$$\Big[(E^{(1)}_\alpha - \mu_v)\langle v|r^{(1)}_\alpha\rangle - \sum_{u\in N_v - v'} J_{v,u}\langle u|r^{(1)}_\alpha\rangle\Big]\Big[(E^{(1)}_\alpha - \mu_v)\langle l^{(1)}_\alpha|v\rangle - \sum_{u\in N_v - v'} J^*_{u,v}\langle l^{(1)}_\alpha|u\rangle\Big]$$
$$= |J_{v',v}|^2 M_{\alpha,v',v'} \tag{4.8}$$

Similarly, the coefficients $M^{(1)}_{\alpha,v',v}$, $M^{(1)}_{\alpha,v,v'}$ can also be calculated (see Appendix A).

Next, consider a coupling $J_{v,v'}$, where $v \in \mathcal{V}_0$ and $v' \in \mathcal{V}_1$, whose phase cannot be fixed (for e.g., $J_{v_2,v'}$ in Fig. 4.3(b)). In this case, we first need to evaluate the coefficients $M^{(1)}_{\alpha,v,v'}$ so that we can then use Eq. 4.6 to determine the complex coupling $J_{v,v'}$. To calculate these coefficients, we assume that there exists a closed loop in the lattice (for e.g. $v \to v_1 \to v_2 \to \ldots v_n \to v' \to v$ in Fig. 4.3(c))) such that only coefficients corresponding to the edge in question ($M^{(1)}_{\alpha,v,v'}$) are not known. If this assumption holds true, the coefficients can be

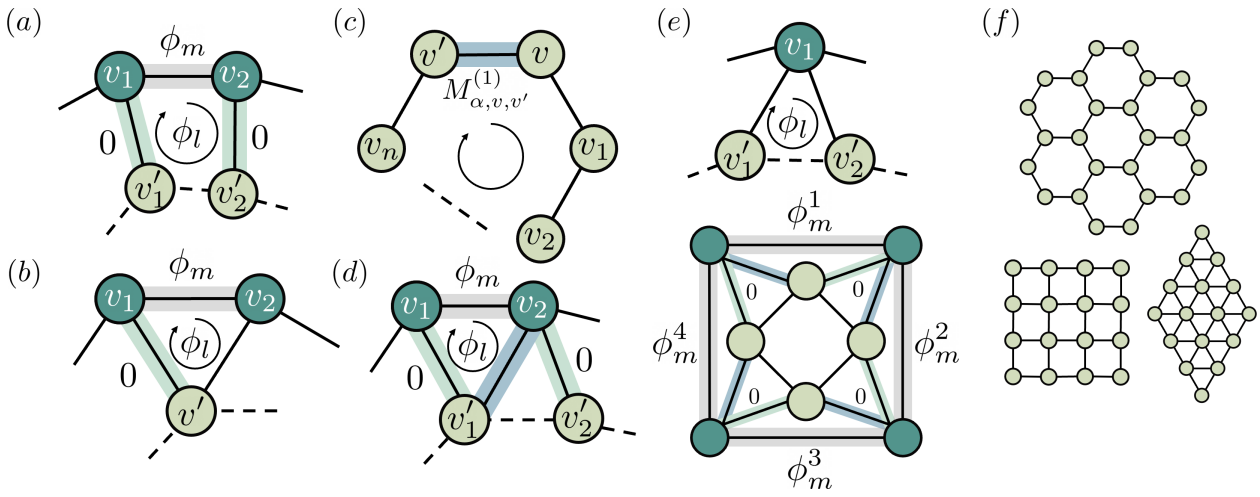

Figure 4.3: Schematic depicting photonic graphs. (a) Topology of a photonic graph where we can assume positive couplings along the edges between two perimeters (phase equals 0, shaded in green). Let, ϕ_l denote phase acquired by a photon moving in the depicted closed loop. The phase along the outer edge ϕ_m is fixed during measurement (denoted in gray). The remaining closed loop phase $\phi_l - \phi_m$ gets transferred onto the edge along the inner perimeter (dashed, unshaded) (b) Topology of a photonic graph where we cannot assume positive couplings along all the edges between the two perimeters. As soon as phase along one edge is assumed to be 0, the phase along the remaining edge gets fixed ($\phi_l - \phi_m$). (c) Schematic depicting the closed loop traversal used to calculate the coefficients $M^{(1)}_{\alpha,v,v'}$ when coefficients along all the other edges of the loop are already known. (d) Topology of a photonic graph where we can exploit the existence of a closed loop $v_1' \to v_1 \to v_2 \to v_1'$ to determine the complex coupling along the edge J_{v_1',v_2} (shaded in blue). (e) Topologies of photonic graphs where there doesn't exist closed loops that can be exploited to calculate couplings along edges with non-zero phases. (f) Honeycomb lattice, square lattice and triangular lattice which are amenable to our protocol.

calculated using the cyclical property

$$M^{(1)}_{\alpha,v,v'} = \frac{M^{(1)}_{\alpha,v,v_1}\left(\prod_1^{n-1} M^{(1)}_{\alpha,v_i,v_{i+1}}\right) M^{(1)}_{\alpha,v_n,v'}}{\prod_1^n M^{(1)}_{\alpha,v_i,v_i}} \tag{4.9}$$

A typical topology where this assumption holds is depicted in Fig. 4.3(d). To solve this construction, the coupling along $J_{v_1,v_1'}$ can be chosen to be positive and be calculated using Eq. 4.7. As the site $v_2 \in \mathcal{V}_0$ is connected to two sites in the inner perimeter ($v_1', v_2' \in \mathcal{V}_1$), the couplings along these edges can't both be chosen to be positive. But as there does exist the closed loop, $v_1' \to v_1 \to v_2 \to v_1'$, we can calculate the complex coupling J_{v_1',v_2} using the cyclical property (Eq. 4.9). Then the remaining coupling J_{v_2',v_2} can be chosen to be positive and determined using Eq. 4.7. This methodology however falters, if there doesn't exist a closed loop in the lattice that will allow us to determine one of these couplings without choosing it to be positive. Two possible cases where this situation might arise are depicted in Fig. 4.3(e) in which case our algorithm can not be used to reconstruct the Hamiltonian. In the first case (top), we have a site in the outer perimeter connected to two sites in the inner perimeter, with no other existing edge connecting these sites to parts of the lattice that have already been determined. This means that there doesn't exist a closed loop which allows us to determine the coefficients and hence the coupling along one of these edges. The second case is slightly tricker, as at first glance it may seem that closed loops similar to the topology in depicted in Fig. 4.3(d) exist in this graph. However, on closer inspection, we can see that none of these loops have an edge that can be first solved using Eq. 4.7 and then be used to calculate other edges using the cyclical property, implying that we cannot solve this/similar constructions.

Finally, the last step involves estimating the coefficients $M^{(1)}_{\alpha}$ for sites in the inner perimeter ($\mathcal{V}_1$) which we would have obtained if we had measurement access to these sites (Fig. 4.2(c)). These coefficients $M^{(1)}_{\alpha,v,u}\ \forall\ v \in \mathcal{V}_1, u \in \mathbb{N}_v$ can again be calculated by exploiting the cyclical relation between the $M^{(1)}_{\alpha}$s, as coefficients along all the edges connecting the perimeters $\mathcal{V}_0$ and $\mathcal{V}_1$ were already determined in the last step. For example, in Fig. 4.3(a) the coefficients $M^{(1)}_{\alpha,v_1',v_2'}$ for $v_1', v_2' \in \mathcal{V}_1$ can be calculated by traversing the path $v_1' \to v_1 \to v_2 \to v_2'$.

This then completes the recursion, and the same process can be repeated starting from perimeter $\mathcal{V}_1$ and moving inwards until the entire Hamiltonian in single-photon space i.e. $H^{(1)}$ is mapped successfully (Fig. 4.2(d)). Despite the mentioned limitation, the outlined algorithm allows tomography of most experimentally relevant graphs with complex couplings, laid out in the square, triangular and honeycomb topologies (Fig. 4.3(f)) mimicking topological phenomena like the optical delay lines [31, 57] and the topological quadrupole phases [14]. This is in stark contrast to previous works dealing with limited access tomography algorithms [45, 47–49] which were restricted to graphs with real couplings or 1D chains only.

4.2.3 Reconstructing χ

The second stage involves working in two-photon space using the determined $H^{(1)}$ and the measured values of $M_\alpha^{(2)}$ to calculate $\chi_v \ \forall \ v \in \mathcal{V}$ and hence mapping the full Hamiltonian H. Similar as above, we work perimeter by perimeter to determine the non-linear part of the Hamiltonian. Before running this part of the algorithm, we use the measured $M_\alpha^{(2)}$s to calculate the operators $\hat{O}^{(2)}_{\alpha_2,u,v} \ \forall \ u, v \in \mathcal{V}_0$. This can be done as:

$$\hat{O}^{(2)}_{\alpha_2,u,v} = \sum_{\alpha_1,\alpha_3} \frac{|r^{(1)}_{\alpha_1}\rangle\langle l^{(1)}_{\alpha_3}| M^{(2)}_{\vec{\alpha},u,v}}{\langle G|a_v|r^{(1)}_{\alpha_1}\rangle\langle l^{(1)}_{\alpha_3}|a_u^\dagger|G\rangle} \tag{4.10}$$

where we use the reconstructed $H^{(1)}$ from the first stage of the scheme to get the eigenvectors $|r^{(1)}_{\alpha_1}\rangle, |l^{(1)}_{\alpha_3}\rangle$. The obtained operators are then used to calculate coefficients, $C^{(2)}_{\vec{\alpha},u,v} = \langle l^{(1)}_{\alpha_1}|\hat{O}^{(2)}_{\alpha_2,v,u}|r^{(1)}_{\alpha_3}\rangle \ \forall \ u, v \in \mathcal{V}_0$ which are used to reconstruct the χ's.

Again, beginning at the outermost perimeter $\mathcal{V}_0$, $\chi_v \ \forall \ v \in \mathcal{V}_0$ can be estimated using the following relation with $\alpha_1 = \alpha_3$:

$$\chi_v = -\frac{1}{2}\sum_{\alpha_1,\alpha_2} (\mu_v + E^{(1)}_{\alpha_1} - E^{(2)}_{\alpha_2}) C^{(2)}_{\vec{\alpha},v,v} \tag{4.11}$$

Then, as in the first stage of the scheme, the next step involves calculating the coefficients $C^{(2)}_{\vec{\alpha},v,v'}$, $C^{(2)}_{\vec{\alpha},v,v'}$ and $C^{(2)}_{\vec{\alpha},v,v'} \forall \ v \in \mathcal{V}_0, v' \in \mathcal{V}_1$ along the edges joining the two perimeters. The

coefficients $C^{(2)}_{\vec{\alpha},v',v'}$ can for example be calculated using

$$C_{\vec{\alpha},v',v'} = -\frac{1}{J_{v,v'}}\left(\sum_{u\in N_v - v'} J_{v,u}C_{\vec{\alpha},u,v'} + \chi_v Q_{\vec{\alpha},v,v'} + (\mu_v + E^{(1)}_{\alpha_1} - E^{(2)}_{\alpha_2})C_{\vec{\alpha},v,v'}\right) \tag{4.12}$$

where $Q_{\vec{\alpha},v,v'} = \langle l^{(1)}_{\alpha_1}|(a^\dagger_v a_v)a_v|r^{(2)}_{\alpha_2}\rangle\langle l^{(2)}_{\alpha_2}|a^\dagger_{v'}|r^{(1)}_{\alpha_3}\rangle$ which can be determined using the coefficients $C_{\vec{\alpha},v,v'}$ by reverting to the operators $\hat{O}^{(2)}_{\alpha_2,v,v'}$ and multiplying by an additional $(a^\dagger_v a_v)$ before taking projections on $|l^{(1)}_{\alpha_1}\rangle$, $|r^{(1)}_{\alpha_3}\rangle$ to obtain $Q_{\vec{\alpha},v,v'}$. Similarly, the coefficients $C^{(2)}_{\vec{\alpha},v,v'}$, $C^{(2)}_{\vec{\alpha},v',v}$ can also be evaluated (see Appendix B).

Finally, the last step involves calculating the coefficients for all sites lying in the inner perimeter ($C^{(2)}_{\vec{\alpha},v,u}\ \forall\ v,u \in \mathcal{V}_1$). These can now be calculated using the cyclical property of coefficients $C^{(2)}_{\vec{\alpha}}$s and traversing a closed loop in the lattice (for e.g. $v \to v_1 \to v_2 \to \dots v_n \to u \to v$), where except for the edge of interest $\{v,u\}$, the coefficients along all the other edges ($C^{(2)}_{\vec{\alpha},v_i,v_{i+1}}$) in the loop are already known. This can be done by ensuring that the remaining edges are either part of the outer perimeter or connect the two perimeters. Then $C^{(2)}_{\vec{\alpha},v,u}$ can be calculated by cyclical property,

$$C^{(2)}_{\vec{\alpha},v,u} = \frac{C^{(2)}_{\vec{\alpha},v,v_1}\left(\prod_1^{n-1} C^{(2)}_{\vec{\alpha},v_i,v_{i+1}}\right)C^{(2)}_{\vec{\alpha},v_n,u}}{\prod_1^n C^{(2)}_{\vec{\alpha},v_i,v_i}} \tag{4.13}$$

This completes the recursion, and we can repeat the process for all the perimeters until all the χs are determined.

4.2.4 Stability analysis

In real life scenarios, due to measurement errors/noise even in the ideal case, we cannot determine observable expectation values perfectly since we need to average over many runs. So, we need to understand how the reconstructed Hamiltonian parameters diverge from true ones when measurements contain errors. The primary inputs into the first-stage of our algorithm are the eigenenergies and the coefficients $M^{(1)}_{\alpha,v,u}$. We know that the eigenvalues are the poles of our measurements and, hence, for a well calibrated setup we assume that these can typically be determined more accurately than the coefficients. Hence, we focus

on determining scaling of the error in the reconstructed couplings with the error in the coefficients. About the point of zero error for an arbitrary hopping rate $J_{v,u}$ being estimated we can write that:

$$\delta J_{v,u} = \sum_{\alpha,v',u'} \frac{\partial J_{v,u}}{\partial M^{(1)}_{\alpha,v',u'}} \delta M^{(1)}_{\alpha,v',u'} \tag{4.14}$$

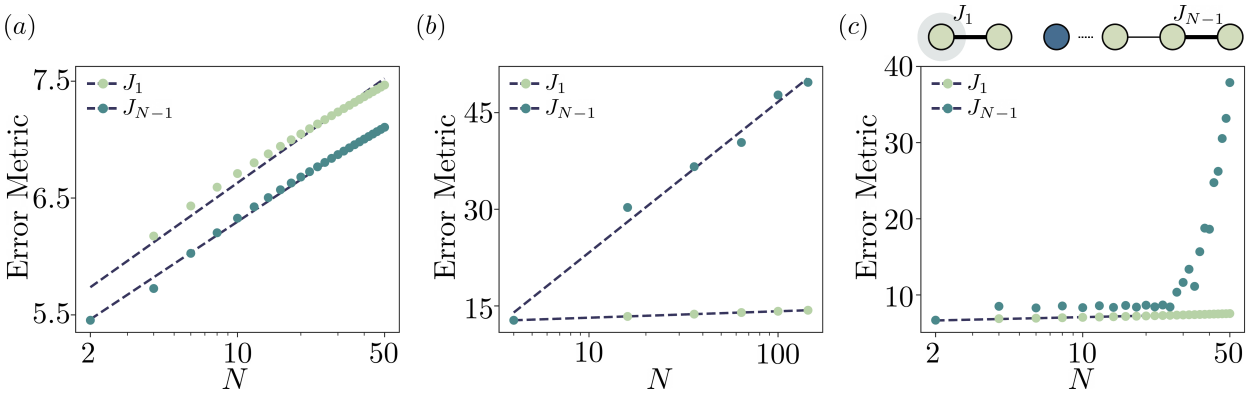

Figure 4.4: Stability analysis. x-axis denotes number of sites in the array on a log scale, y-axis denotes the error metric (a) Error metric plot for a SSH chain with $J_1/J_2 = 1.2$ with fitted b values being $b = 1.28,\ 1.19$ for J_1, J_{N-1} respectively. (b) Error metric plot for a SSH $2D$ lattice with $J_1/J_2 = 1.2$. Each point is in 100 point average with disorder in onsite potentials to be 10 MHz to avoid absolute degeneracies. The fitted b values are $b = 1,\ 23.4$ for J_1, J_{N-1} respectively. (c) Top: Schematic depicting the measurement scheme for 1D SSH with a defect site at $N/2$ s.t. $\mu_{N/2} = \mu_{N/2} + 2J_1$. Error metric plot s.t. $J_1/J_2 = 1.2$. The fitted b value for J_1 is $b = 0.62$. However, error metric for J_{N-1} depicts a breakdown in stability.

Then assuming that errors in the coefficients are independent i.e. $\langle \delta M^{(1)}_{\alpha,v'_1,u'_1} \delta M^{(1)}_{\alpha,v'_2,u'_2} \rangle = 0$ as we are dealing with errors at different frequencies, we can define an error metric that is the logarithm of average first order error about the point of zero error if we assume random

Gaussian errors in the coefficients:

$$\text{Error metric} = \log_{10}\left(\sum_{\alpha,v',u'}\left|\frac{\partial J_{v,u}}{\partial M^{(1)}_{\alpha,v',u'}}\right|^2\right) \tag{4.15}$$

Then, the stability of the algorithm in estimating the arbitrary hopping rate $J_{v,u}$ due to errors in experimentally extracted coefficients $M^{(1)}_{\alpha,v,u}$ depends on the behavior of the error metric with number of nodes in graph (N). If the algorithm is stable with increasing number of sites N then the defined error metrics should scale as $a + b\log(N)$ as this would imply a polynomial scaling in the number of measurements needed to attain a specific precision.

To illustrate how the metric scales with increasing N we take up a model Hamiltonian, for example here Su-Schrieffer-Heeger (SSH) model [35]. The SSH Hamiltonian is characterized with a graph with uniform onsite potentials but alternate coupling strengths between the sites. In Fig. 4.4 (a) we take a SSH chain with real coupling strengths and plot the behavior of the error metric for the coupling strengths along the first and last edge in the chain. From the plot, we can see that the metric scales sub-linearly with N. This suggests that even though the amount of error in the reconstructed coupling strengths increase with N, we only need a polynomial increase in the number of measurements to accurately determine the Hamiltonian in question. We show the same for a $2D$ SSH model in Fig. 4.4 (b). Finally, we take an example of a SSH chain with a defect in the middle such that the onsite potential of this site is greater than two times the maximum hopping rate in the chain. This means there will exist a defect state in the lattice that will decay as we approach the edge site at which measurements can be performed. Hence, we expect that in this case there will exist a N after which a small error in the measurement of coefficients will lead to a blow up in the error of the estimated coupling strengths. We plot this case in Fig. 4.4 (c). We confirm from the plot that after a specific N the error metric scales polynomially implying that an exponentially large number of measurements will be needed to accurately determine the realized Hamiltonian after this point.

The second-stage of the tomography scheme involving reconstruction of χs, however, is not demonstrably stable (see Appendix B) and hence in principle can only be applied to lattices

with a few sites. But, if we assume an additional capability in the system under investigation, such that the onsite non-linearity can be toggled on/off during the experiment at all nodes, there exists a modification of the algorithm that remains stable irrespective of the system size N. The assumption of control over onsite non-linearity is generally valid for most on-chip typical quantum simulators, as local tunability is a necessity in order to precisely program the terms of the Hamiltonian being implemented [61]. In these systems, obtaining concurrent local measurability with local control is experimentally challenging due to the difficulty in placing impedance matched read-out resonators (for superconducting systems) or lossless waveguides (for photonics) in proximity of the densely packed resonator arrays used to realize these bosonic lattices [10,11,13,41,46]. Hence, our modification that overcomes this issue can be useful for tomography of non-linearities in such bosonic lattices. Under this assumption, the non-linearity for any site $v \in \mathcal{V}$ can be calculated as:

$$\chi_v = \mathrm{Tr}(H) - \mathrm{Tr}(H_{v,off}) = \sum_{\alpha} \left(E^{(2)}_{\alpha} - E^{(2)}_{\alpha,v,off} \right) \tag{4.16}$$

where $E^{(2)}_{\alpha,off}$ denotes the eigenenergies in two-photon subspace of the lattice measured at the boundaries with non-linearity at site v: χ_v turned off, $H_{v,off}$ denotes the corresponding system Hamiltonian. This modification will then allow us to determine the entire non-linear part of the Hamiltonian in a stable manner.

4.3 Quantum enhanced tomography

It can then be asked if we can achieve an improvement in this precision by utilizing non-classical states of photons. In this subsection we show that, if we impose a few additional restrictions on the system being studied, we can reduce the rate in scaling of photons needed in comparison to the classical interferometry to obtain an Δ precision in measurement by utilizing quantum mechanical enhancement due to the entangled nature of the input photons. Particularly, we make the assumptions that the lattices in question are lossless; we have control over the number of input/output ports of the system and; that the onsite non-linearity can be arbitrarily turned on/off during the experiment at all nodes. Then, our

proposition for this entanglement enhanced protocol is as that the Hamiltonian parameters $J_{v,u}$, μ_v and χ_v for a fixed number of sites, can be obtained with a precision Δ from just boundary quantum interferometry measurements using $N00N$ states of $O(\Delta^{-2/3})$ photons. The quantum-mechanical enhancement in obtaining the linear part of the Hamiltonian follows straightforwardly from scattering of P photon $N00N$ states from the lattice via the input/output ports while non-linearity is turned off for the entire lattice. This allows us to quadratically enhance the precision in measurement of the scattered phase from the lattice, which enhances the precision in measurement of coefficients $M_\alpha^{(1)}$. Obtaining enhancement in precision of non-linearities χ_v's can be more challenging if we use P photon Fock state scattering from the system while the non-linearities are all turned on, as the output state would then be a mixed P photon state from which extracting χ_v becomes extremely hard. Hence, we propose the following protocol to obtain enhancement in measuring the non-linearities in the system. Let's say we want to estimate non-linearity χ_v at a site $v \in \mathcal{V}$, then we carry out the following steps:

(i) Step 1: With the non-linearity turned off, initialize the system in a superposition of vacuum and P photon Fock state at site v i.e. $(1 + \frac{a_v^{\dagger P}}{\sqrt{P!}})|G\rangle$. The input photon wave packet needed to initialize the system in this state can be pre-designed by reversing the emitted wave packet from the lattice when a photon on vertex v decays into the output port at the boundary. We assume that it takes a finite amount of time for such an initialization to be performed.

(ii) Step 2: Turn on the non-linearity χ_v at site v for a time period $T_{on} \propto \frac{1}{\sqrt{P!}}$. Within this time the photons will not diffuse to the neighboring sites and the state of the lattice will be

$$|\psi\rangle \approx \left(1 + e^{-j(\mu_v P + \chi_v \frac{P(P-1)}{2})T_{on}} \frac{a^{\dagger P}}{\sqrt{P!}}\right)|G\rangle \tag{4.17}$$

(iii) Step 3: Use an interferometry setup to measure the operators

$$\hat{O}^c = |P\rangle\langle 0| + |0\rangle\langle P| \text{ and} \tag{4.18}$$

$$\hat{O}^s = j(|P\rangle\langle 0| + |0\rangle\langle P|) \tag{4.19}$$

k times each at the output port. The operators are chosen such that

$$\langle \hat{O}^c \rangle_{|\psi\rangle} = \cos\left(\mu_v P + \chi_v \frac{P(P-1)}{2}\right) \text{ and} \tag{4.20}$$

$$\langle \hat{O}^s \rangle_{|\psi\rangle} = \sin\left(\mu_v P + \chi_v \frac{P(P-1)}{2}\right) \tag{4.21}$$

(iv) Step 4: Comparing $\langle \hat{O}^c \rangle_{|\psi\rangle}$ or $\langle \hat{O}^s \rangle_{|\psi\rangle}$, we choose the lesser of these to invert to obtain χ_v.

It can be shown that the above algorithm is provably stable even for the case in which the error in the reconstructed Hamiltonian in the first excitation space $H_{rc}^{(1)}$ is finite, i.e. $\|H^{(1)} - H_{rc}^{(1)}\|_F^2 \leq \delta N$. We can also prove that the protocol allows us to have worst case scaling of $O(\Delta^{-2/3})$ in number of photons needed for obtaining Δ precision in Hamiltonian parameters (see Appendix C for the proofs).

Finally, to demonstrate the quantum-enhanced protocol, we take a $1D$ chain made of five sites and estimate the non-linearity at the middle site (Fig. 4.5(a)) by doing a full quantum simulation [62]. We then plot how our estimated non-linearity value ($\chi_{est.}$) varies with the time for which non-linearity was turned-on (T_{on}) and the number of photons in the Fock state used for measurement (Fig. 4.5(b)). We expect that for very small turn on time T_{on} the estimated value will be very erroneous as the acquired phase by the lattice wavefunction will initially be dominated by measurement error and for a range of T_{on} predominantly depend only on the onsite potential μ_v. As the turn-on time increases, we expect the error in the estimated $\chi_{est.}$ to decrease due to its increasing contribution to the overall phase. However, past an optimal turn-on time we will start seeing diffusion of photons to neighboring sites, which acts as a source of error in our protocol. Hence, we expect there to exist an optimal turn-on time window for us to accurately estimate the non-linearity χ_v of the sites forming the lattice. This behavior is confirmed from our simulation results as well. Additionally, we also expect the protocol to perform better as the number of photons in the input Fock state P increase, which is also observed in our simulated plot.

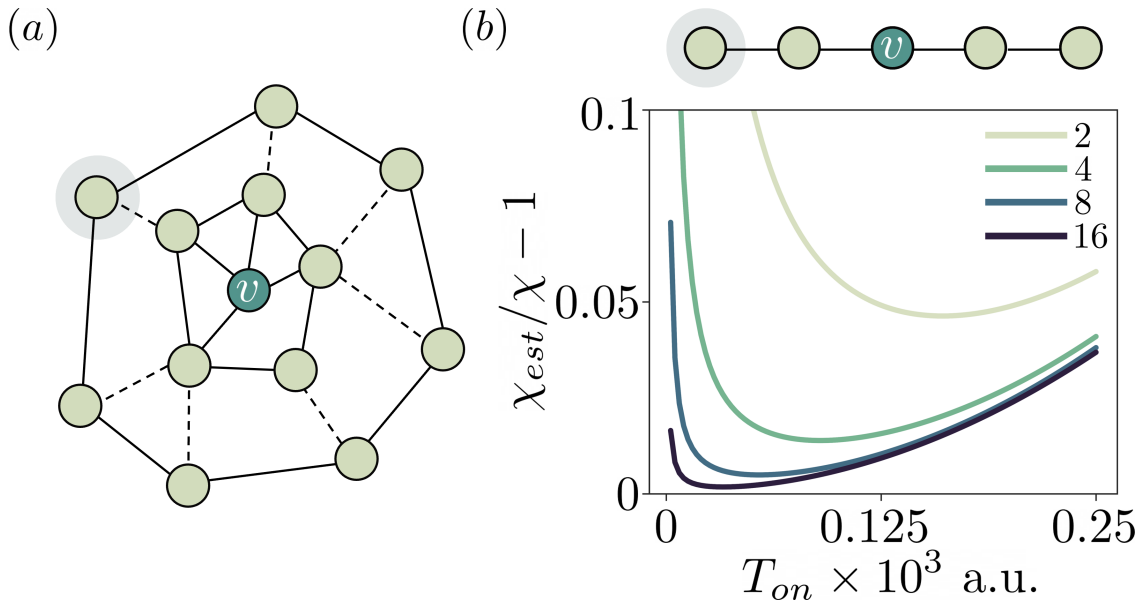

Figure 4.5: Quantum enhancement protocol. (a) Schematic showing the lattice with one output port (background shaded) at the outermost perimeter and the site v whose non-linearity χ_v is being determined.(b) Schematic showing the simulated chain. $J_{mean} = 95.5\ 1/a.u.$, $\sigma_J = 3.64\ 1/a.u.$, $\chi_v = 10\ 1/a.u.$. The colors denote the number of photons P in the input state.

4.4 Conclusion

In this chapter, we developed an algorithm for tomography of non-linear topological quantum bosonic lattices with measurement accessibility only to the perimeter of the lattice. We numerically demonstrated the stability of our algorithm and then proposed an extension to the algorithm to quantum mechanically enhance the precision of the estimated Hamiltonian. Further, we analytically proved the stability of our quantum enhanced protocol to errors in reconstructing the linear part of the Hamiltonian. In the future, the algorithm can also be extended to included other quantum simulation platforms like spin chains. Another direction of interest for exploration can include the studying protocols to tomographically probe emitters coupled to such photonic lattices.

Chapter 5

CONTROLLABILITY

The contents of this chapter are adapted from [46]; *Abhi Saxena, Arnab Manna, Rahul Trivedi, and Arka Majumdar. "Realizing tight-binding Hamiltonians using site-controlled coupled cavity arrays" arXiv:2210.05070 (2022)*; with permission from the authors.

5.1 Introduction

In the previous two chapters, we demonstrated how photonic CCAs can be scaled and developed tomography protocols that allowed us to map the realized Hamiltonians with access to sites forming the outermost boundary only. In this chapter, one of the things we propose is to experimentally test the tomography algorithm. Secondly, we aim to address the third requirement of making photonic CCAs suitable for quantum simulation: adding controllability: i.e., control over all the terms describing the Hamiltonian being implemented. However, we need to do so while guaranteeing that it does not negatively impact the scalability or measurability, and additionally ensuring that the ensuing device design allows for future integration with non-linear optical materials to operate in the quantum non-linear regime. These added demands, as a precondition, necessitate using high-quality factor (Q) cavities with small mode volumes as constituents of the CCA to maximize the strength of non-linear interactions and allow probing of the entire quantized eigenenergy spectra. Though several experiments showing various physical phenomena using optical CCAs have been previously reported [12, 63, 64], none of these CCAs are programmable and have access to the entire quantized eigenenergy spectra of the Hamiltonian. In the optical regime, achieving programmability and measurability of the eigen-spectrum concurrently is very challenging owing to the extremely small physical dimensions involved.

Here, we tackle these problems by engineering a silicon photonic CCA made of high-Q (intrinsic Qs up to 7.1×10^4) racetrack resonators with thermally controllable onsite potential using specially designed thermo-optic (TO) island heaters. We specifically focus on 1D tight-binding lattices which can be described by a set of Gaussian Hamiltonians of the form ($\hbar = 1$):

$$H = \sum_n \mu_n a_n^\dagger a_n + J_n(a_{n+1}^\dagger a_n + a_n^\dagger a_{n+1}) \tag{5.1}$$

where a_n denotes the onsite photonic annihilation operator, μ_n is the onsite potential given by the resonant frequency of the cavity, J_n is the photonic hopping rate between n^{th} and $(n+1)^{th}$ sites. Realization of such a set of Hamiltonians requires implementing a potential profile $[\mu_n] = [\mu_0, \mu_1, \ldots \mu_{N-1}]$ across a photonic lattice with specific inter-site hopping rates J_n, while ensuring that all the eigenstates of the system denoted by $[\epsilon_n] = [\epsilon_0, \epsilon_1, \ldots \epsilon_{N-1}]$ remain addressable and measurable.

5.2 Device description & optical design

Experimentally, we implement a Hamiltonian with 8 nodes via a CCA made up of 8 strongly coupled racetrack resonators fabricated on a silicon-on-insulator platform using 220 nm silicon on top of 3 μm thick silicon oxide (Fig. 5.1a). The spacing between the resonators is determined by the desired hopping rate between the sites for the tight binding Hamiltonians being implemented. The spectrum of the resulting system is probed via a set of grating couplers located at the first and last sites. The scattering properties of this system are completely described by the effective non-Hermitian Hamiltonian, which incorporates the coupling to input/output ports and system losses as:

$$H_{eff}^0 = H - j\left(\frac{\gamma_0}{2} a_0^\dagger a_0 + \frac{\gamma_{N-1}}{2} a_{N-1}^\dagger a_{N-1}\right) - j\sum_n \frac{\kappa_n}{2} a_n^\dagger a_n \tag{5.2}$$

where γ_0, γ_{N-1} denote the coupling rates to the grating couplers and κ_n denotes the onsite scattering/absorption losses. In the next subsections, we briefly touch upon a few key aspects of the design of the optical layer of the device:

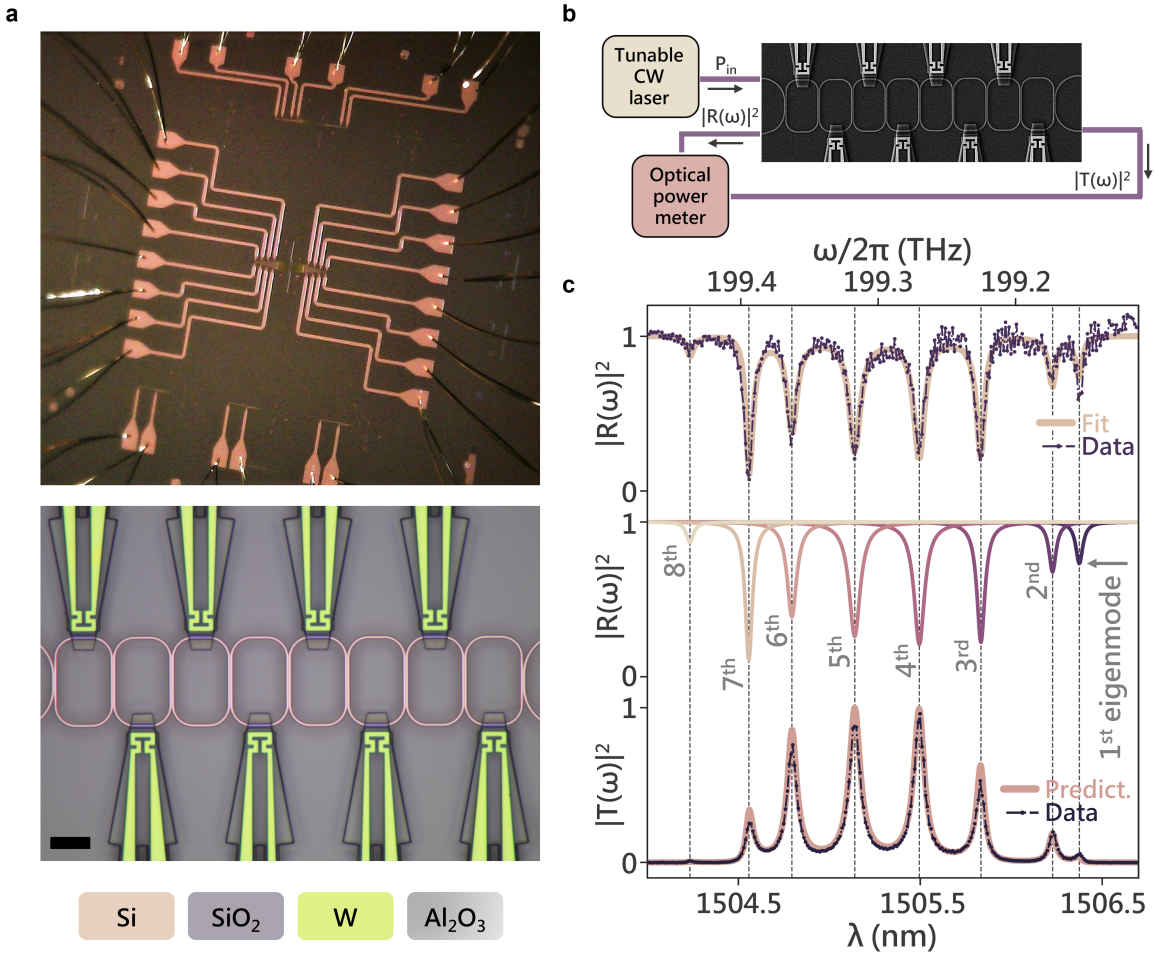

Figure 5.1: Hamiltonian Tomography. (a) Optical image of the electrically controlled CCA depicting the wiring structure, optical micrograph of the CCA (scale bar: 10 μm). The constituent racetrack resonators are characterized by longer straight segments that are 12 μm long, shorter straight segments that are 4 μm long, and a bending radius of 5 μm. (b) Schematic of the experimental setup used for measuring reflection ($|R(\omega)|^2$) and transmission ($|T(\omega)|^2$) spectra. (c) From the top: measured reflection spectrum $|R(\omega)|^2$ (dotted purple) along with the fit generated using the tomography algorithm (cream); followed by a plot showing contributions of various eigenmodes of the system to $|R(\omega)|^2$, and finally at the bottom; experimentally measured transmission spectrum $|T(\omega)|^2$ (dotted purple) along with the predicted transmission spectrum $|T(\omega)|^2$ (pink) from the H^0_{eff} obtained using tomography algorithm.

5.2.1 Waveguide modes

The racetrack resonators have two differing waveguide sections: (i) a standard ridge waveguide section which is 554 nm wide with an 82° slant and (ii) and an embedded waveguide section where the resonator makes thermal contact with the heater through the bottom alumina layer of the island heaters. The simulated optical mode profile (using ANSYS Lumerical MODE) for both these sections is plotted in Fig. 5.2. The simulated waveguide losses are 9.2×10^{-13} dB/cm and, 7.8×10^{-9} dB/cm respectively. As evident the loss is negligible even for the heater integrated design as we were able to utilize the bottom alumina platform (which is 265 nm thick) to place the tungsten heater both above the plane of the optical mode and at a far enough (1.5 μm) lateral distance to ensure minimal increase in the absorption losses.

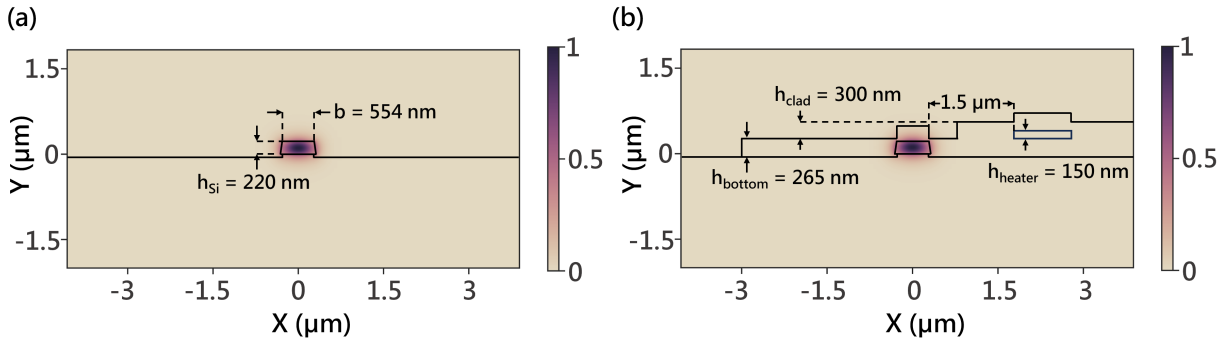

Figure 5.2: Waveguide mode profiles ($|E|^2/|E|^2_{max}$). (a) Profile of the waveguide mode in the sections without any cladding layers. The effective index of the mode is $n_{eff} = 2.556$ and the group index is $n_g = 4.13$. The simulated loss is 9.213×10^{-13} dB/cm. A lateral undercut of 27 nm occurs during the BOE strip of HSQ resist. (b) Profile of the waveguide mode where the resonator makes thermal contact with the island heaters with the tungsten heating element being 1 μm wide. The effective index of the mode is $n_{eff} = 2.61$ and the group index is $n_g = 4.006$. The simulated loss is 7.75×10^{-9} dB/cm.

5.2.2 Hopping rates

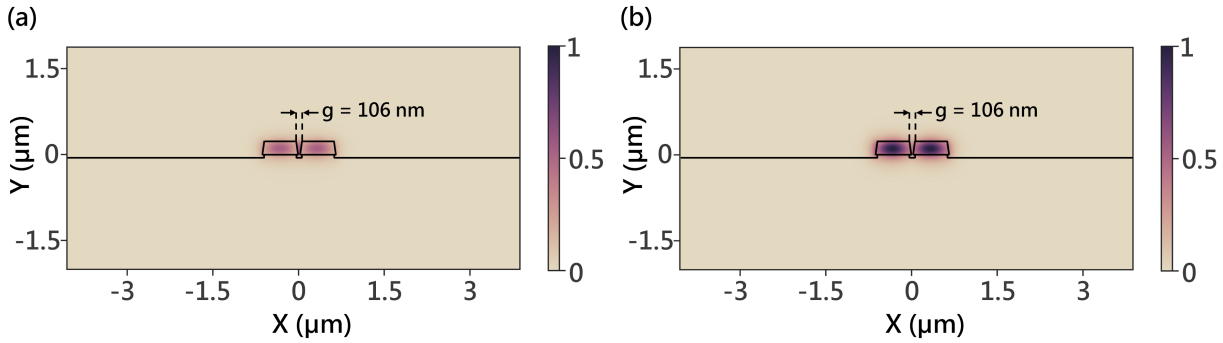

Figure 5.3: Coupled waveguide mode profiles ($|E|^2/|E|^2_{max}$). (a) Mode profile of the first coupled waveguide mode, $n_{eff} = 2.568$. (b) Mode profile of the second coupled waveguide mode, $n_{eff} = 2.5525$. $\Delta n_{eff} \approx 0.0155$.

Another aspect of the optical design deals with the interplay of the physical spacing between the resonators and the corresponding hopping rates between the sites. As the waveguides forming the coupling region of neighboring resonators in a CCA lie in close proximity, their respective modes overlap with each other to create two coupled modes as depicted in Fig. 5.3. Their coupling constant k can be estimated numerically by simulating the eigenmodes of the two adjacent waveguides and is given by the following relation:

$$k = sin(\frac{\pi \Delta n_{eff}}{\mu^{\lambda}} L_{coupling}) \tag{5.3}$$

where Δn_{eff} is the difference between the effective indices of the coupled waveguide modes, $L_{coupling}$ is the coupling length of the resonators and μ^{λ} is the resonant wavelength of the resonator. Given the coupling constant between the coupled waveguide sections, the corresponding hopping rate between the resonators (assuming no disorder) can then be calculated using the following relation [65, 66]:

$$J = \frac{kv_g}{L_{resonator}} \tag{5.4}$$

where v_g denotes the group velocity of the waveguide mode and the $L_{resonator}$ denotes the length of resonator. Combing these two equations, the estimated hopping rate between the resonators can be written as

$$J = sin(\frac{\pi \Delta n_{eff}}{\mu^{\lambda}} L_{coupling}) \frac{c}{n_g L_{resonator}} \tag{5.5}$$

Note that we have substituted $v_g = c/n_g$ where n_g denotes the group index of the waveguide mode, and the hopping rate J is obtained in units of rad/s. Substituting for the values we get $J \approx 69.1\ GHz$.

5.3 Hamiltonian tomography

Photonic CCAs on a 2D chip can only be accessed reliably through input/output ports at the device boundaries, and hence require a protocol that allows determination of the realized Hamiltonians with this boundary-restricted access. To map the initial Hamiltonian H^0_{eff} of our CCA post-fabrication, we apply the Hamiltonian tomography algorithm described in the last chapter for application in 1D nearest neighbor lossy CCAs. Specifically, the modified algorithm allows for determining the entire H^0_{eff} describing the system from a single reflection spectrum measurement $|R(\omega)|^2$ (Fig. 5.1b) performed at the first site of the CCA by estimating the contribution of individual eigenmodes of the system to the measured spectrum. In Fig. 5.1c, we plot the reflection spectrum of our CCA along with the corresponding contributions of the 8 individual eigenmodes. We then verify the accuracy of our fit by comparing the experimentally measured transmission spectrum $|T(\omega)|^2$ of the CCA to the predicted spectrum of the extracted H^0_{eff}. Note that, while the reflection spectrum is needed to map the entire H^0_{eff}, the transmission spectrum can be used to find only the eigenvalues of the Hamiltonian.

5.3.1 The algorithm

In this subsection, we discuss the specific version of the general algorithm discussed in Ch. 4 which we used for reconstruction of the effective Hamiltonian of our 1D CCA. For a coupled cavity array with N racetrack resonators with grating couplers at first and last sites, the non-interacting system Hamiltonian H is given by Eq. 5.1. Then using input-output formalism we can write:

$$\frac{\mathrm{d}a_0}{\mathrm{d}t} = -j(\mu_0 a_0 + J_0 a_1) - \frac{\kappa_0}{2}a_0 - \frac{\gamma_0}{2}a_0 - \sqrt{\gamma_0}x_0, \tag{5.6}$$

$$\frac{\mathrm{d}a_n}{\mathrm{d}t} = -j(\mu_n a_n + J_{n-1}a_{n-1} + J_{n+1}a_{n+1}) - \frac{\kappa_n}{2}a_n, \text{ where } n = 1, 2, \ldots N-2 \tag{5.7}$$

$$\frac{\mathrm{d}a_{N-1}}{\mathrm{d}t} = -j(\mu_{N-1} a_{N-1} + J_{N-2}a_{N-2}) - \frac{\kappa_{N-1}}{2}a_{N-1} - \frac{\gamma_{N-1}}{2}a_{N-1} \tag{5.8}$$

where κ_n denotes the loss rate to environment at each site, γ_n denotes the coupling rate to the grating couplers, x_0 denotes the destruction operator of the input into the system. The system can be visualized with the aid of the schematic depicted in Fig. 5.4.

Taking Fourier transform on these equations gives:

$$-j\omega a_0 = -j(\mu_0 a_0 + J_0 a_1) - \frac{\kappa_0}{2}a_0 - \frac{\gamma_0}{2}a_0 - \sqrt{\gamma_0}x_0, \tag{5.9}$$

$$-j\omega a_n = -j(\mu_n a_n + J_{n-1}a_{n-1} + J_{n+1}a_{n+1}) - \frac{\kappa_n}{2}a_n, \text{ where } n = 1, 2, \ldots N-2 \tag{5.10}$$

$$-j\omega a_{N-1} = -j(\mu_{N-1} a_{N-1} + J_{N-2}a_{N-2}) - \frac{\kappa_{N-1}}{2}a_{N-1} - \frac{\gamma_{N-1}}{2}a_{N-1} \tag{5.11}$$

Rearranging the terms gives:

$$\sqrt{\gamma_0}x_0 = j\left(\omega - \left(\mu_0 - j\frac{\kappa_0}{2} - j\gamma_0 2\right)\right)a_0 - jJ_0 a_1, \tag{5.12}$$

$$0 = j\left(\omega - \left(\mu_n - j\frac{\kappa_n}{2}\right)\right)a_n - j(J_{n-1}a_{n-1} + J_n a_{n+1}), \text{ where } n = 1, 2, \ldots N-2 \tag{5.13}$$

$$0 = j\left(\omega - \left(\mu_{N-1} - j\frac{\kappa_{N-1}}{2} - j\gamma_{N-1}2\right)\right)a_{N-1} - jJ_{N-2}a_{N-1} \tag{5.14}$$

Writing as a matrix: .

$$j\begin{pmatrix} \omega-(\mu_0-j\frac{\kappa_0}{2}-j\frac{\gamma_0}{2}) & -J_0 & 0 & 0 & \dots \\ -J_0 & \omega-(\mu_n-j\frac{\kappa_n}{2}) & -J_1 & 0 & \dots \\ \ddots & \ddots & \ddots & \ddots & \vdots \\ \dots & \dots & 0 & -J_{N-2} & \omega-(\mu_{N-1}-j\frac{\kappa_{N-1}}{2}-j\frac{\gamma_{N-1}}{2}) \end{pmatrix}\begin{pmatrix} a_0 \\ a_1 \\ \vdots \\ a_{N-1} \end{pmatrix} = \begin{pmatrix} \sqrt{\gamma_0}x_0 \\ 0 \\ \vdots \\ 0 \end{pmatrix} \tag{5.15}$$

Further, we can define H_{eff} as .

$$H_{eff} = \begin{pmatrix} \omega-(\mu_0-j\frac{\kappa_0}{2}-j\frac{\gamma_0}{2}) & -J_0 & 0 & 0 & \dots \\ -J_0 & \omega-(\mu_n-j\frac{\kappa_n}{2}) & -J_1 & 0 & \dots \\ \ddots & \ddots & \ddots & \ddots & \vdots \\ \dots & \dots & 0 & -J_{N-2} & \omega-(\mu_{N-1}-j\frac{\kappa_{N-1}}{2}-j\frac{\gamma_{N-1}}{2}) \end{pmatrix} \tag{5.16}$$

and vector $|x_{in}\rangle$ as:

$$|x_{in}\rangle = \begin{pmatrix} \sqrt{\gamma_0}x_0 \\ 0 \\ \vdots \\ 0 \end{pmatrix} \tag{5.17}$$

This allows us to compress Eq. 5.14 into

$$j(\omega\mathbb{I} - H_{eff})\,|a_n\rangle = |x_{in}\rangle \tag{5.18}$$

Hence, we obtain $|a_n\rangle$ as

$$|a_n\rangle = -j(\omega\mathbb{I} - H_{eff})^{-1}\,|x_{in}\rangle \tag{5.19}$$

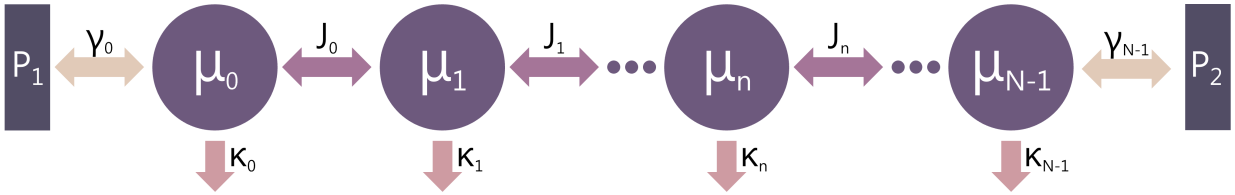

Figure 5.4: Schematic depicting a general CCA device. Each resonator site is characterized by the onsite potential μ_n and the loss rate to the environment/absorption is denoted by κ_n. The hopping rates between the sites are denoted by J_n. The array is probed using grating couplers coupled to the first and last sites of the array with coupling rates denoted by γ_n. The grating couplers are themselves denoted by the ports P_1, P_2.

From input-output formalism we can also write the output modes as:

$$|y_{out}\rangle = |x_{in}\rangle + |\sqrt{\gamma_n} a_n\rangle \tag{5.20}$$

Separately, we know that the two experimentally measurable quantities from the device the reflection spectrum $|R(\omega)|^2$ and the transmission spectrum $|T(\omega)|^2$ of the system can be written as

$$|R(\omega)|^2 = \left|\frac{y_0}{x_0}\right|^2, |T(\omega)|^2 = \left|\frac{y_{N-1}}{x_0}\right|^2 \tag{5.21}$$

Substituting for y_0 from Eqs. 5.19, 5.20 we can obtain $|R(\omega)|^2$ as

$$\begin{aligned} |R(\omega)|^2 = \left|\frac{y_0}{x_0}\right|^2 &= \left|\frac{x_0 - j\gamma_0 x_0 \langle v_0| (\omega\mathbb{I} - H_{eff})^{-1} |v_0\rangle}{x_0}\right|^2 \\ &= \left|1 - j\gamma_0 \langle v_0| (\omega\mathbb{I} - H_{eff})^{-1} |v_0\rangle\right|^2 \end{aligned} \tag{5.22}$$

where $|v_0\rangle = \begin{pmatrix} 1 \\ 0 \\ \vdots \\ 0 \end{pmatrix}$.

Let ϵ_α, $|\epsilon_\alpha\rangle$ denote the eigenvalues and eigenvectors of H_{eff}, as H_{eff} is complex symmetric

matrix we can write

$$H_{eff} = \sum_{\alpha} \epsilon_\alpha \left|\epsilon_\alpha\right\rangle \left\langle\epsilon_\alpha\right| \tag{5.23}$$

Note that $\langle\epsilon_\alpha|$ denotes the transpose and not the conjugate transpose of $|\epsilon_\alpha\rangle$ and $\langle\epsilon_\beta|\epsilon_\alpha\rangle = \delta_{\beta\alpha}$.This also implies that we can expand $(\omega\mathbb{I} - H_{eff})^{-1}$ as:

$$\frac{1}{\omega\mathbb{I} - H_{eff}} = \sum_{\alpha} \frac{\left|\epsilon_\alpha\right\rangle \left\langle\epsilon_\alpha\right|}{\omega - \epsilon_\alpha} \tag{5.24}$$

then we can write Eq. 5.22

$$|R(\omega)|^2 = \left|1 - j\gamma_0 \sum_{\alpha} \left\langle v_0\right| \frac{\left|\epsilon_\alpha\right\rangle \left\langle\epsilon_\alpha\right|}{\omega - \epsilon_\alpha} \left|v_0\right\rangle\right|^2 = \left|1 - j\gamma_0 \sum_{\alpha} \frac{\left\langle v_0|\epsilon_\alpha\right\rangle^2}{\omega - \epsilon_\alpha}\right|^2 \tag{5.25}$$

Similarly, for transmission spectrum $|T(\omega)|^2$ we have

$$\begin{aligned} |T(\omega)|^2 = \left|\frac{y_{N-1}}{x_0}\right|^2 &= \left|\frac{-j\sqrt{\gamma_0\gamma_{N-1}}x_0 \left\langle v_{N-1}(\omega\mathbb{I} - H_{eff})^{-1}\left|v_0\right\rangle\right|}{x_0}\right|^2 \\ &= \left|-j\sqrt{\gamma_0\gamma_{N-1}} \left\langle v_{N-1}\right| (\omega\mathbb{I} - H_{eff})^{-1} \left|v_0\right\rangle\right|^2 \end{aligned} \tag{5.26}$$

Using Eq. 5.24

$$|T(\omega)|^2 = \left|-j\sqrt{\gamma_0\gamma_{N-1}} \sum_{\alpha} \left\langle v_{N-1}\right| \frac{\left|\epsilon_\alpha\right\rangle \left\langle\epsilon_\alpha\right|}{\omega - \epsilon_\alpha} \left|v_0\right\rangle\right|^2 = \left|-j\sqrt{\gamma_0\gamma_{N-1}} \sum_{\alpha} \frac{\left\langle v_{N-1}|\epsilon_\alpha\right\rangle \left\langle\epsilon_\alpha|v_0\right\rangle}{\omega - \epsilon_\alpha}\right|^2 \tag{5.27}$$

Going further, exploiting the geometry of the device allows us to write

$$H_{eff} \left|v_n\right\rangle = \tilde{\mu}_n \left|v_n\right\rangle + J_{n-1} \left|v_{n-1}\right\rangle + J_n \left|v_{n+1}\right\rangle, \text{ where} \tilde{\mu}_n = \mu_n - j\frac{\kappa_n}{2} - j\frac{\gamma_n}{2}; \tag{5.28}$$

and $\left|v_n\right\rangle = \begin{pmatrix} 0 \\ \vdots \\ 1 \\ \vdots \\ 0 \end{pmatrix}$ n^{th} row.

Taking transpose and multiplying by $|\epsilon_\alpha\rangle$ we get

$$\langle v_n| H_{eff} |\epsilon_\alpha\rangle = \langle v_n| \tilde{\mu}_n |\epsilon_\alpha\rangle + \langle v_{n-1}| J_{n-1} |\epsilon_\alpha\rangle + \langle v_{n+1}| J_n |\epsilon_\alpha\rangle \tag{5.29}$$

$$\implies \langle v_n| \epsilon_\alpha |\epsilon_\alpha\rangle = \langle v_n| \tilde{\mu}_n |\epsilon_\alpha\rangle + \langle v_{n-1}| J_{n-1} |\epsilon_\alpha\rangle + \langle v_{n+1}| J_n |\epsilon_\alpha\rangle \tag{5.30}$$

$$\implies (\epsilon_\alpha - \tilde{\mu}_n) \langle v_n|\epsilon_\alpha\rangle - J_{n-1} \langle v_{n-1}|\epsilon_\alpha\rangle = J_n \langle v_{n+1}|\epsilon_\alpha\rangle \tag{5.31}$$

Also using Eq. 5.23 we have

$$\tilde{\mu}_n = \langle v_n| H_{eff} |v_n\rangle = \sum_\alpha \epsilon_\alpha \langle v_n|\epsilon_\alpha\rangle^2 \tag{5.32}$$

Now we have all the ingredient equations needed for determining H_{eff}. The general method we use for Hamiltonian tomography can be summarized as an algorithm **SA1**:

(i) Measure reflection spectrum $|R(\omega)|^2$ of the device and fit it to a sum N complex Lorentzian functions to obtain all the ϵ_α's and $\langle v_0|\epsilon_\alpha\rangle$'s using Eq. 5.25.

(ii) For the first site ($n = 0$), obtain the diagonal element $\tilde{\mu}_n$ of H_{eff} using Eq. 5.32.

(iii) Normalize Eq. 5.31 to then obtain the off-diagonal element J_n.

(iv) Use the value of J_n to obtain all the $\langle v_{n+1}|\epsilon_\alpha\rangle$s needed for the next iteration.

(v) Repeat steps $3, 4, 5$ for $n > 0$ until the entire H_{eff} has been determined.

We next demonstrate how the algorithm SA1 looks in practice:
(i) We begin with fitting the experimentally measured reflection spectrum $|R(\omega)|^2$ as sum of N Lorentzians to obtain the values of γ_0,$\langle v_0|\epsilon_\alpha\rangle$,$\epsilon_\alpha$ as

$$|R(\omega)|^2 = \left|1 - j\sum_\alpha \frac{A_\alpha e^{j\phi_\alpha}}{\omega - (\omega_\alpha - j\beta_\alpha)}\right|^2, \text{where } \epsilon_\alpha = \omega_\alpha - j\beta_\alpha, \gamma_0 \langle v_0|\epsilon_\alpha\rangle^2 = A_\alpha e^{j\phi_\alpha} \tag{5.33}$$

From normalization it also follows that $\sum_\alpha \langle v_0|\epsilon_\alpha\rangle^2 = 1 \implies \sum_\alpha A_\alpha e^{j\phi_\alpha} = \gamma_0$. Here, fitting for the complex Lorentzians from the reflection spectrum $|R(\omega)|^2$ is done by minimizing

the following expression to ensure that the finally fitted H_{eff} falls in the realm of physical possibility:

$$\text{Min}\left\{\left\||R(\omega)|^2_{predicted}-|R(\omega)|^2_{measured}\right\|^2+\left|\text{Im}\left(\sum_\alpha A_\alpha e^{j\phi_\alpha}\right)\right|+\sum_i|\text{Im}(J_i)|\right\} \tag{5.34}$$

(ii) For the first site ($n=0$) we use Eq. 5.32 to obtain the diagonal element $\tilde{\mu}_0$ as

$$\tilde{\mu}_0=\sum_\alpha \epsilon_\alpha\left\langle v_0|\epsilon_\alpha\right\rangle^2=\sum_\alpha(\omega_\alpha-j\beta_\alpha)A_\alpha e^{j\phi_\alpha}/\gamma_0 \tag{5.35}$$

(iii) Next we determine the first off-diagonal element J_0 using Eq. 5.31 ($(\epsilon_\alpha-\tilde{\mu}_0)\left\langle v_0|\epsilon_\alpha\right\rangle = J_0\left\langle v_1|\epsilon_\alpha\right\rangle$) for $n=0$ and normalizing for $\sum_\alpha\left\langle v_1|\epsilon_\alpha\right\rangle^2=1$, giving:

$$J_0=\sqrt{\sum_\alpha((\epsilon_\alpha-\tilde{\mu}_0)\left\langle v_0|\epsilon_\alpha\right\rangle)^2}=\sqrt{\sum_\alpha(\omega_\alpha-j\beta_\alpha\tilde{\mu}_0)^2A_\alpha e^{j\phi_\alpha}/\gamma_0} \tag{5.36}$$

(iv) Finally, we can substitute the obtained J_0 back into Eq. 5.31 to obtain $\langle v_1|\epsilon_\alpha\rangle$s needed for the next iteration as:

$$\left\langle v_1|\epsilon_\alpha\right\rangle=\frac{(\epsilon_\alpha-\tilde{\mu}_0)\left\langle v_0|\epsilon_\alpha\right\rangle}{J_0}=\frac{(\omega_\alpha-j\beta_\alpha-\tilde{\mu}_0)\sqrt{A_\alpha e^{j\phi_\alpha}}}{J_0} \tag{5.37}$$

(v) Next for $n=1$, carrying out steps (ii)-(iv) gives:

$$\tilde{\mu}_1=\sum_\alpha\epsilon_\alpha\left\langle v_1|\epsilon_\alpha\right\rangle^2,\ (\epsilon_\alpha-\tilde{\mu}_1)\left\langle v_1|\epsilon_\alpha\right\rangle-J_0\left\langle v_0|\epsilon_\alpha\right\rangle=J_1\left\langle v_2|\epsilon_\alpha\right\rangle \tag{5.38}$$

then normalizing for $\sum_\alpha\left\langle v_2|\epsilon_\alpha\right\rangle^2=1$ gives

$$\begin{aligned}J_1&=\sqrt{\sum_\alpha((\epsilon_\alpha-\tilde{\mu}_1)\left\langle v_1|\epsilon_\alpha\right\rangle-J_0\left\langle v_0|\epsilon_\alpha\right\rangle)^2},\\ \left\langle v_2|\epsilon_\alpha\right\rangle&=\frac{(\epsilon_\alpha-\tilde{\mu}_1)\left\langle v_1|\epsilon_\alpha\right\rangle-J_0\left\langle v_0|\epsilon_\alpha\right\rangle}{J_1}\end{aligned} \tag{5.39}$$

And so on for $n>1$ we can keep iterating over the steps (ii)-(iv) until we obtain all the $\tilde{\mu}_n$, J_n where $n\in[0,\dots N-1]$. At the end of the algorithm we will have a successfully mapped effective Hamiltonian H_{eff} describing the device. A couple of things to note in the algorithm are: (i) We assume that all J_n have the same sign, and that it is a valid

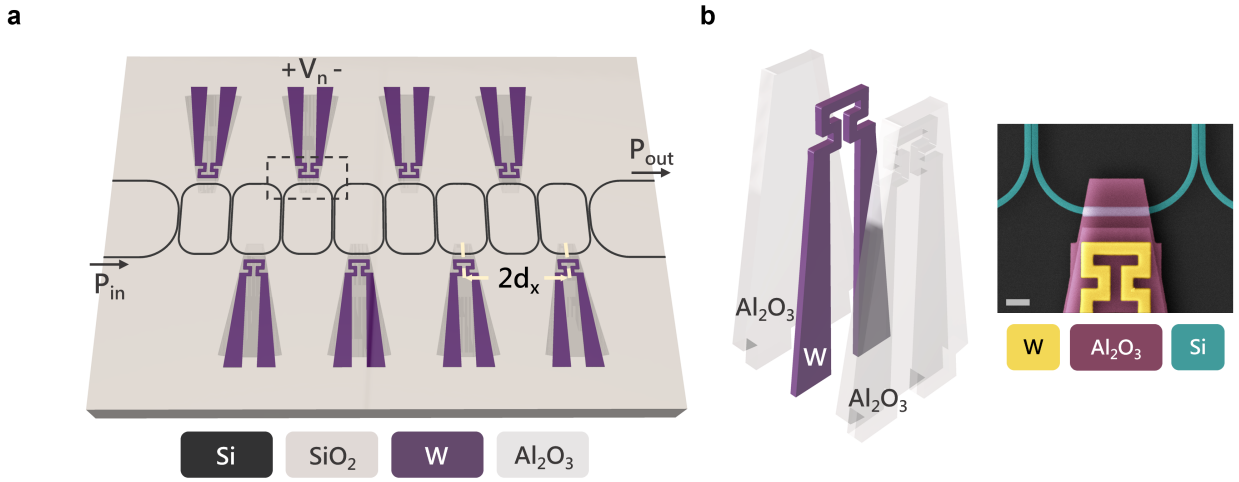

Figure 5.5: Heater design. (a) Device schematic depicting the electrical characterization as voltage V_n is applied to the n^{th} site while measuring the transmission spectrum ($d_x = 14.66\mu m$).(b) Exploded view of the TO island heaters. The heater consists of a tungsten element sandwiched between alumina layers. Inset shows a false colored SEM image (scale bar: $2\mu m$) of a typical TO island (yellow: tungsten, pink: alumina, teal: silicon).

assumption for our devices. (ii) The algorithm SA1 works for determining H_{eff} when we fit the measured reflection spectrum $|R(\omega)|^2$ to a sum of complex Lorentzian functions to obtain the eigenvalues ϵ_α and spectral weights $\langle v_0|\epsilon_\alpha\rangle$. While we can also fit the transmission spectrum $|T(\omega)|^2$ to a sum of complex Lorentzian functions to obtain the eigenvalues ϵ_αs, as evident from Eq. 5.27 we cannot uniquely determine the involved spectral weights $\langle v_0|\epsilon_\alpha\rangle$, $\langle v_{N-1}|\epsilon_\alpha\rangle$ from such a fit.

5.4 Thermal layer design & characterization

Thermal control of the CCA has two primary design objectives: (i) minimizing the additional optical loss incurred when introducing the heaters and (ii) reducing the thermal crosstalk between heaters, which need to be placed in close proximity owing to the small device footprint necessary to obtain small mode volumes for each cavity and ensure strong coupling between

the cavities while maintaining large free spectral ranges [15,24]. We meet both objectives by engineering TO island heaters made up of tungsten (W) wires sandwiched between two alumina (Al_2O_3) layers (Fig. 5.5a, b). In such a configuration, the lower thermal resistance of the alumina layers than that of the air/silicon oxide channel separating the islands allows for a more directional transfer of thermal energy from the tungsten heaters to the corresponding resonators. Since alumina is typically optically lossless in the telecommunication wavelength range, the islands also allow for placing the tungsten heaters at an adequate distance from the racetrack resonators. This ensures that the introduction of heating elements occurs with minimal absorptive losses and allows for achieving much higher Q-factors required for addressability of individual eigenmodes of a controllable CCA platform. Additionally, the top alumina layer acts as a protective layer against oxidation for the tungsten heating element [67]. In comparison, typical TO control schemes either rely on placing heaters on top of a universal cladding [68] for minimizing additional dissipative losses or incorporating these into the resonator structure itself using photoconductive elements [69] for extremely local control. However, both of these approaches have major drawbacks. The former allows to obtain very high Q-factors, it suffers from poor local controllability, with our island heaters outperforming these by more than 50% in reducing stray effects of thermal crosstalk. On the other hand, while the latter approach gives extremely local control, the photoconductive elements used to do so inevitably limit the maximum achievable Q-factors due to dopant implantation in the regions that host the optical mode.

5.4.1 Thermal simulations

In this subsection, we discuss the thermal simulations used to design the island heaters. For a racetrack resonator we know that $n_{eff}l = m\mu_n^{\lambda}$, where n_{eff} is the refractive index of the racetrack resonator, l is the length of the resonator, μ_n^{λ} is the onsite potential (in wavelength units) and $m \in \mathbb{Z}$. Let a segment of length x be affected by change in temperature, such that

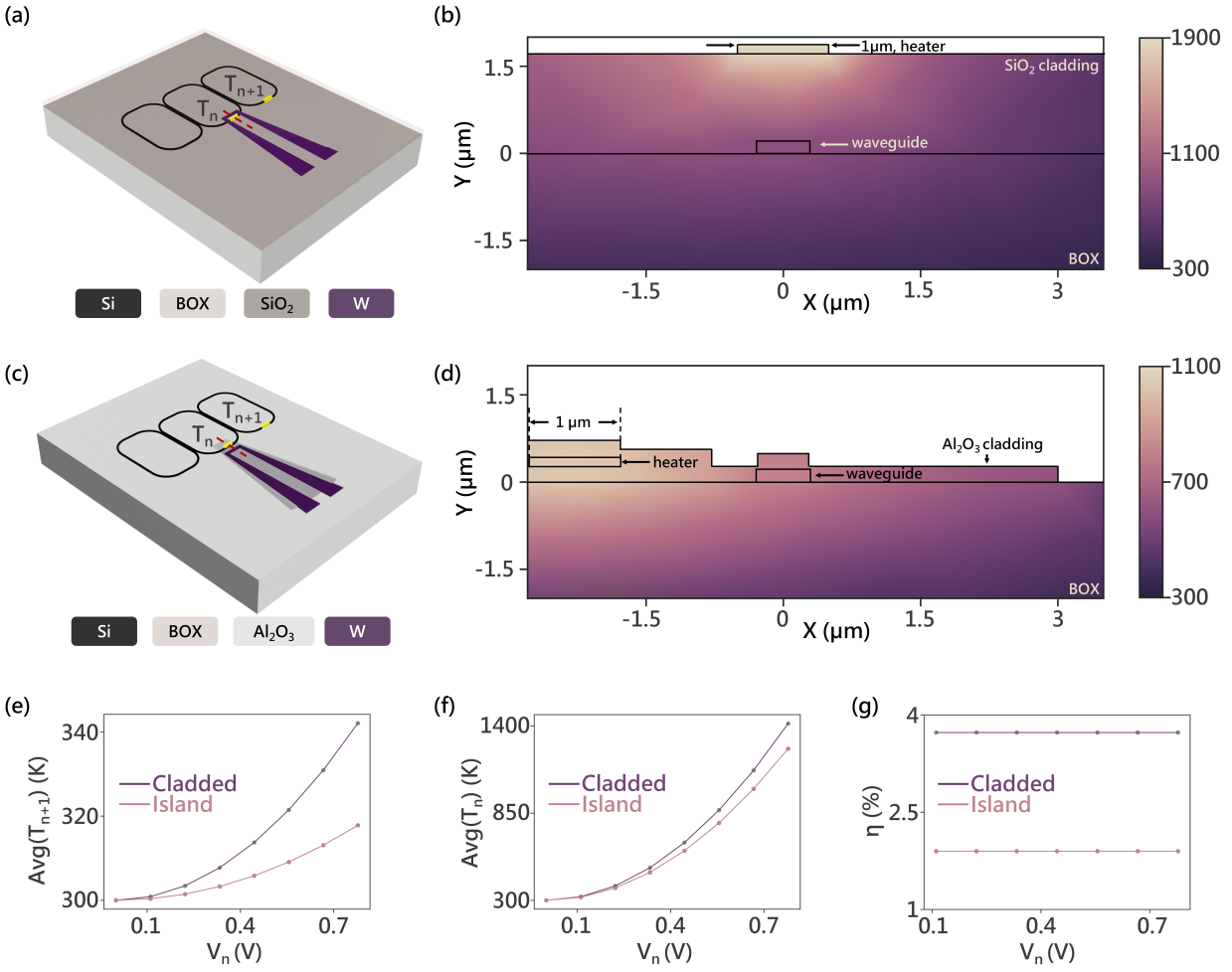

Figure 5.6: Thermal simulation results. (a) Schematic depicting the device with conventional TO heater sitting directly over the resonator separated by $1.5\mu m$ thick oxide cladding (label: Cladded). (b) Temperature profile (in K) across the cladded waveguide (cross-section denoted by red dashed line in the schematic) when $V_n = 0.56\ V$. (c) Schematic depicting a device equipped with the island TO heater used in our paper (label: Island). (d) Temperature profile (in K) across the island waveguide (cross-section denoted by red dashed line in the schematic) when $V_n = 0.56\ V$. (e) Plot comparing average temperature across the straight segment (in yellow) of the $(n+1)^{th}$ resonator. (f) Plot comparing average temperature across the straight segment (in yellow) of the n^{th} resonator. (g) Plot comparing η factor in % for the two device designs. (purple: cladded, pink: island).

its refractive index is given by $n(x)$. Resonance condition for the resonator then becomes:

$$n_{eff}(l-x) + \int n(x)dx = m(\mu_n^\lambda + \Delta\mu_n^\lambda) \tag{5.40}$$

Removing the constant terms gives

$$\int (n(x) - n_{eff})dx = \int \Delta n(x)dx = m(\Delta\mu_n^\lambda) \tag{5.41}$$

Assuming a constant thermo-optic coefficient $\frac{\mathrm{d}n}{\mathrm{d}T}$ we can write $\Delta n(x) = \rho\Delta T(x)$. Consequently,

$$\int \rho\Delta T(x)dx = m(\Delta\mu_n^\lambda) \tag{5.42}$$

This implies that shift in onsite potential $\Delta\mu_n^\lambda \propto \int \Delta T(x)dx$. To estimate this effect of thermal crosstalk in our system and compare it with typically used thermo-optic (TO) heaters we perform a set of thermal simulations using ANSYS Lumerical HEAT (Fig. 5.6). In Fig. 5.6(a) we have the schematic depicting a conventional TO heater, where the metallic heating element sits directly on top of the resonator segment separated by a uniform and universal 1.5 μm SiO_2 cladding. In Fig. 5.6(c) we have the island TO heater design we used for our device. For both these cases we have the CCA made up of only 3 sites with the heater placed on the middle site (n^{th}). We then record the temperature profile in the shorter straight segment (highlighted in yellow) of the racetrack resonators for the n^{th} and $((n+1)^{th}$ sites as we vary the voltage applied V_n across the heater from 0 V to 0.78 V. Then in Fig. 5.6(b), (d) we plot the temperature profile (in K) across the waveguide cross-section (denoted by the red dashed line in the corresponding schematic) for both the designs when 0.56 V is applied across the heater. In Fig. 5.6(e) we plot the average temperature across the segments given by

$$Avg(T) = \frac{\int T(x)dx}{\int dx} \tag{5.43}$$

for neighboring $(n+1)^{th}$ site. Similarly, in Fig. 5.6(f) we plot the average temperature across the segment for n^{th} site. It is clear from these plots that even though both heater

designs cause a similar increase in the onsite temperature (n^{th}), the average temperature in the neighboring sites diverges rapidly between the designs with the temperature difference already greater than 24 K at 0.78 V. To study the difference in effects of this thermal crosstalk we then define a dimensionless parameter η given by

$$\eta = \frac{\Delta\mu^{\lambda}_{n+1}}{\Delta\mu^{\lambda}_{n}} \tag{5.44}$$

Using Eq. 5.42 we can write the above as

$$\eta = \frac{\Delta\mu^{\lambda}_{n+1}}{\Delta\mu^{\lambda}_{n}} = \frac{\int \Delta T_{n+1}(x)dx}{\int \Delta T_{n}(x)dx} = \frac{\int (T_{n+1}(x) - 300)dx}{\int (T_{n}(x) - 300)dx} \tag{5.45}$$

5.4.2 Characterization

We characterize the realized CCA by applying a linearly increasing voltage across each heater one at a time and recording the respective transmission spectra. The eigenenergies are then extracted from the recorded spectra and combined with our knowledge of H^{0}_{eff}, we estimate the amount of crosstalk between the heaters. The change in the onsite potential $\Delta\mu_n$ when expressed in wavelength units is proportional to the square of voltage V_n applied to the n^{th} site: $\Delta\mu^{\lambda}_{n} \propto V^{2}_{n}$. Note that, we express the onsite potentials μ_n and eigenvalues ϵ_n of the CCA in wavelength units as μ^{λ}_{n} and ϵ^{λ}_{n}. We plot the effects of voltage V_n applied across heater h_n on the potential profile $[\mu^{\lambda}_{n}]$ of the CCA in Fig. 5.7. The change in respective onsite potentials $\Delta\mu^{\lambda}_{n}$ is represented by the radii of the circles, whereas the color of the circles denotes the voltage V_n applied across heater h_n. From the plot, we establish that thermal crosstalk is already low between the nearest neighbors ($n \pm 1$) and becomes negligible as we go beyond the third-nearest neighbors ($n \pm 3$). In order to obtain this plot we do a fitting procedure described in the following paragraph.

Let voltage V_n be applied to heater h_n at the n^{th} site of the CCA. When only one heater h_n is turned on at a time, using Ohmic heating law we can approximate the change in temperature at n^{th} site of the CCA as $Avg(\Delta T_n) \propto V^{2}_{n}/R_n$ where R_n is the resistance of heater h_n. For a constant thermo-optic coefficient $\frac{\mathrm{d}n}{\mathrm{d}T}$, from Eq. 5.42 we know that $\Delta\mu^{\lambda}_{n} \propto Avg(\Delta T_n)$.

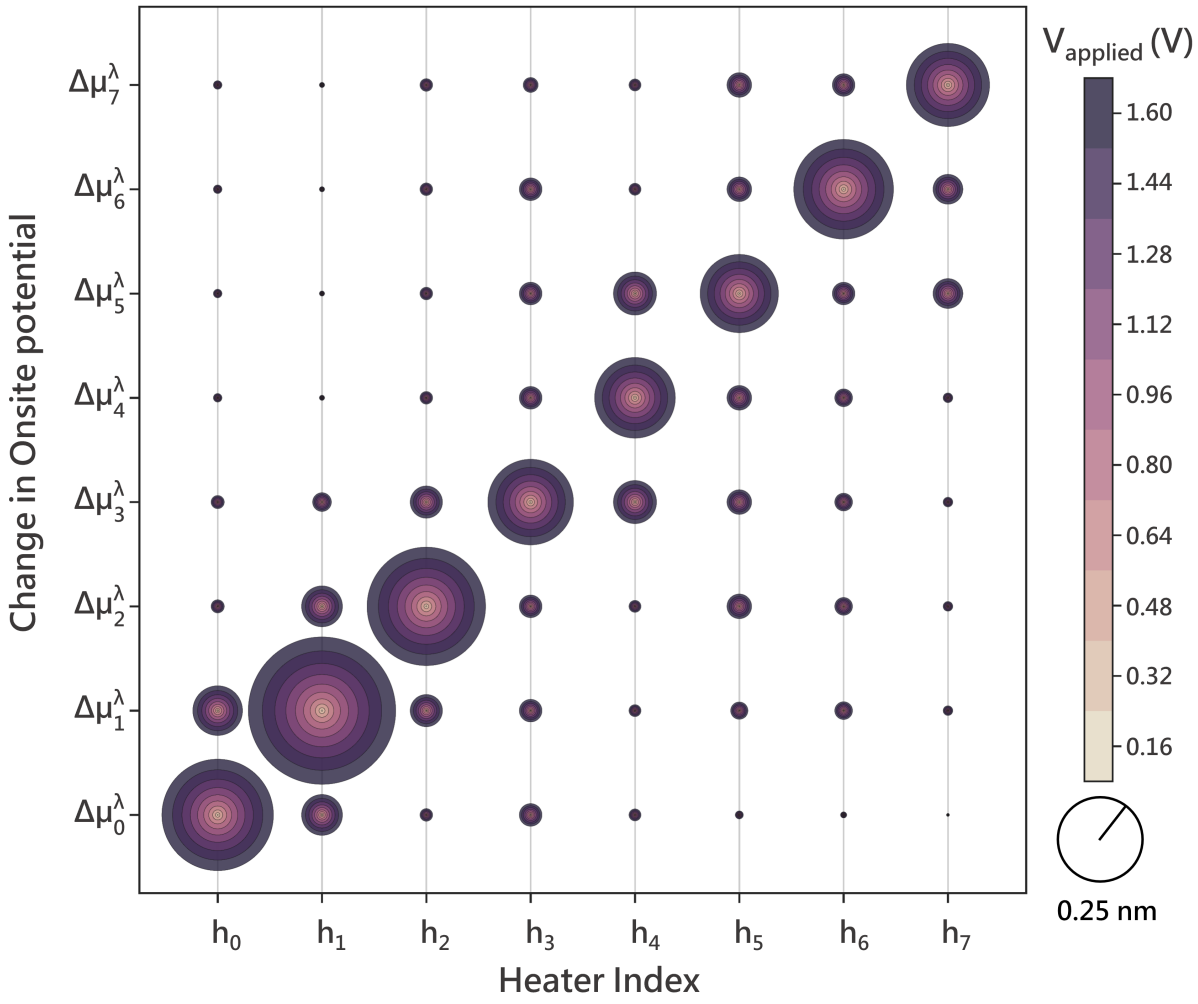

Figure 5.7: Electrical Characterization. Plot showing the effect of heaters $[h_n]$ on the potential profile across the device. The x-axis denotes the heater index h_n switched ON for a particular set of measurements and the y-axis represents the change in potential profile $[\Delta\mu_n^\lambda]$. The voltage applied for the measurement (V_n) across heater h_n is mapped to the color of the circular surface and the corresponding change in potential is denoted by the radii of the circle encompassing the surface (0.25 nm of change is depicted by the radii of the circle in the scale bar).

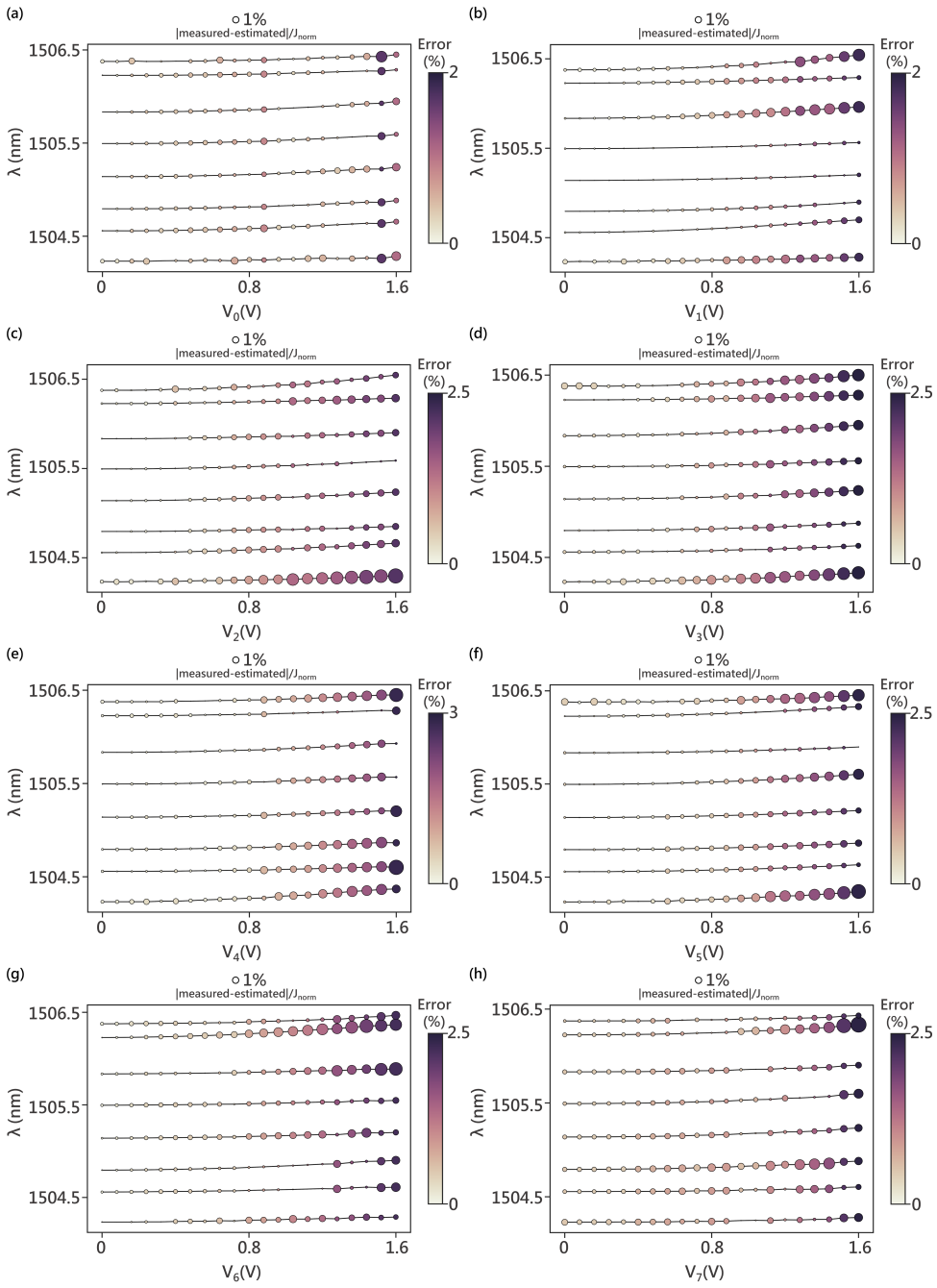

Figure 5.8: Thermal crosstalk extraction. Fitting accuracy for sweeps with only one heater turned on at a time, where the x-axis denotes the voltage applied V_n, the y-axis denotes the wavelength with the location of the measured eigenenergies is denoted by the dark black lines in the background. The radii of the circles denote the deviation of the fitted value from measured values (scale bar on top). The color of the dots denotes the overall prediction error for that generation.

Combining the above two relations using a proportionality constant k_1 allows us to write:

$$\Delta\mu_n^\lambda = k_1 V_n^2/R_n = \alpha_n V_n^2 \tag{5.46}$$

where $\alpha_n = k_1/R_n$. Since only h_n is turned on, it also follows that for another site m in the array, $\Delta\mu_m^\lambda \propto Avg(\Delta T_n)$. Introducing another set of proportionality constants β_{nm} allows us to write:

$$\Delta\mu_m^\lambda = \beta_{nm}\alpha_n V_n^2 = \beta'_{nm} V_n^2 \tag{5.47}$$

Using Eq. 5.46, 5.47 we can then estimate the thermal crosstalk by fitting for these coefficients α_n, β'_{nm} by calculating the change in onsite potentials and estimating the eigenenergies of the modified H_{eff} whose initial state H^0_{eff} was fitted with the procedure outlined in the previous subsection.

$$[\epsilon_n^\lambda]_{estimated} = \text{Eig}(H^0_{eff} + [\Delta\mu_n]\mathbb{I}),\ [\Delta\mu_n^\lambda] = [\alpha_n, \beta'_{nm}][V_n^2] \tag{5.48}$$

We do this fitting for all the eight heaters $[h_n]$ to obtain corresponding α_ns and β'_{nm}s; accuracy results of which are plotted in Fig. 5.8. The x-axis denotes the voltage V_n applied to heater h_n, the y-axis plots the eigenenergies as wavelengths. The black lines in the background denote the measured locations of eigenenergies on application of V_n, the size of the circle denotes the error of the fit from the measured location of eigenenergy. The color of the circles denotes the overall fit error for that particular measurement. The extracted values α_ns and β'_{nm} are then used to plot Fig. 5.7 where we use these to plot the change in $\Delta\mu_n^\lambda$s for all V_ns used in the measurements shown in Fig. 5.8.

5.5 Control model

We next model the CCA to accurately predict the eigenenergies of the system on application of a voltage profile $[V_n] = [V_0, V_1, \ldots V_{N-1}]$ across the heaters. Here, we define a translationally invariant function f which takes in the input voltage profile and predicts the change in onsite potential when applied at each site. The function f consists of three sets of terms: (i)

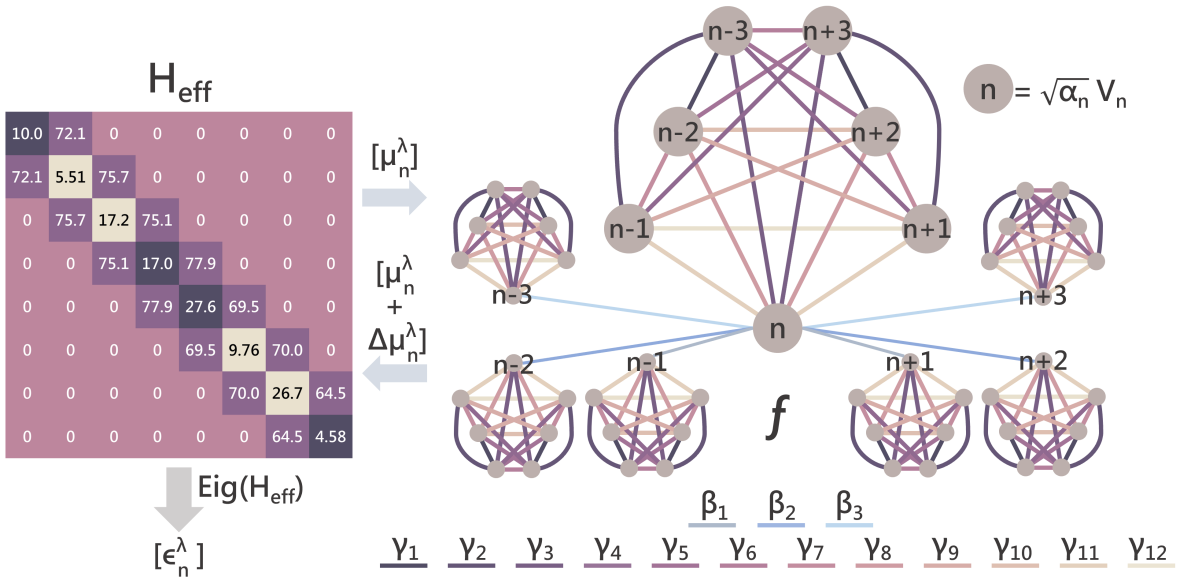

Figure 5.9: Electrical control model schematic. Visualization of the optimization process depicting how the model takes in the system Hamiltonian H_{eff} and fits for the function f which connects the applied voltage profile $[V_n]$ to change in onsite potentials. We predict the position of eigenenergies on application of $[V_n]$ by calculating the change in onsite potentials which lie along the Hamiltonian diagonal and finding the eigenvalues of the modified Hamiltonian. The optimization is initialized using H^0_{eff} shown in the matrix form (only real part is depicted). All entries are in GHz, with diagonal terms denoting the deviations in resonant frequency about the mean (dark purple: $+ve$ deviation, tan: $-ve$ deviation) and super/sub diagonal terms denoting the hopping rates. $n \pm i$ denote indices of sites in neighborhood of site n on which the function f is being applied on. The coefficients β_i are denoted in hues of blue and $\gamma_{j,k}$ are denoted in hues of purple

a fitting correction to the initial onsite potential denoted by δ_n, (ii) thermal contributions from voltages applied across heaters in the thermal neighborhood of site $n(n \pm 3)$ connected through proportionality coefficients β_i's (V_i^2), (iii) cross-terms connected through proportionality coefficients $\gamma_{j,k}$'s (V_jV_k s.t. $i, j, k \in [n-3, n+3]$) accounting for the thermal effects

on heater performances by virtue of these being in the thermal vicinity of each other. We also use an additional set of coefficients α_n to incorporate the effects of minor variations in heater resistances due to fabrication inconsistencies. We then express this relationship mathematically as

$$\Delta\mu_n^\lambda = f([V_n]) = \delta_n + \sum_i \beta_i(\alpha_i V_i^2) + \sum_{j,k} \gamma_{j,k}(\sqrt{\alpha_j \alpha_k} V_j V_k) \tag{5.49}$$

Note that, we assume that f is translationally invariant, and hence the number of functional parameters β_i and $\gamma_{j,k}$ needed to model the device behavior can be restricted to 3 and 12 respectively.

We visualize this process in Fig. 5.9 where we show how we can use the model to predict the location of eigenenergies $[\epsilon_n^\lambda]$ by finding the eigenvalues of the modified Hamiltonian. Starting with the initial H_{eff}^0 and updating its diagonal terms by evaluating the function f at each site of the array for a particular $[V_n]$ we predict the eigenvalues of the modified Hamiltonian as:

$$[\epsilon_n^\lambda]_{predicted} = \text{Eig}(H_{eff}^0 + [\Delta\mu_n]\mathbb{I}) \tag{5.50}$$

These predicted eigenenergies are then used to fit for f by minimizing the error obtained by calculating the deviations from experimentally extracted eigenenergies across many measurements (here we limit the number of measurements to 288).

$$\text{Error} = \frac{|[\epsilon_n^\lambda]_{predicted} - [\epsilon_n^\lambda]_{measured}|^2}{J_{norm}} \tag{5.51}$$

The probability distribution of the fitting error normalized to the mean hopping-rate J_{norm} is plotted in Fig. 5.10a. Finally, once we have identified f, we use it to predict the location of eigenenergies for 20 randomly generated voltage profiles in Fig. 5.10b. The centers of the circles in the figure denote the measured values of eigenenergies, and the error in predicted values are represented by the radii of the corresponding circle. The net overall error for a random generation is mapped to the color of the particular set of eigenenergies. From the plot, we can see that the model allows for the prediction of the eigenenergies of our system with greater than 96% accuracy.

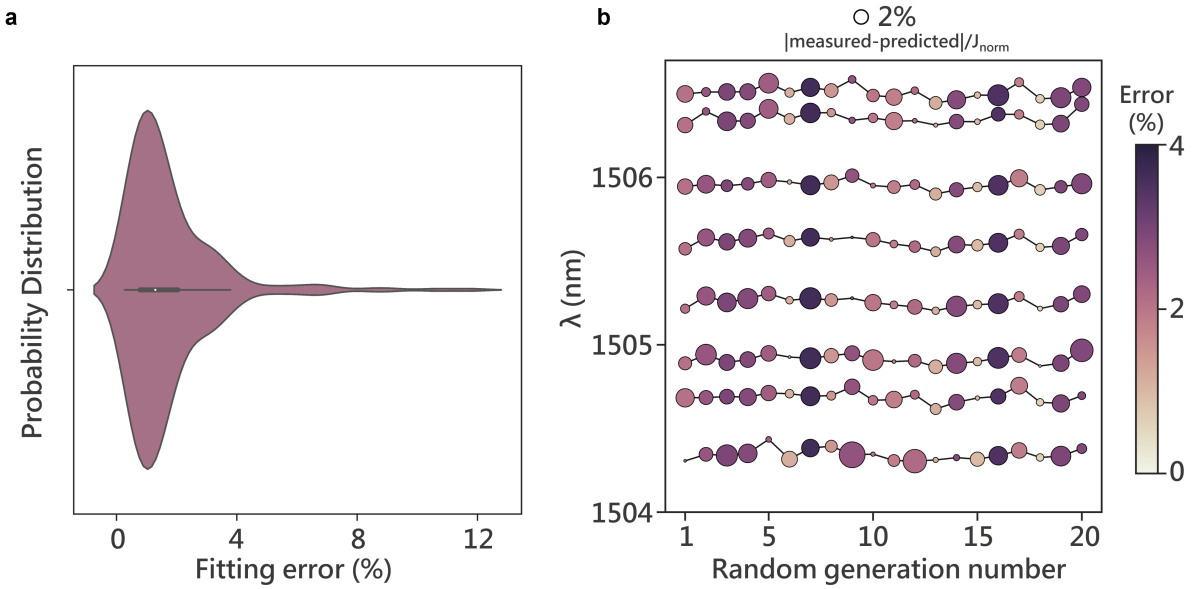

Figure 5.10: Eigenenergy prediction. (a) Violin plot denoting the fitting error normalized to the mean hopping rate J_{norm} across 288 points. (b) Prediction accuracy plot where the x-axis denotes the random generation, and the y-axis denotes the wavelength. The location of the measured eigenenergies is denoted by the dark black lines in background. The radii of the circles denote the deviation of the predicted value from measured values (scale on top). The color of the dots denotes the overall prediction error for that generation.

5.6 Conclusion

In this chapter, we demonstrated a thermally controlled optical CCA which can be used to realize a set of tight binding Hamiltonians with addressability to the entire quantized eigenenergy spectrum. To ensure a compact device footprint and high Q cavities necessary for reaching the regime of interacting photons and allowing access to the full quantized eigenspectrum [29], we engineered special TO islands heaters, which allowed reduction in thermal crosstalk by almost 50% over previously reported works [68,70]. Our device design allowed us to realize Q-factors more than 7.1×10^4 for heater integrated racetrack resonators. Finally, we

presented a mathematical model which allowed for precise control of the eigenenergies of the implemented Hamiltonians within an error of only 4% of the mean hopping rate. Our device can already be used to simulate a number of single-particle physical effects like Anderson localization [12] and the Su–Schrieffer–Heeger model [35]. One potential disadvantage of using TO heaters is that our dynamic modulation rates are limited to the MHz regime [68] which rules out the possibility to implement models like the Haldane quantum Hall effect [71] requiring modulation of onsite potentials at rates comparable to the mean hopping rate ($\approx \ GHz$). However, what TO heaters might lack, they make up for it by allowing a larger range of static modulation and ease of scalability in comparison to say electro-optical modulators which might be much faster but present far more challenges when it comes to scaling to a larger number of sites [72]. Looking ahead, our TO island heaters equipped CCAs are hence perfectly suited for implementing a large class of Hamiltonians that do not require very high-speed modulation, such as the Hofstadter Hamiltonian [8, 31], SSH Hamiltonian [15, 35] and non-Hermitian topological Hamiltonians [73], among others. Further, leveraging the immense scaling potential of photonics, operating in a linear regime the CCA can be scaled to sizes where it can be used to study classical and quantum bosonic walks and solid-state lattice band structures [74]. While we did not demonstrate any non-linearity, our CCA with high Q-factors and a cladding free design has the potential to enable integration with excitonic materials [75], defect centers [76, 77] and reach single photon non-linear regime [78–80]. Additionally, adopting more complex control algorithms involving feedback control [81, 82] and data-based learning [83] in future works can help to improve the accuracy of the realized Hamiltonians further. In conclusion, our work shows the scalability, programmability, and measurability of photonic CCAs for the first time, and is a significant step forward over state-of-the art photonic quantum simulators, which are traditionally not programmable or tomographically mappable.

5.7 Extended discussion

5.7.1 Fabrication methods

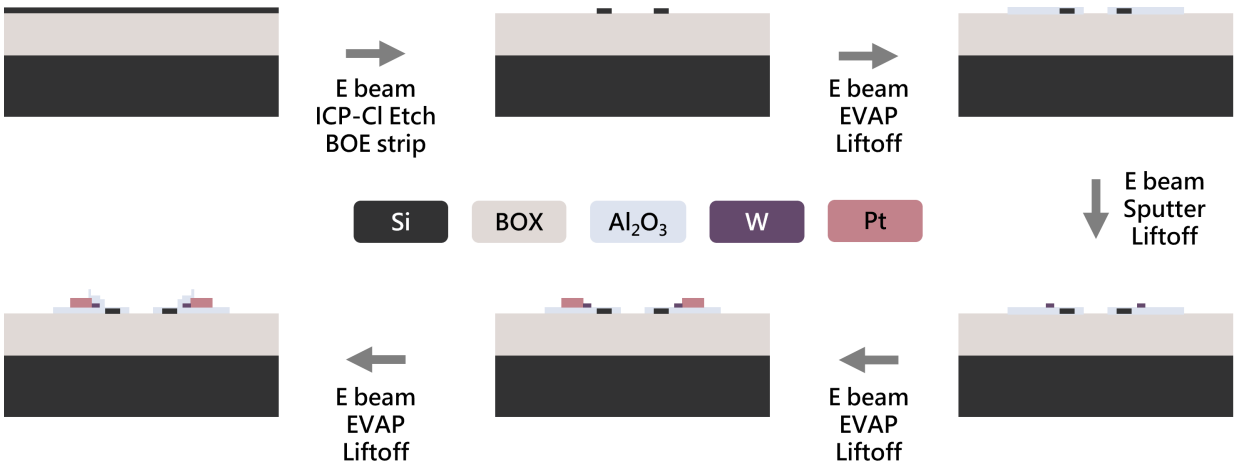

Figure 5.11: Fabrication flow. The CCA was defined on a silicon on insulator (SOI) chip via electron-beam lithography using HSQ resist. Cl_2 gas was then used to etch the structures. The resist was then removed using dilute BOE. For the deposition steps positive tone PMMA resist was used for patterning. Bottom Al_2O_3 layer is 265 nm thick and the sputtered tungsten (W) layer making up the heating elements is 150 nm thick. The contact pads are made up of 25 nm Ti / 325 nm Pt layers. The final Al_2O_3 cladding over the islands is 300 nm thick.

A silicon on insulator wafer (SOITEC) with 220 nm thick film of silicon on 3 μm thick buried silicon oxide was diced. A 10 $mm \times 10$ mm chip thus obtained was used for further processing. After cleaning, the chip was spin-coated with Hydrogen silsesquioxane (HSQ) and exposed using a JEOL JBX6300FS electron beam (e-beam) lithography system. After developing in 25% TMAH, the chip was etched using an inductively coupled plasma etcher with a Cl_2 chemistry. The resist was then removed using diluted BOE. The chip then underwent several cycles of patterning, followed by electron beam evaporation/sputtering of materials

and lift-off to define the island heaters, and contact pads. The first of these cycles involved defining the island pattern in positive tone polymethyl methacrylate (PMMA) resist using e-beam lithography, followed by depositing 265 nm thick Al_2O_3 layer using evaporation and finally lift-off to obtain the lower layer of the islands. The next cycle began by patterning of heating elements using a similar PMMA based e-beam lithography step. A 150 nm thick tungsten (W) layer was then sputtered, followed by a sonication-based lift-off to obtain the heaters. The contact pads made up of 25 nm Ti / 325 nm Pt layers were then defined using a PMMA based e-beam lithography followed by an evaporation and lift-off cycle. The final 300 nm thick Al_2O_3 cladding over the islands was then obtained using a similar e-beam lithography/evaporation/lift-off process cycle.

5.7.2 Quality factor extraction & considerations

The relevant Q-factors for us here are the Q-factors of the eigenmodes of the system which effect Hamiltonian dynamics and the number of modes we can address for a given hopping rate, and the intrinsic Qs of the cavities which act as a barometer of loss in our system due to integration with island heaters. These can be calculated as follows: In the step (i) of the tomography algorithm we fit each of the supermodes to a complex Lorentzian and hence obtain both their eigenfrequencies and linewidths. The following table (Table 5.1) shows the quality factor of each of the eigenmodes calculated using the relation:

$$Q_\alpha = \frac{\omega_\alpha}{2\beta_\alpha} \tag{5.52}$$

where Q_α denotes the Q-factor of the eigenmode α.

Additionally, after going through the entire tomography algorithm, we know all the complex onsite potentials lying along the diagonal of the reconstructed Hamiltonian H_{eff}. Hence, estimating the intrinsic the Q-factors of the cavities not directly coupled to the grating couplers ($n \neq 1,\ N-1$) is straightforward as their complex potentials can be expressed as

Table 5.1: Q-factors of eigenmodes. Quality factors of the 8 supermodes of the CCA. The average linewidth of the eigenmodes is 7.41 GHz and the average Q-factor is $\text{Avg}(Q_\alpha) \approx 2.8 \times 10^4$.

Q_0	Q_1	Q_2	Q_3	Q_4	Q_5	Q_6	Q_7
32432	32380	28314	21609	20394	23738	31814	31746

($\tilde{\mu}_n = \mu_n - j\kappa_n/2, n \neq 0,\ N-1$). The intrinsic Q-factor can then be calculated as:

$$Q_{intrinsic} = \frac{\text{Re}(\tilde{\mu}_n)}{-2\text{Im}(\tilde{\mu}_n)} \ \forall\ n \neq 0, N-1 \tag{5.53}$$

The following table (Table 5.2) then shows the intrinsic Qs for the realized CCA:

Table 5.2: Q-factors of individual cavities. Intrinsic quality factors of the 6 internal cavities ($n \in [1, 6]$).

Q_1	Q_2	Q_3	Q_4	Q_5	Q_6
49821	28467	32146	32148	31137	711666

Finally, as we also obtained the coupling rate to the grating coupler from the algorithm ($\gamma \approx 11.6\ GHz$), we can use it to estimate the average loss rate in the CCA from the following relation:

$$\text{Avg}(\kappa_n) = 2\left(-\sum_{n=0}^{N-1} Im(\tilde{\mu}_n) - \gamma\right) \tag{5.54}$$

Then the typical intrinsic Q can be estimated as

$$\text{Expected}(Q_{intrinsic}) = \frac{\text{Avg}(\text{Re}(\tilde{\mu}_n))}{\text{Avg}(\kappa_n)} \tag{5.55}$$

which for our device gives $\text{Avg}(\kappa_n) = 4.49\ GHz$, $\text{Expected}(Q_{intrinsic}) \approx 4.43 \times 10^4$. We also fabricated some add-drop filters (single racetrack resonators coupled to grating couplers on

either side) on the same chip and measured their Q-factors before integration of the island heaters. The measured data is presented in the table (Table 5.3) below:

Table 5.3: Q-factors of single racetrack resonators (in add-drop configuration) before the addition of island heaters. Q_L denotes the loaded Q-factor, $Q_{intrinsic}$ denotes the unloaded Q-factor, BW denotes the total bandwidth = loss rate + 2 × coupling rate.

No.	Q_L	$Q_{intrinsic}$	BW (GHz)
1	8324	99920	23.96
2	8701	257775	22.9
3	8949	192177	22.28

The Q-factor of the add-drop filters post integration of the island heaters was found to be similar to the Q-factor reported above for the main device. For example, for the add-drop filter No.3 the Q-factors post integration were: $Q_L = 7073$, $Q_{intrinsic} = 45067$ and $BW = 28.18\ GHz$. The intrinsic Q-factor matches very well with the Expected($Q_{intrinsic}$) calculated from the CCA device.

From our simulations in the above sections and measured data, we expect the major source of loss in our device to be the scattering loss due to mode mismatch between the cladded and uncladded sections of the racetrack resonator. We also used mode simulations to calculate the worst-case power coupling between the modes (by estimating their overlap) to be 0.99675; which is on the lower side, hence confirming our hypothesis. Additionally, based on our analysis we can perform a back of the hand calculation to estimate the kind of Q-factors we would ultimately desire in order to realize very large-scale systems made up of say 1000 cavities. We know that the energy band of a 1D infinite tight-binding model is confined within $+2J$ to $-2J$ about the central potential [24]. As individual addressability to eigenmodes is desired, the maximum number of cavities that can be present given the average linewidth of the resonator can then be ball parked as $N_{cav} = 4J/\text{Avg}(\kappa_n)$ where we assume small coupling

rates to the input/output ports. We can then invert this equation to get an idea about the Q-factors desired for a CCA consisting of 1000 cavities:

$$\text{Expected}(Q_{desired}) \sim N_{cav}\frac{\mu}{4J} = 1000\frac{199.29}{4 \times 0.072} \approx 6.9 \times 10^5 \tag{5.56}$$

While this is an order of magnitude higher than the current reported Q-factor, in future works we aim to reduce the loss in the constituent cavities by designing better mode matched waveguide sections. We also plan to incorporate Euler bends [84] in our racetrack resonators and further optimize the fabrication processes to improve the Q-factors of our devices.

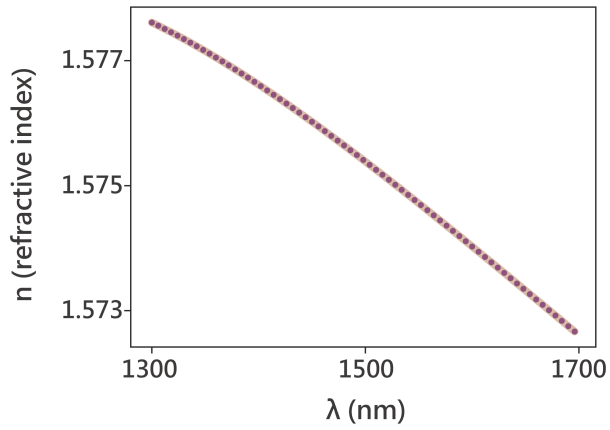

Figure 5.12: Ellipsometry data of evaporated alumina. The refractive index of evaporated alumina is measured using ellipsometry. The imaginary part of the index is negligible, denoting that alumina is lossless in the window of operation of our CCA. $n\,(1505\ nm) = 1.57532$.

Chapter 6

OUTLOOK

In this concluding chapter, we examine some of our efforts in addressing the final challenge in realizing a quantum simulator based on photonic CCAs: optical non-linearity. Realizing on-chip optical non-linearity at the single-photon level is a difficult task due to the extremely weak interactions between two photons. Despite this, the immense potential of having a single photon non-linearity in optics has ensured that the area has attracted a lot of attention from researchers.

As photons typically don't interact except at very high power in bulk nonlinear materials, one of the few ways to reach the quantum non-linear optical (NLO) regime is by utilizing light-matter interaction. While light-matter interaction itself is typically small, it can be enhanced using optical cavities, which allow confinement of light to small volumes for long period of times. In fact, single photon non-linearity has been reported in organic material integrated cavities [80] and atom-cavity systems [85].

However, the scalability requirements of quantum simulators mean that we need to realize strong light-matter interaction on a photonic platform. Solid-state photonic systems based on self-assembled quantum dots have been used to demonstrate photonic blockade and polaritons [86], but because it is very difficult to obtain control over their spectral properties and locations on-chip, these too are not suitable to be used to realize non-linearity on a photonic chip. On the other hand, while exploiting on-chip optical bulk non-linearities would have been an ideal option to be used in a photonic CCA due to their compatibility with the other three requirements for a photonic quantum simulator, the prohibitively large quality factors required [87] mean that the limitations of current fabrication processes makes this route an impractical solution for now. One potential alternative to these is solution-processed colloidal

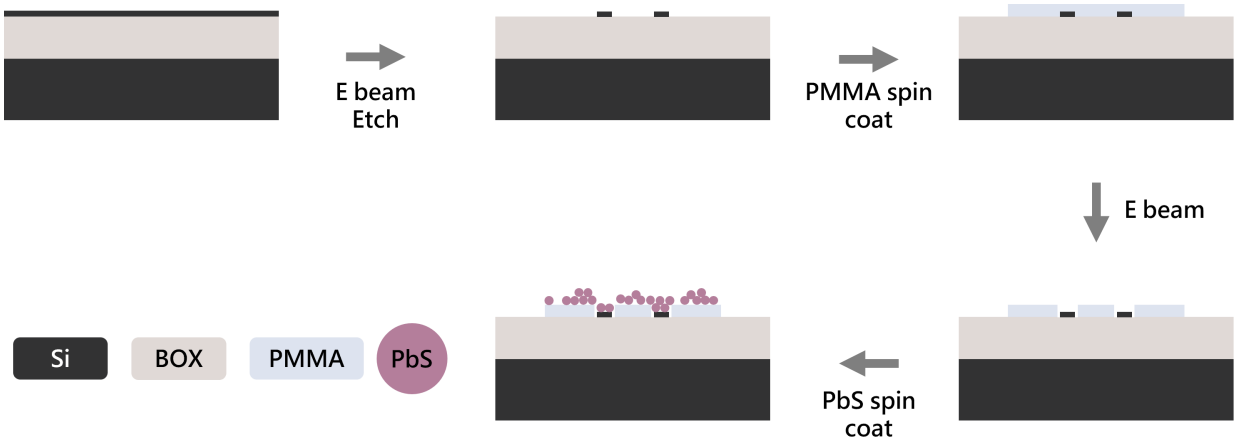

Figure 6.1: Fabrication flow for integrating PbS colloidal QDs with a photonic CCA. We use 220 nm thick Si on 3 μm buried oxide to fabricate the optical layer. The fabrication process remains same as the last chapter up to this point. However, the next steps vary. To integrate the colloidal QDs, we spin coat a 800 nm thick PMMA cladding layer and make windows into it using E-beam lithography. We then spin coat a PbS colloidal QD suspension at 750 rpm for 60 s to deterministically position the dots onto the racetrack resonators.

quantum dots (QD)s due to their low-cost chemical synthesis, straightforward deposition on any substrate, and room temperature stability. These characteristics make them a promising candidate for realizing scalable integrated quantum photonic platforms [88] and in the next section, we briefly talk about the progress we made in integrating these to silicon-photonic chips and the outstanding challenges ahead if this approach is to be employed.

6.1 Colloidal quantum dots

Building on a previous work from our group, which demonstrated the deterministic positioning of colloidal QDs in nanobeam cavities [75], we investigated potential ways to integrate colloidal QDs with our photonic CCAs. The first challenge that we faced was that our photonic CCAs operate in the telecom wavelength regime using silicon photonics to ensure the best pathway forward towards scalability. Therefore, we needed to find alternative colloidal

QDs which emit in a similar spectral regime. Recently, solution-processed lead sulphide (PbS) colloidal QDs were used to demonstrate infrared lasing in telecom window using distributed cavity structures [89]. Building on this work, we investigated if it was possible to integrate similar dots with our racetrack resonators. To accurately position these dots on the racetracks, we modified our fabrication process of the optical layer to integrate QDs. In the updated process, we spin coated a polymethyl methacrylate (PMMA) cladding layer on the chip and used E-beam lithography to define a window over the resonator regions. This allowed us to very precisely control where the colloidal QDs interact with the optical mode of the resonator. The modified fab flow depicted in Fig 6.1.

The fabricated device is depicted in Fig. 6.2 (a). The racetrack resonator used has a bending radius of 5 μm and straight sections that are 10 μm and 3 μm long. The PMMA window size is 30 $\mu m \times 30$ μm and the windows are defined such that PbS dots don't affect the coupling region between the racetrack resonator and the input/output waveguide. Once the device was fabricated, we characterized it by performing photoluminescence (PL) measurements. In Fig. 6.2 (b) we plot the cavity coupled PL spectrum, where we can clearly see the cavity modes over a broad PL background coming from the colloidal QDs. A broadband superluminescent diode (SLED) was used to pump the dots and the PL coming out of the grating couplers was collected with the aid of a pin-hole in a confocal microscopy setup.

Despite this preliminary success, there are some big challenges that lie ahead if these colloidal QDs are to be used to obtain optical non-linearity. These include: (i) while the solution-processed QDs provide ease of scalability to a large number of sites, these suffer from large dephasing rates; (ii) In our experiments, we found that the spectral properties of these dots can vary over short durations of time by changing chemical structures caused due to thermal and optical excitations while pumping. In a previous work, we proposed an experimentally feasible approach to deal with the first of these problems and engineered a system of two cascaded photonic cavities to generate indistinguishable single photons from very dissipative colloidal QDs [79]. The general idea behind the device was as follows: using a device made up of two weakly coupled cavities, only one of which is coupled to a single colloidal QD, we

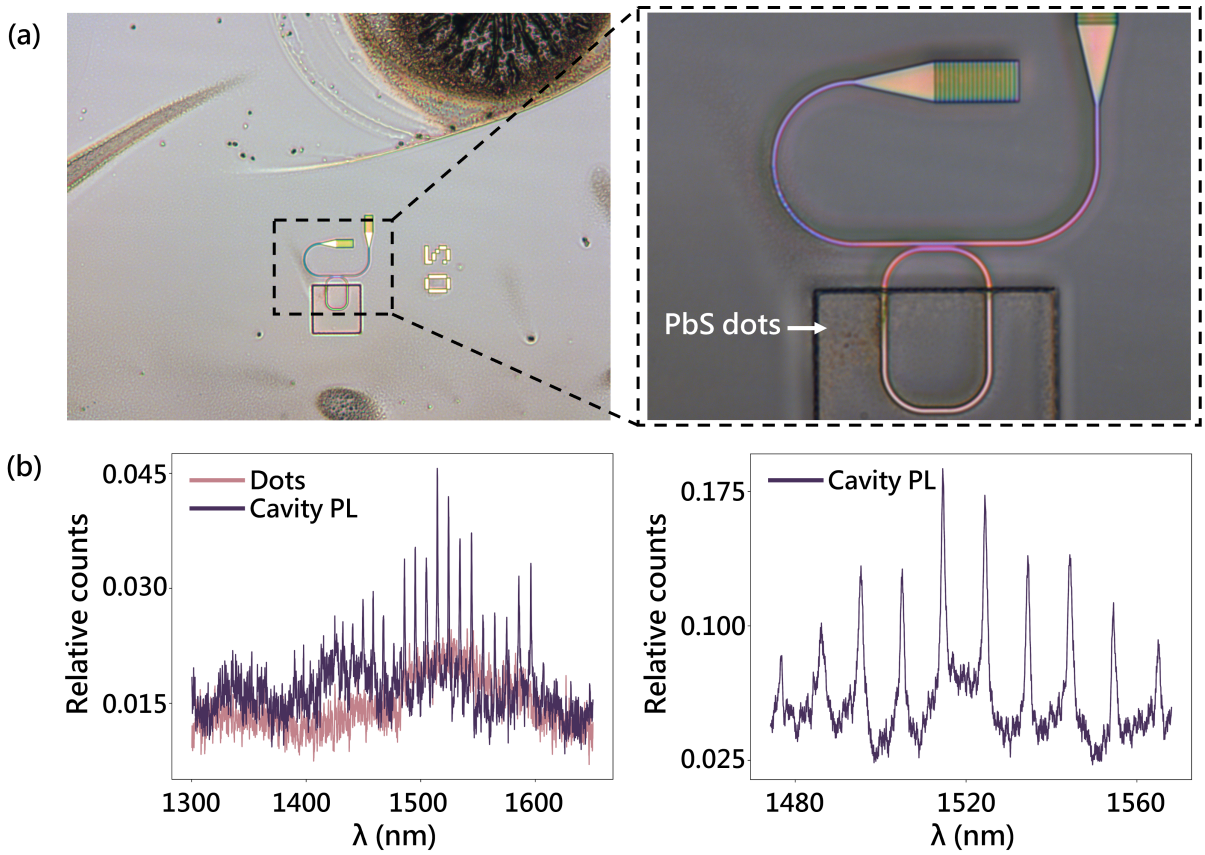

Figure 6.2: PL characterization of the coupled QD-cavity system. (a) Optical microscope images of the device showing PMMA window over the racetrack resonator with the spun on *PbS* colloidal QDs visible as brownish coffee-stains. On the right is a zoomed-in image of the window region, where we see clearly the PbS dots physically in contact with the resonator waveguide. (b) PL spectrum for the racetrack resonator coupled to *PbS* dots is observed in the telecom regime against the PL background of the bare QDs. The cavity coupled PL is only collected from the grating coupler using a pinhole to improve the signal-to-noise ratio.

operate in a regime where the emission from the dissipative QD can be funneled through the cavities to get highly indistinguishable output photons at somewhat low efficiencies. The proposed device design is depicted in Fig. 6.3 and a detailed discussion can be found in the referenced work. A big drawback of the above scheme is that it does not take care of the chemical instability issue and relies on there only being a single QD coupled to a cavity. Further improvements in the chemical synthesis of these dots as well as the development of more sophisticated methods of placing these dots on cavities are needed before solution-processed QDs can be used for obtaining single photon non-linearity at scale on a photonics platform.

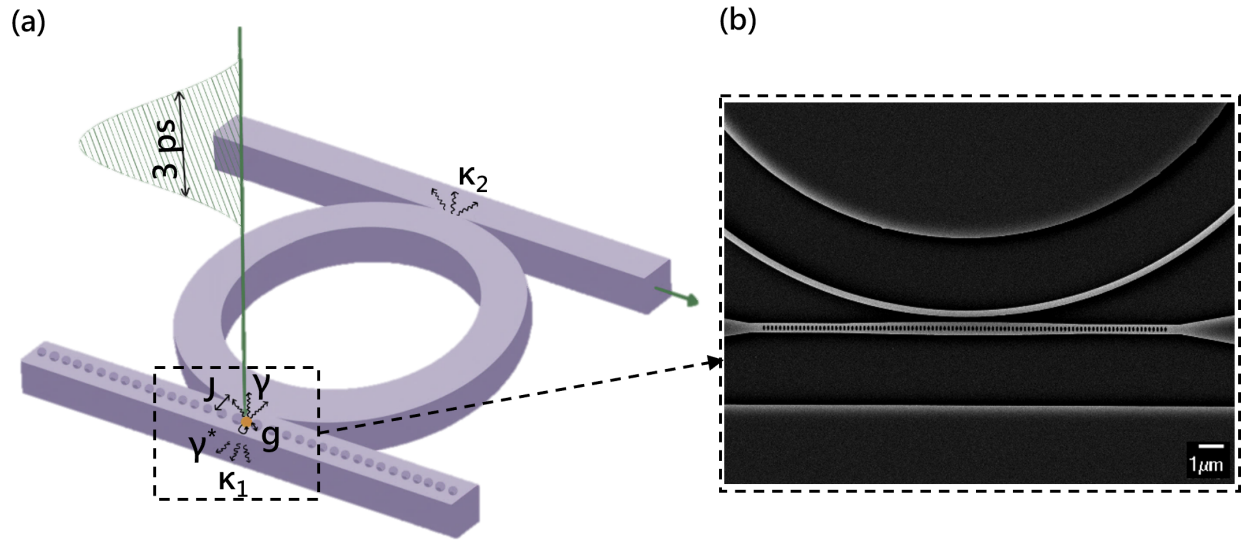

Figure 6.3: Experimental proposal to overcome dephasing rate limitation in colloidal QDs. (a) Design schematic depicting colloidal QD with decay rate γ and dephasing rate γ^* coupled to the nanobeam cavity with a coupling rate of g. The nanobeam cavity has a decay rate κ_1 and is coupled to a ring resonator with a coupling rate J. The ring resonator has a decay rate of κ_2. The QD is excited by 3 ps wide pulse with an amplitude of $P_o = 120\gamma$. The output is collected from the waveguide coupled to the ring resonator. (b) SEM image of a fabricated device structure inside the dotted black box shown in (a).

6.2 Concluding remarks

In this dissertation, we developed the design principles needed to realize photonic CCAs suitable for quantum simulation. We then experimentally demonstrated 1D photonic CCAs designed in accordance with these principles, which, when integrated with non-linear optical materials, would allow the realization of non-linear quantum Hamiltonians on a photonic platform.

However, as discussed in the last section, a significant amount of work needs to be done in order to realize scalable on-chip optical non-linearities. One of the more promising direction for exploring optical non-linearities in photonics comes from the recent progress made in induced defect centers in Si and SiC platforms. These emitters have already been shown in Si to allow for deterministic placement on a wafer-scale [90], emit single photons [77], and in SiC have been used to demonstrate optical super-radiance and cooperativities as high as 0.8 [76]. Our photonic CCAs, with their cladding-free design and extremely small mode volumes, are an ideal platform for investigating the possibility of realizing photon blockade and single-photon non-linearity using such defect centers on a foundry-compatible solid-state platform.

Another obvious direction that needs exploration is extending the device from $1D$ to $2D$ and therefore expanding the scope of Hamiltonians that can be implemented. While the scalability condition for the photonic CCAs remains the same in $2D$ as in $1D$, we need to develop more sophisticated control protocols that allow control on a $2D$-plane. Additionally, while the tomography algorithm described in Ch. 4 and Appendices A, B is applicable for $2D$ photonic lattices, it still needs to be experimentally demonstrated for $1D$ non-linear and $2D$ Hamiltonians. One of the $2D$ Hamiltonians of interest in this regard is the strained-graphene Hamiltonian, which was recently used as an illustrative example to demonstrate tomographically mappable topological optomechanical superconducting lattices. We can implement a similar structure in Si photonics and use our developed algorithm to find the Hamiltonian of the realized device. In Fig. 6.4 we show optical microscope images of such

$2D$ devices implementing the strained-graphene Hamiltonian and square lattice Hamiltonian, which are fitted with grating couplers along one of the edges as these are the minimum number of measurement ports needed to tomographically map the implemented Hamiltonians.

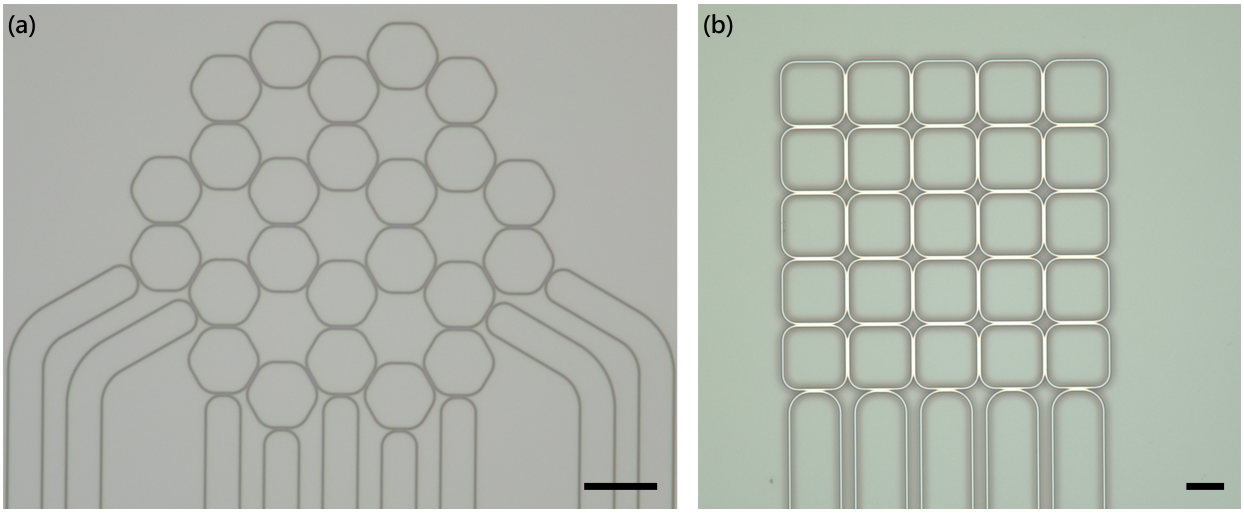

Figure 6.4: Optical microscope images of $2D$ photonic CCAs. (a) CCA implementing the strained-graphene Hamiltonian, scale bar: 20 μm. (b) CCA implementing a square lattice with real hopping rates, scale bar: 15 μm. The CCAs are fitted with grating couplers along one of the edges.

Another aspect of the optical design of CCAs that is of potential interest is the further reduction of mode volumes of the cavities that constitute the CCA to enhance the potential for light-matter interaction with the integrated materials. This, however, needs to be done in a manner that does not affect the scalability or addressability of the realized CCA. While the photonic crystal cavities allow for ultra-small mode volumes [91] it is in general hard to scale these to a large number of sites due to fabrication disorders [38] and their physical geometry not being readily amenable to a lot of interesting lattices. Recent progress in inverse-designed photonic cavities and cavity couplers [92] has opened a new avenue of research in implementing photonic CCAs consisting of high-Q and low mode volume cavities. As these inverse designed structures can be designed to be foundry compatible [93] they

avoid the scalability issue faced by standard photonic crystals. Additionally, as we have more control over the design parameters, we can use these to implement lattices in geometries and Hamiltonian elements in ranges that are not typically achievable using other methods. For example, in Fig. 6.5, we depict some of the coupled cavity structures we have fabricated up to this point (we thank Geun Ho Ahn and Prof. Jelena Vuckovic from Stanford University for helping us on this project and providing us with these designs). More investigations are required to characterize the exact coupling rates in these structures, but our preliminary measurements suggest that these allow us to achieve Q-factors in the order of a few tens of thousands and coupling rates exceeding 1 nm at telecom band frequencies. It can be inferred from the images that inverse designed structures are greatly promising for realizing unique lattice geometries with ultra-low mode volume resonators.

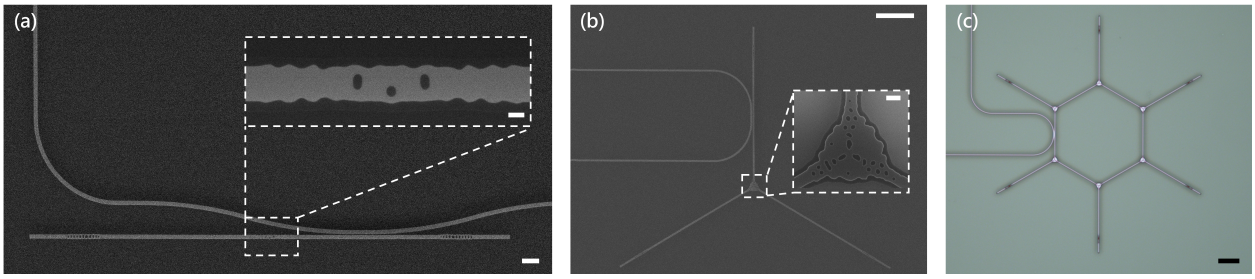

Figure 6.5: Images of inverse designed, coupled Fabry-Perot cavities. (a) SEM showing two Fabry-Perot cavities coupled via a two-way coupler, scale bar: 2 μm. Inset shows a zoom in of the coupler region, scale bar: 200 nm. (b) SEM showing three Fabry-Perot cavities coupled via an inverse designed three-way coupler, scale bar: 10 μm. Inset shows a zoom in of the coupler region, scale bar: 500 nm. (c) Optical micrograph of a snowflake shaped CCA realized by showing six three-way couplers, scale bar: 10 μm.

BIBLIOGRAPHY

[1] Erwin Schrödinger. An undulatory theory of the mechanics of atoms and molecules. *Physical review*, 28(6):1049, 1926.

[2] Richard P Feynman. Simulating physics with computers. In *Feynman and computation*, pages 133–153. CRC Press, 2018.

[3] Iulia Buluta and Franco Nori. Quantum simulators. *Science*, 326(5949):108–111, 2009.

[4] Immanuel Bloch. Ultracold quantum gases in optical lattices. *Nature physics*, 1(1):23–30, 2005.

[5] Christopher Monroe and Jungsang Kim. Scaling the ion trap quantum processor. *Science*, 339(6124):1164–1169, 2013.

[6] Karan K Mehta, Chi Zhang, Maciej Malinowski, Thanh-Long Nguyen, Martin Stadler, and Jonathan P Home. Integrated optical multi-ion quantum logic. *Nature*, 586(7830):533–537, 2020.

[7] Juan M Arrazola, Ville Bergholm, Kamil Brádler, Thomas R Bromley, Matt J Collins, Ish Dhand, Alberto Fumagalli, Thomas Gerrits, Andrey Goussev, Lukas G Helt, et al. Quantum circuits with many photons on a programmable nanophotonic chip. *Nature*, 591(7848):54–60, 2021.

[8] Pedram Roushan, Charles Neill, J Tangpanitanon, Victor M Bastidas, A Megrant, Rami Barends, Yu Chen, Z Chen, B Chiaro, A Dunsworth, et al. Spectroscopic signatures of localization with interacting photons in superconducting qubits. *Science*, 358(6367):1175–1179, 2017.

[9] Ruichao Ma, Brendan Saxberg, Clai Owens, Nelson Leung, Yao Lu, Jonathan Simon, and David I Schuster. A dissipatively stabilized mott insulator of photons. *Nature*, 566(7742):51–57, 2019.

[10] Eunjong Kim, Xueyue Zhang, Vinicius S Ferreira, Jash Banker, Joseph K Iverson, Alp Sipahigil, Miguel Bello, Alejandro González-Tudela, Mohammad Mirhosseini, and Oskar Painter. Quantum electrodynamics in a topological waveguide. *Physical Review X*, 11(1):011015, 2021.

[11] Xueyue Zhang, Eunjong Kim, Daniel K Mark, Soonwon Choi, and Oskar Painter. A superconducting quantum simulator based on a photonic-bandgap metamaterial. *Science*, 379(6629):278–283, 2023.

[12] Shayan Mookherjea, Jun Rong Ong, Xianshu Luo, and Lo Guo-Qiang. Electronic control of optical anderson localization modes. *Nature Nanotechnology*, 9(5):365–371, 2014.

[13] Alicia J Kollár, Mattias Fitzpatrick, and Andrew A Houck. Hyperbolic lattices in circuit quantum electrodynamics. *Nature*, 571(7763):45–50, 2019.

[14] Sunil Mittal, Venkata Vikram Orre, Guanyu Zhu, Maxim A Gorlach, Alexander Poddubny, and Mohammad Hafezi. Photonic quadrupole topological phases. *Nature Photonics*, 13(10):692–696, 2019.

[15] Abhi Saxena, Yueyang Chen, Zhuoran Fang, and Arka Majumdar. Photonic topological baths for quantum simulation. *ACS Photonics*, 9(2):682–687, 2022.

[16] Zihe Gao, Haoqi Zhao, Tianwei Wu, Xilin Feng, Zhifeng Zhang, Xingdu Qiao, Ching-Kai Chiu, and Liang Feng. Topological quadratic-node semimetal in a photonic microring lattice. *Nature Communications*, 14(1):3206, 2023.

[17] Amir Youssefi, Shingo Kono, Andrea Bancora, Mahdi Chegnizadeh, Jiahe Pan, Tatiana Vovk, and Tobias J Kippenberg. Topological lattices realized in superconducting circuit optomechanics. *Nature*, 612(7941):666–672, 2022.

[18] Han Zhao, Pei Miao, Mohammad H Teimourpour, Simon Malzard, Ramy El-Ganainy, Henning Schomerus, and Liang Feng. Topological hybrid silicon microlasers. *Nature communications*, 9(1):981, 2018.

[19] Stefan Krastanov, Mikkel Heuck, Jeffrey H Shapiro, Prineha Narang, Dirk R Englund, and Kurt Jacobs. Room-temperature photonic logical qubits via second-order nonlinearities. *Nature communications*, 12(1):191, 2021.

[20] Jueming Bao, Zhaorong Fu, Tanumoy Pramanik, Jun Mao, Yulin Chi, Yingkang Cao, Chonghao Zhai, Yifei Mao, Tianxiang Dai, Xiaojiong Chen, et al. Very-large-scale integrated quantum graph photonics. *Nature Photonics*, pages 1–9, 2023.

[21] Michael E Beverland, Prakash Murali, Matthias Troyer, Krysta M Svore, Torsten Hoeffler, Vadym Kliuchnikov, Guang Hao Low, Mathias Soeken, Aarthi Sundaram, and Alexander Vaschillo. Assessing requirements to scale to practical quantum advantage. *arXiv preprint arXiv:2211.07629*, 2022.

[22] Risheng Cheng, Yiyu Zhou, Sihao Wang, Mohan Shen, Towsif Taher, and Hong X Tang. A 100-pixel photon-number-resolving detector unveiling photon statistics. *Nature Photonics*, 17(1):112–119, 2023.

[23] Joshua Combes, Joseph Kerckhoff, and Mohan Sarovar. The slh framework for modeling quantum input-output networks. *Advances in Physics: X*, 2(3):784–888, 2017.

[24] Sunil Mittal. *Topological edge states in silicon photonics*. PhD thesis, Department of Electrical and Computer Engineering, University of Maryland, 2014.

[25] Miguel Bello, Gloria Platero, Juan Ignacio Cirac, and Alejandro González-Tudela. Unconventional quantum optics in topological waveguide qed. *Sci. Adv.*, 5(7):eaaw0297, 2019.

[26] Brandon M Anderson, Ruichao Ma, Clai Owens, David I Schuster, and Jonathan Simon. Engineering topological many-body materials in microwave cavity arrays. *Phys. Rev. X*, 6(4):041043, 2016.

[27] Oscar Viyuela, A Rivas, Simone Gasparinetti, Andreas Wallraff, Stefan Filipp, and Miguel A Martín-Delgado. Observation of topological uhlmann phases with superconducting qubits. *npj Quantum Inf.*, 4(1):1–6, 2018.

[28] Xin Wang, Tao Liu, Anton Frisk Kockum, Hong-Rong Li, and Franco Nori. Tunable chiral bound states with giant atoms. *Phys. Rev. Lett.*, 126:043602, Jan 2021.

[29] Michael J Hartmann. Quantum simulation with interacting photons. *J. Opt.*, 18(10):104005, 2016.

[30] Sunil Mittal, Jingyun Fan, Sanli Faez, Alan Migdall, Jacob M Taylor, and Mohammad Hafezi. Topologically robust transport of photons in a synthetic gauge field. *Phys. Rev. Lett.*, 113(8):087403, 2014.

[31] Mohammad Hafezi, S Mittal, J Fan, A Migdall, and JM Taylor. Imaging topological edge states in silicon photonics. *Nat. Photonics*, 7(12):1001–1005, 2013.

[32] Midya Parto, Steffen Wittek, Hossein Hodaei, Gal Harari, Miguel A Bandres, Jinhan Ren, Mikael C Rechtsman, Mordechai Segev, Demetrios N Christodoulides, and Mercedeh Khajavikhan. Edge-mode lasing in 1d topological active arrays. *Phys. Rev. Lett.*, 120(11):113901, 2018.

[33] P St-Jean, V Goblot, E Galopin, A Lemaître, T Ozawa, L Le Gratiet, I Sagnes, J Bloch, and A Amo. Lasing in topological edge states of a one-dimensional lattice. *Nat. Photonics*, 11(10):651–656, 2017.

[34] Shirin Afzal, Tyler J Zimmerling, Yang Ren, David Perron, and Vien Van. Realization of anomalous floquet insulators in strongly coupled nanophotonic lattices. *Phys. Rev. Lett.*, 124(25):253601, 2020.

[35] W. P. Su, J. R. Schrieffer, and A. J. Heeger. Solitons in polyacetylene. *Phys. Rev. Lett.*, 42:1698–1701, Jun 1979.

[36] János K Asbóth, László Oroszlány, and András Pályi. A short course on topological insulators. *Lect. Notes Phys.*, 919:997–1000, 2016.

[37] Devin L Underwood, Will E Shanks, Jens Koch, and Andrew A Houck. Low-disorder microwave cavity lattices for quantum simulation with photons. *Phys. Rev. A*, 86(2):023837, 2012.

[38] Arka Majumdar, Armand Rundquist, Michal Bajcsy, Vaishno D Dasika, Seth R Bank, and Jelena Vučković. Design and analysis of photonic crystal coupled cavity arrays for quantum simulation. *Phys. Rev. B*, 86(19):195312, 2012.

[39] Hermann A Haus and Weiping Huang. Coupled-mode theory. *Proc. IEEE*, 79(10):1505–1518, 1991.

[40] Kevin C Smith, Yueyang Chen, Arka Majumdar, and David J Masiello. Active tuning of hybridized modes in a heterogeneous photonic molecule. *Phys. Rev. Appl.*, 13(4):044041, 2020.

[41] John Clai Owens, Margaret G Panetta, Brendan Saxberg, Gabrielle Roberts, Srivatsan Chakram, Ruichao Ma, Andrei Vrajitoarea, Jonathan Simon, and David I Schuster. Chiral cavity quantum electrodynamics. *Nature Physics*, 18(9):1048–1052, 2022.

[42] Nathan Schine, Albert Ryou, Andrey Gromov, Ariel Sommer, and Jonathan Simon. Synthetic landau levels for photons. *Nature*, 534(7609):671–675, 2016.

[43] Horst L Stormer, Daniel C Tsui, and Arthur C Gossard. The fractional quantum hall effect. *Reviews of Modern Physics*, 71(2):S298, 1999.

[44] M Zahid Hasan and Charles L Kane. Colloquium: topological insulators. *Reviews of modern physics*, 82(4):3045, 2010.

[45] Ruichao Ma, Clai Owens, Aman LaChapelle, David I Schuster, and Jonathan Simon. Hamiltonian tomography of photonic lattices. *Physical Review A*, 95(6):062120, 2017.

[46] Abhi Saxena, Arnab Manna, Rahul Trivedi, and Arka Majumdar. Realizing tight-binding hamiltonians using site-controlled coupled cavity arrays. *arXiv preprint arXiv:2210.05070*, 2022.

[47] Daniel Burgarth, Koji Maruyama, and Franco Nori. Coupling strength estimation for spin chains despite restricted access. *Physical Review A*, 79(2):020305, 2009.

[48] Carlo Di Franco, Mauro Paternostro, and MS Kim. Hamiltonian tomography in an access-limited setting without state initialization. *Physical review letters*, 102(18):187203, 2009.

[49] Daniel Burgarth and Koji Maruyama. Indirect hamiltonian identification through a small gateway. *New Journal of Physics*, 11(10):103019, 2009.

[50] Koji Maruyama, Daniel Burgarth, Akihito Ishizaki, Takeji Takui, and K Birgitta Whaley. Application of indirect hamiltonian tomography to complex systems with short decoherence times. *Quantum Information & Computation*, 12(9-10):9–10, 2012.

[51] Daniel Burgarth, Koji Maruyama, and Franco Nori. Indirect quantum tomography of quadratic hamiltonians. *New Journal of Physics*, 13(1):013019, 2011.

[52] Jun Zhang and Mohan Sarovar. Quantum hamiltonian identification from measurement time traces. *Physical review letters*, 113(8):080401, 2014.

[53] Jun Zhang and Mohan Sarovar. Identification of open quantum systems from observable time traces. *Physical Review A*, 91(5):052121, 2015.

[54] Daniel Burgarth and Kazuya Yuasa. Quantum system identification. *Physical Review Letters*, 108(8):080502, 2012.

[55] Daniel Burgarth and Ashok Ajoy. Evolution-free hamiltonian parameter estimation through zeeman markers. *Physical Review Letters*, 119(3):030402, 2017.

[56] Christian Kokail, Rick van Bijnen, Andreas Elben, Benoît Vermersch, and Peter Zoller. Entanglement hamiltonian tomography in quantum simulation. *Nature Physics*, 17(8):936–942, 2021.

[57] Mohammad Hafezi, Eugene A Demler, Mikhail D Lukin, and Jacob M Taylor. Robust optical delay lines with topological protection. *Nature Physics*, 7(11):907–912, 2011.

[58] Dominik Hangleiter, Ingo Roth, Jens Eisert, and Pedram Roushan. Precise hamiltonian identification of a superconducting quantum processor. *arXiv preprint arXiv:2108.08319*, 2021.

[59] Clai Owens, Aman LaChapelle, Brendan Saxberg, Brandon M Anderson, Ruichao Ma, Jonathan Simon, and David I Schuster. Quarter-flux hofstadter lattice in a qubit-compatible microwave cavity array. *Physical Review A*, 97(1):013818, 2018.

[60] Rahul Trivedi, Marina Radulaski, Kevin A Fischer, Shanhui Fan, and Jelena Vučković. Photon blockade in weakly driven cavity quantum electrodynamics systems with many emitters. *Physical review letters*, 122(24):243602, 2019.

[61] Iacopo Carusotto, Andrew A Houck, Alicia J Kollár, Pedram Roushan, David I Schuster, and Jonathan Simon. Photonic materials in circuit quantum electrodynamics. *Nature Physics*, 16(3):268–279, 2020.

[62] J Robert Johansson, Paul D Nation, and Franco Nori. Qutip: An open-source python framework for the dynamics of open quantum systems. *Computer Physics Communications*, 183(8):1760–1772, 2012.

[63] Sunil Mittal, Elizabeth A Goldschmidt, and Mohammad Hafezi. A topological source of quantum light. *Nature*, 561(7724):502–506, 2018.

[64] Sunil Mittal, Venkata Vikram Orre, Elizabeth A Goldschmidt, and Mohammad Hafezi. Tunable quantum interference using a topological source of indistinguishable photon pairs. *Nature Photonics*, 15(7):542–548, 2021.

[65] Brent E Little, Sai T Chu, Hermann A Haus, JAFJ Foresi, and J-P Laine. Microring resonator channel dropping filters. *Journal of lightwave technology*, 15(6):998–1005, 1997.

[66] Joyce KS Poon, Jacob Scheuer, Yong Xu, and Amnon Yariv. Designing coupled-resonator optical waveguide delay lines. *JOSA B*, 21(9):1665–1673, 2004.

[67] Viktor Evgenevich Ivanov. *High temperature oxidation protection of tungsten*, volume 583. National Aeronautics and Space Administration, 1969.

[68] Guozhen Liang, Heqing Huang, Aseema Mohanty, Min Chul Shin, Xingchen Ji, Michael Joseph Carter, Sajan Shrestha, Michal Lipson, and Nanfang Yu. Robust, efficient, micrometre-scale phase modulators at visible wavelengths. *Nature Photonics*, 15(12):908–913, 2021.

[69] Hasitha Jayatilleka, Hossam Shoman, Lukas Chrostowski, and Sudip Shekhar. Photoconductive heaters enable control of large-scale silicon photonic ring resonator circuits. *Optica*, 6(1):84–91, 2019.

[70] Xiaoxiao Xue, Yi Xuan, Cong Wang, Pei-Hsun Wang, Yang Liu, Ben Niu, Daniel E Leaird, Minghao Qi, and Andrew M Weiner. Thermal tuning of kerr frequency combs in silicon nitride microring resonators. *Optics express*, 24(1):687–698, 2016.

[71] Momchil Minkov and Vincenzo Savona. Haldane quantum hall effect for light in a dynamically modulated array of resonators. *Optica*, 3(2):200–206, 2016.

[72] Mian Zhang, Cheng Wang, Yaowen Hu, Amirhassan Shams-Ansari, Tianhao Ren, Shanhui Fan, and Marko Lončar. Electronically programmable photonic molecule. *Nature Photonics*, 13(1):36–40, 2019.

[73] Huitao Shen, Bo Zhen, and Liang Fu. Topological band theory for non-hermitian hamiltonians. *Physical review letters*, 120(14):146402, 2018.

[74] Alen Senanian, Logan G Wright, Peter F Wade, Hannah K Doyle, and Peter L McMahon. Programmable large-scale simulation of bosonic transport in optical synthetic frequency lattices. *Nature Physics*, pages 1–7, 2023.

[75] Yueyang Chen, Albert Ryou, Max R Friedfeld, Taylor Fryett, James Whitehead, Brandi M Cossairt, and Arka Majumdar. Deterministic positioning of colloidal quantum dots on silicon nitride nanobeam cavities. *Nano Lett.*, 18(10):6404–6410, 2018.

[76] Daniil M Lukin, Melissa A Guidry, Joshua Yang, Misagh Ghezellou, Sattwik Deb Mishra, Hiroshi Abe, Takeshi Ohshima, Jawad Ul-Hassan, and Jelena Vučković. Two-emitter multimode cavity quantum electrodynamics in thin-film silicon carbide photonics. *Physical Review X*, 13(1):011005, 2023.

[77] Yoann Baron, Alrik Durand, Tobias Herzig, Mario Khoury, Sébastien Pezzagna, Jan Meijer, Isabelle Robert-Philip, Marco Abbarchi, Jean-Michel Hartmann, Shay Reboh, et al. Single g centers in silicon fabricated by co-implantation with carbon and proton. *Applied Physics Letters*, 121(8), 2022.

[78] Albert Ryou, David Rosser, Abhi Saxena, Taylor Fryett, and Arka Majumdar. Strong photon antibunching in weakly nonlinear two-dimensional exciton-polaritons. *Physical Review B*, 97(23):235307, 2018.

[79] Abhi Saxena, Yueyang Chen, Albert Ryou, Carlos G Sevilla, Peipeng Xu, and Arka Majumdar. Improving indistinguishability of single photons from colloidal quantum dots using nanocavities. *ACS Photonics*, 6(12):3166–3173, 2019.

[80] Anton V Zasedatelev, Anton V Baranikov, Denis Sannikov, Darius Urbonas, Fabio Scafirimuto, Vladislav Yu Shishkov, Evgeny S Andrianov, Yurii E Lozovik, Ullrich

Scherf, Thilo Stöferle, et al. Single-photon nonlinearity at room temperature. *Nature*, 597(7877):493–497, 2021.

[81] Francesco Morichetti, Stefano Grillanda, and A Melloni. Breakthroughs in photonics 2013: Toward feedback-controlled integrated photonics. *IEEE Photonics Journal*, 6(2):1–6, 2014.

[82] Stefano Grillanda, Marco Carminati, Francesco Morichetti, Pietro Ciccarella, Andrea Annoni, Giorgio Ferrari, Michael Strain, Marc Sorel, Marco Sampietro, and Andrea Melloni. Non-invasive monitoring and control in silicon photonics using cmos integrated electronics. *Optica*, 1(3):129–136, 2014.

[83] Steven L Brunton and J Nathan Kutz. *Data-driven science and engineering: Machine learning, dynamical systems, and control*. Cambridge University Press, 2022.

[84] Xinru Ji, Junqiu Liu, Jijun He, Rui Ning Wang, Zheru Qiu, Johann Riemensberger, and Tobias J Kippenberg. Compact, spatial-mode-interaction-free, ultralow-loss, nonlinear photonic integrated circuits. *Communications Physics*, 5(1):84, 2022.

[85] Kevin M Birnbaum, Andreea Boca, Russell Miller, Allen D Boozer, Tracy E Northup, and H Jeff Kimble. Photon blockade in an optical cavity with one trapped atom. *Nature*, 436(7047):87–90, 2005.

[86] Andrei Faraon, Ilya Fushman, Dirk Englund, Nick Stoltz, Pierre Petroff, and Jelena Vučković. Coherent generation of non-classical light on a chip via photon-induced tunnelling and blockade. *Nature Physics*, 4(11):859–863, 2008.

[87] Arka Majumdar and Dario Gerace. Single-photon blockade in doubly resonant nanocavities with second-order nonlinearity. *Physical Review B*, 87(23):235319, 2013.

[88] Hao A Nguyen, David Sharp, Johannes E Froech, Yi-Yu Cai, Shenwei Wu, Madison Monahan, Christopher Munley, Arnab Manna, Arka Majumdar, Cherie R Kagan, et al. Deterministic quantum light arrays from giant silica-shelled quantum dots. *ACS Applied Materials & Interfaces*, 15(3):4294–4302, 2022.

[89] GL Whitworth, M Dalmases, N Taghipour, and G Konstantatos. Solution-processed pbs quantum dot infrared laser with room-temperature tunable emission in the optical telecommunications window. *Nature photonics*, 15(10):738–742, 2021.

[90] Michael Hollenbach, Nico Klingner, Nagesh S Jagtap, Lothar Bischoff, Ciarán Fowley, Ulrich Kentsch, Gregor Hlawacek, Artur Erbe, Nikolay V Abrosimov, Manfred Helm, et al. Wafer-scale nanofabrication of telecom single-photon emitters in silicon. *Nature Communications*, 13(1):7683, 2022.

[91] Jun Zhou, Jiajiu Zheng, Zhuoran Fang, Peipeng Xu, and Arka Majumdar. Ultra-low mode volume on-substrate silicon nanobeam cavity. *Optics Express*, 27(21):30692–30699, 2019.

[92] Geun Ho Ahn, Ki Youl Yang, Rahul Trivedi, Alexander D White, Logan Su, Jinhie Skarda, and Jelena Vuckovic. Photonic inverse design of on-chip microresonators. *ACS Photonics*, 9(6):1875–1881, 2022.

[93] Ki Youl Yang, Chinmay Shirpurkar, Alexander D White, Jizhao Zang, Lin Chang, Farshid Ashtiani, Melissa A Guidry, Daniil M Lukin, Srinivas V Pericherla, Joshua Yang, et al. Multi-dimensional data transmission using inverse-designed silicon photonics and microcombs. *Nature Communications*, 13(1):7862, 2022.

Appendix A

SINGLE PHOTON SCATTERING TOMOGRAPHY

A.1 Model

For reconstructing the linear part of the Hamiltonian we restrict ourselves to single photon excitation subspace. The Hamiltonian of the photonic lattice $(\mathcal{V}, \mathcal{E})$ in this subspace can be written as (basis restricted to 1 photon):

$$H^{(1)} = \sum_{v \in \mathcal{V}} \mu_v a_v^\dagger a_v + \sum_{u,v \in \mathcal{E}} J_{v,u} a_v^\dagger a_u \tag{A.1}$$

where the parameters $J_{v,u} \in \mathbb{C}$ (the coupling strengths s.t. $J_{v,u} = J_{u,v}^*$), $\mu_v \in \mathbb{C}$ (the onsite potential) need to be tomographically mapped. Experimentally, we have access to the single photon reflection and transmission spectra for all the sites forming the outermost perimeter $\mathcal{V}_0$. From one-photon scattering theory we know that the transmission and reflection spectra of a photon lattice is given by [46, 60]:

$$|T_{v,u}(\omega)|^2 = \gamma_v \gamma_u \left| \sum_\alpha \frac{\langle G|a_v|r_\alpha^{(1)}\rangle \langle l_\alpha^{(1)}|a_u^\dagger|G\rangle}{\omega - E_\alpha^{(1)}} \right|^2 \tag{A.2}$$

$$|R_{v,v}(\omega)|^2 = \left| 1 - j\gamma_v \sum_\alpha \frac{\langle G|a_v|r_\alpha^{(1)}\rangle \langle l_\alpha^{(1)}|a_v^\dagger|G\rangle}{\omega - E_\alpha^{(1)}} \right|^2 \tag{A.3}$$

where γ_v, γ_u denote coupling rates to input/output ports at site u, v, $\langle l_\alpha^{(1)}|, |r_\alpha^{(1)}\rangle$ denote the left and right eigenvectors of H in the 1^{st} excitation subspace and $|G\rangle$ denotes the vacuum state of the lattice with zero photons. Fitting these spectra then allows determination of the eigenenergies of $H^{(1)}$: $E_\alpha^{(1)}$, as well as the coefficients:

$$M_{\alpha,v,u}^{(1)} = \langle G|a_v|r_\alpha^{(1)}\rangle \langle l_\alpha^{(1)}|a_u^\dagger|G\rangle, \ \forall \ u, v \ \in \ \mathcal{V}_0. \tag{A.4}$$

where we note that: $\sum_\alpha M_{\alpha.v,u} = \delta_{v,u}$.

A.2 Algorithm

The tomography can be then performed as follows: Let N_v denote the neighborhood of site v s.t. $N_v = u \cup v'$ s.t. $u \in \mathcal{V}_0, v' \in \mathcal{V}_1$. We can expand about v to write:

$$(E_\alpha^{(1)} - \mu_v)\langle v|r_\alpha^{(1)}\rangle = J_{v,v'}\langle v'|r_\alpha^{(1)}\rangle + \sum_{u\in N_v - v'} J_{v,u}\langle u|r_\alpha^{(1)}\rangle \tag{A.5}$$

$$(E_\alpha^{(1)} - \mu_v)\langle l_\alpha^{(1)}|v\rangle = J^*_{v,v'}\langle l_\alpha^{(1)}|v'\rangle + \sum_{u\in N_v - v'} J^*_{v,u}\langle l_\alpha^{(1)}|u\rangle \tag{A.6}$$

Now, multiplying Eq. A.5 by $\langle l_\alpha^{(1)}|v\rangle$ and summing over α gives μ_v as:

$$\mu_v = \sum_\alpha E_\alpha^{(1)} M_{\alpha.v,v} \tag{A.7}$$

To get $J_{v,u}$ we multiply Eq. A.5 by $\langle l_\alpha^{(1)}|u\rangle$ and sum over α to get:

$$J_{v,u} = \sum_\alpha (E_\alpha^{(1)} - \mu_v) M_{\alpha,v,u} = \sum_\alpha E_\alpha^{(1)} M_{\alpha,v,u} \tag{A.8}$$

Multiplying Eqs. A.5, A.6 and summing over α then gives:

$$\sum_\alpha (E_\alpha^{(1)} - \mu_v)^2 M_{\alpha,v,v} = \sum_{u\in N_v - v'} |J_{v,u}|^2 + |J_{v,v'}|^2 \tag{A.9}$$

This allows us to obtain $J_{v',v} = |J_{v',v}|$.

Now taking all the terms associated with sites in $\mathcal{V}_0$ onto L.H.S. and again multiplying Eqs. A.5, A.6 gives:

$$\Big[(E_\alpha^{(1)} - \mu_v)\langle v|r_\alpha^{(1)}\rangle - \sum_{u\in N_v - v'} J_{v,u}\langle u|r_\alpha^{(1)}\rangle\Big]\Big[(E_\alpha^{(1)} - \mu_v)\langle l_\alpha^{(1)}|v\rangle - \sum_{u\in N_v - v'} J^*_{u,v}\langle l_\alpha^{(1)}|u\rangle\Big] = |J_{v',v}|^2 M_{\alpha,v',v'} \tag{A.10}$$

Using the values of experimentally extracted $M_{\alpha,v,u}, M_{\alpha,u,v}, M_{\alpha,u_1,u_2} \; \forall \; u_1, u_2 \in u$ gives us the values of $M_{\alpha,v',v'} \; \forall \; \alpha$. Now multiplying Eq. A.5 by $\langle l_\alpha^{(1)}|v\rangle$, rearranging the terms and again using $M_{\alpha,u,v}$ also gives:

$$M_{\alpha,v',v} = \frac{1}{J_{v',v}}\Big[(E_\alpha^{(1)} - \mu_v) M_{\alpha,v,v} - \sum_{u\in N_v - v'} J_{v,u} M_{\alpha,u,v}\Big] \tag{A.11}$$

and similarly multiplying Eq. A.6 by $\langle v|r_\alpha^{(1)}\rangle$, rearranging the terms and using $M_{\alpha,v,u}$ gives:

$$M_{\alpha,v,v'} = \frac{1}{J^*_{v,v'}}\Big[(E_\alpha^{(1)} - \mu_v)M_{\alpha,v,v} - \sum_{u\in N_v - v'} J^*_{v,u}M_{\alpha,v,u}\Big] \tag{A.12}$$

To complete the recursion now we need to find $M_{\alpha,v',u'}, M_{\alpha,u',v'}, M_{\alpha,u'_1,u'_2}$ where $u' \in N_{v'} - v'' = v \cup (N_{v'} \cap \mathcal{V}_1)$. First for $M^\alpha_{v',u'}$, we know that:

$$M_{\alpha,v',v}M_{\alpha,v,u}M_{\alpha,u,u'} = \langle v'|r_\alpha^{(1)}\rangle\langle l_\alpha^{(1)}|v\rangle v|r_\alpha^{(1)}\rangle\langle l_\alpha^{(1)}|u\rangle\langle u|r_\alpha^{(1)}\rangle\langle l_\alpha^{(1)}|u'\rangle \tag{A.13}$$

$$\implies M_{\alpha,v',v}M_{\alpha,v,u}M_{\alpha,u,u'} = \langle v'|r_\alpha^{(1)}\rangle\langle l_\alpha^{(1)}|u'\rangle\langle v|r_\alpha^{(1)}\rangle\langle l_\alpha^{(1)}|v\rangle\langle u|r_\alpha^{(1)}\rangle\langle l_\alpha^{(1)}|u\rangle \tag{A.14}$$

$$\implies M_{\alpha,v',v}M_{\alpha,v,u}M_{\alpha,u,u'} = \langle v'|r_\alpha^{(1)}\rangle\langle l_\alpha^{(1)}|u'\rangle M_{\alpha,v,v}M_{\alpha,u,u} \tag{A.15}$$

$$\implies M_{\alpha,v',u'} = \frac{M_{\alpha,v',v}M_{\alpha,v,u}M_{\alpha,u,u'}}{M_{\alpha,v,v}M_{\alpha,u,u}} \tag{A.16}$$

Similarly $M_{\alpha,u',v'}$ can be written as:

$$M_{\alpha,u',v'} = \frac{M_{\alpha,u',u}M_{\alpha,u,v}M_{\alpha,v,v'}}{M_{\alpha,u,u}M_{\alpha,v,v}} \tag{A.17}$$

Similarly for M_{α,u'_1,u'_2},

$$M_{\alpha,u'_1,v'}M_{\alpha,v',u'_2} = \langle u'_1|r_\alpha^{(1)}\rangle\langle l_\alpha^{(1)}|v'\rangle\langle v'|r_\alpha^{(1)}\rangle\langle l_\alpha^{(1)}|u'_2\rangle \tag{A.18}$$

$$\implies M_{\alpha,u'_1,v'}M_{\alpha,v',u'_2} = \langle u'_1|r_\alpha^{(1)}\rangle\langle l_\alpha^{(1)}|u'_2\rangle\langle v'|r_\alpha^{(1)}\rangle\langle l_\alpha^{(1)}|v'\rangle \tag{A.19}$$

$$\implies M_{\alpha,u'_1,u'_2} = \frac{M_{\alpha,u'_1,v'}M_{\alpha,v',u'_2}}{M_{\alpha,v',v'}} \tag{A.20}$$

At the end of this part we have determined $H^{(0)} + H^{(1)}$, and hence the eigenvectors $|r_\alpha^{(1)}\rangle$, $\langle l_\alpha^{(1)}| \;\forall\; \alpha$.

A.3 Illustration of one exceptional case: Corner of a square lattice

As we discussed in Ch.4 not all hopping rates along the edges connecting two arbitrary perimeters $\mathcal{V}_n, \mathcal{V}_{n+1}$ can be assumed to be positive. We dealt with the general anomalous cases in the chapter. Here we will illustrate a very commonly encountered sub-case of the general exceptional cases: the case of a corner of a square lattice depicted in Fig. A.1.

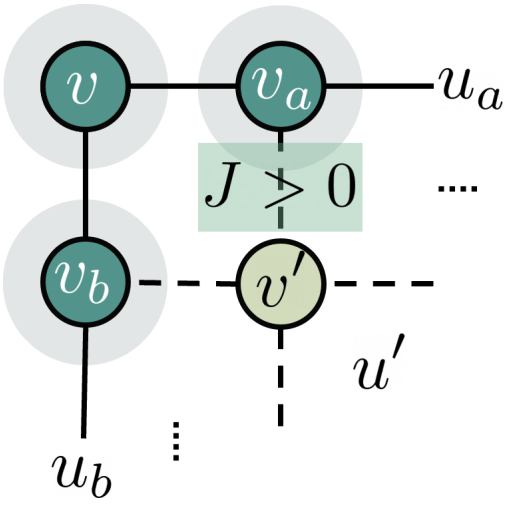

Figure A.1: Schematic depicting a corner of a square photonic graph. The algorithm allows us to assume hopping rate along one of the edges to be $+ve$.

We first expand about v_a to write:

$$(E_\alpha^{(1)} - \mu_{v_a})\langle v_a|r_\alpha^{(1)}\rangle = J_{v_a,v'}\langle v'|r_\alpha^{(1)}\rangle + \sum_{u\in N_{v_a}-v'} J_{v_a,u}\langle u|r_\alpha^{(1)}\rangle \tag{A.21}$$

$$(E_\alpha^{(1)} - \mu_{v_a})\langle l_\alpha^{(1)}|v_a\rangle = J^*_{v_a,v'}\langle l_\alpha^{(1)}|v'\rangle + \sum_{u\in N_{v_a}-v'} J^*_{v_a,u}\langle l_\alpha^{(1)}|u\rangle \tag{A.22}$$

and about v_b to write:

$$(E_\alpha^{(1)} - \mu_{v_b})\langle v_b|r_\alpha^{(1)}\rangle = J_{v_b,v'}\langle v'|r_\alpha^{(1)}\rangle + \sum_{u\in N_{v_b}-v'} J_{v_b,u}\langle u|r_\alpha^{(1)}\rangle \tag{A.23}$$

$$(E_\alpha^{(1)} - \mu_{v_b})\langle l_\alpha^{(1)}|v_b\rangle = J^*_{v_b,v'}\langle l_\alpha^{(1)}|v'\rangle + \sum_{u\in N_{v_b}-v'} J^*_{v_b,u}\langle l_\alpha^{(1)}|u\rangle \tag{A.24}$$

In the closed loop formed by v, v_a, v', v_b we can assume one of the non-determined edges to have a $+ve$ hopping rate. Let $J_{v_a,v'}$ be such that $|J_{v_a,v'}| = J_{v_a,v'}$. Then we want to uniquely determine $J_{v_b,v'}$ and the rest of the quantities needed for the continuation of the algorithm. Let u_a, u_b denotes sites as $u_a \in N_{v_a} - v'$ and $u_b \in N_{v_b} - v'$. For site v_a we can use the

following relations without any change:

$$\mu_{v_a} = \sum_{\alpha} E_{\alpha}^{(1)} M_{\alpha,v_a,v_a} \tag{A.25}$$

$$J_{v_a,u_a} = \sum_{\alpha} E_{\alpha}^{(1)} M_{\alpha,v_a,u_a} \tag{A.26}$$

Multiplying Eqs. A.21, A.22 and summing over α then gives:

$$\sum_{\alpha} (E_{\alpha} - \mu_{v_a})^2 M_{\alpha,v_a,v_a} = \sum_{u_a \in N_{v_a} - v'} |J_{v_a,u_a}|^2 + |J_{v_a,v'}|^2 \tag{A.27}$$

This allows us to obtain $J_{v_a,v'} = |J_{v_a,v'}|$.

Now taking all the terms associated with sites other than v' onto L.H.S. and again multiplying Eqs. A.21, A.22 gives:

$$\Big[(E_{\alpha}^{(1)} - \mu_{v_a})\langle v_a|r_{\alpha}^{(1)}\rangle - \sum_{u_a \in N_{v_a} - v'} J_{v_a,u_a}\langle u_a|r_{\alpha}^{(1)}\rangle\Big]\Big[(E_{\alpha}^{(1)} - \mu_{v_a})\langle l_{\alpha}^{(1)}|v_a\rangle - \sum_{u_a \in N_{v_a} - v'} J_{v_a,u_a}^{*}\langle l_{\alpha}^{(1)}|u_a\rangle\Big] = |J_{v_a,v'}|^2 M_{\alpha,v',v'} \tag{A.28}$$

Multiplying Eq. A.21 by $\langle l_{\alpha}^{(1)}|v_a\rangle$ gives:

$$M_{\alpha,v',v_a} = \frac{1}{J_{v_a,v'}}\Big[(E_{\alpha}^{(1)} - \mu_{v_a}) M_{\alpha,v_a,v_a} - \sum_{u_a \in N_{v_a} - v'} J_{v_a,u_a} M_{\alpha,v_a,u_a}\Big] \tag{A.29}$$

and similarly multiplying Eq. A.22 by $\langle v_a|r_{\alpha}^{(1)}\rangle$, rearranging the terms gives:

$$M_{\alpha,v_a,v'} = \frac{1}{J_{v_a,v'}^{*}}\Big[(E_{\alpha}^{(1)} - \mu_{v_a}) M_{\alpha,v_a,v_a} \sum_{u_a \in N_{v_a} - v'} J_{v_a,u_a}^{*} M_{\alpha,v_a,u_a}\Big] \tag{A.30}$$

Now using the closed loop formed by v, v_a, v', v_b we can write:

$$M_{\alpha,v',v_b} = \frac{M_{\alpha,v',v_a} M_{\alpha,v_a,v} M_{\alpha,v,v_b}}{M_{\alpha,v_a,v_a} M_{\alpha,v,v}} \tag{A.31}$$

$$M_{\alpha,v_b,v'} = \frac{M_{\alpha,v_b,v} M_{\alpha,v,v_a} M_{\alpha,v_a,v'}}{M_{\alpha,v,v} M_{\alpha,v_a,v_a}} \tag{A.32}$$

The equations for site v can be written trivially. Finally, for site v_b we have:

$$\mu_{v_b} = \sum_{\alpha} E_{\alpha}^{(1)} M_{\alpha,v_b,v_b} \tag{A.33}$$

$$J_{v_b,u_b} = \sum_{\alpha} E_{\alpha}^{(1)} M_{\alpha,u_b,v_b} \tag{A.34}$$

and finally to determine the complex $J_{v_b,v'}$ we can now just use Eq. A.33 to write:

$$J_{v_b,v'} = \sum_{\alpha} E_{\alpha}^{(1)} M_{\alpha,v_b,v'} \tag{A.35}$$

Which completes the illustration.

Appendix B

TWO-PHOTON SCATTERING TOMOGRAPHY

To construct the non-linear part of the Hamiltonian we need to work in a higher excitation subspace. The simplest of these is the two-photon subspace. The Hamiltonian of a photonic lattice in the two-photon excitation subspace can be written as a part of the full Hamiltonian as (basis restricted to 2 photons):

$$H = \sum_{v\in\mathcal{V}} \mu_v a_v^\dagger a_v + \frac{\chi_v}{2} a_v^{\dagger 2} a_v^2 + \sum_{u,v\in\mathcal{E}} J_{v,u} a_v^\dagger a_u = H^{(0)} + H^{(1)} + H^{(2)} \tag{B.1}$$

where the parameters $\chi_v \in \mathbb{R}$ (the onsite anharmonicity) need to be mapped. The most commonly used two-photon measurement is the second-order auto-correlation function $g^{(2)}(0,\omega)$. We use two photon scattering theory to determine the expression for $g^{(2)}(0,\omega)$ in the next section.

B.1 Two-photon scattering

To calculate $g^{(2)}(0,\omega)$ we first need to find the two-photon correlation function under a weak continuous laser. Let the two-photon correlation function when the input laser at frequency ω_L is parked at site u and scattered photons are collected at sites v, w at time τ_1, τ_2 be given by $F_{u,v,w}(\tau_1,\tau_2,\omega_L)$ where $v,u,w \in \mathcal{V}_0$. Then the second-order auto-correlation function $g^{(2)}_{v,u}(0,\omega_L)$ measured at site v when input laser is parked at site u can then be written as [60]:

$$g^{(2)}_{v,u}(0,\omega_L) = \frac{\gamma_v\gamma_u |F_{u,v,v}(0,0,\omega_L)|^2}{4|T_{v,u}(\omega_L)|^4} \tag{B.2}$$

where γ_v, γ_u denote coupling rates to input/output ports at site u, v. Hence, we need to determine an expression for $F_{u,v,w}(\tau_1,\tau_2,\omega_L)$, To begin we can write:

$$F_{u,v,w}(\tau_1,\tau_2,\omega_L) = \int_{t_1,t_2=-\infty}^{\infty} \langle \mathrm{G}|\mathcal{T}\left\{\tilde{a}_v(\tau_1)\tilde{a}_w(\tau_2)\tilde{a}_u^\dagger(t_1)\tilde{a}_u^\dagger(t_2)\right\}|\mathrm{G}\rangle e^{-j\omega_L(t_1+t_2)} dt_1 dt_2 \tag{B.3}$$

where $|G\rangle$ is the ground state of the photonic lattice, $\mathcal{T}$ indicates chronological ordering which for a given set of time indices orders the operators in decreasing order of the time indices and the operators $\tilde{a}_i(t)$ are given by $\tilde{a}_i(t) = e^{jHt}ae^{-jHt}$. Since the above expression is symmetric with respect to exchange of time indices τ_1, τ_2 and t_1, t_2 we can without loss of generality assume that $\tau_1 > \tau_2$ and $t_1 > t_2$. Then we can split the integral into two cases, depending on whether $\tau_1 > t_1 > \tau_2 > t_2$ or $\tau_1 > \tau_2 > t_1 > t_2$.

$$F_{u,v,w}(\tau_1, \tau_2, \omega_L) = 2\left(I_1 + I_2\right) \tag{B.4}$$

s.t.

$$I_1 = \int_{t_1=\tau 2}^{\tau_1}\int_{t_2=-\infty}^{\tau_2} e^{-j\omega_L(t_1+t_2)}\langle \mathrm{G}|\tilde{a}_v(\tau_1)\tilde{a}_u^\dagger(t_1)\tilde{a}_w(\tau_2)\tilde{a}_u^\dagger(t_2)|\mathrm{G}\rangle dt_1 dt_2 \tag{B.5}$$

$$I_2 = \int_{t_1=-\infty}^{\tau_2}\int_{t_2=-\infty}^{t_1} e^{-j\omega_L(t_1+t_2)}\langle \mathrm{G}|\tilde{a}_v(\tau_1)\tilde{a}_w(\tau_2)\tilde{a}_u^\dagger(t_1)\tilde{a}_u^\dagger(t_2)|\mathrm{G}\rangle dt_1 dt_2 \tag{B.6}$$

First evaluating I_1:

$$I_1 = \int_{t_1=\tau 2}^{\tau_1}\int_{t_2=-\infty}^{\tau_2} e^{-j\omega_L(t_1+t_2)}\langle \mathrm{G}|\tilde{a}_v(\tau_1)\tilde{a}_u^\dagger(t_1)|\mathrm{G}\rangle\langle \mathrm{G}|\tilde{a}_w(\tau_2)\tilde{a}_u^\dagger(t_2)|\mathrm{G}\rangle dt_1 dt_2 \tag{B.7}$$

$$= \int_{t_1=\tau 2}^{\tau_1} e^{-j\omega_L t_1}\langle \mathrm{G}|\tilde{a}_v(\tau_1)\tilde{a}_u^\dagger(t_1)|\mathrm{G}\rangle dt_1 \int_{t_2=-\infty}^{\tau_2} e^{-j\omega_L t_2}\langle \mathrm{G}|\tilde{a}_w(\tau_2)\tilde{a}_u^\dagger(t_2)|\mathrm{G}\rangle dt_2 \tag{B.8}$$

The second of these integrals can be evaluated as (note that: $e^{-jHx}|\mathrm{G}\rangle = |\mathrm{G}\rangle$):

$$\int_{t_2=-\infty}^{\tau_2} e^{-j\omega_L t_2}\langle \mathrm{G}|\tilde{a}_w(\tau_2)\tilde{a}_u^\dagger(t_2)|\mathrm{G}\rangle dt_2 = \int_{t_2=-\infty}^{\tau_2} e^{-j\omega_L t_2}\langle \mathrm{G}|a_w e^{-jH^{(1)}(\tau_2-t_2)}a_u^\dagger|\mathrm{G}\rangle dt_2 \tag{B.9}$$

$$= \int_{t_2=-\infty}^{\tau_2} e^{-j\omega_L t_2}\sum_k \langle \mathrm{G}|a_w|r_k^{(1)}\rangle\langle l_k^{(1)}|a_u^\dagger|\mathrm{G}\rangle e^{-jE_k^{(1)}(\tau_2-t_2)}dt_2 \tag{B.10}$$

$$= \sum_k \langle \mathrm{G}|a_w|r_k^{(1)}\rangle\langle l_k^{(1)}|a_u^\dagger|\mathrm{G}\rangle e^{-jE_k^{(1)}\tau_2}\int_{t_2=-\infty}^{\tau_2} e^{-jt_2(\omega_L-E_k^{(1)})}dt_2 \tag{B.11}$$

$$= \sum_k \frac{\langle \mathrm{G}|a_w|r_k^{(1)}\rangle\langle l_k^{(1)}|a_u^\dagger|\mathrm{G}\rangle}{j(E_k^{(1)}-\omega_L)}e^{-j\omega_L\tau_2} \tag{B.12}$$

Similarly for the first integral:

$$\int_{t_1=-\tau_2}^{\tau_1} e^{-j\omega_L t_1}\langle \mathrm{G}|\tilde{a}_v(\tau_1)\tilde{a}_u^\dagger(t_1)|\mathrm{G}\rangle dt_1 = \int_{\tau_2}^{\tau_1} e^{-j\omega_L t_1}\langle \mathrm{G}|a_v e^{-jH^{(1)}(\tau_1-t_1)}a_u^\dagger|\mathrm{G}\rangle dt_1 \tag{B.13}$$

$$= \int_{\tau_2}^{\tau_1} e^{-j\omega_L t_1}\sum_k \langle \mathrm{G}|a_v|r_k^{(1)}\rangle\langle l_k^{(1)}|a_u^\dagger|\mathrm{G}\rangle e^{-jE_k^{(1)}(\tau_1-t_1)}dt_1 \tag{B.14}$$

$$= \sum_k \langle \mathrm{G}|a_v|r_k^{(1)}\rangle\langle l_k^{(1)}|a_u^\dagger|\mathrm{G}\rangle \int_{\tau_2}^{\tau_1} e^{-jt_1(\omega_L-E_k^{(1)})}e^{-jE_k^{(1)}\tau_1}dt_1 \tag{B.15}$$

$$= \sum_k \frac{\langle \mathrm{G}|a_v|r_k^{(1)}\rangle\langle l_k^{(1)}|a_u^\dagger|\mathrm{G}\rangle}{j(E_k^{(1)}-\omega_L)}e^{-j\omega_L\tau_1}(1-e^{-j(E_k^{(1)}-\omega_L)(\tau_1-\tau_2)}) \tag{B.16}$$

Hence I_1 can be written as:

$$I_1 = \sum_{k_2} \frac{\langle \mathrm{G}|a_v|r_{k_2}^{(1)}\rangle\langle l_{k_2}^{(1)}|a_u^\dagger|\mathrm{G}\rangle}{j(E_{k_2}^{(1)}-\omega_L)}e^{-j\omega_L\tau_1}(1-e^{-j(E_{k_2}^{(1)}-\omega_L)(\tau_1-\tau_2)})\sum_{k_1}\frac{\langle \mathrm{G}|a_w|r_{k_1}^{(1)}\rangle\langle l_{k_1}^{(1)}|a_u^\dagger|\mathrm{G}\rangle}{j(E_{k_1}^{(1)}-\omega_L)}e^{-j\omega_L\tau_2} \tag{B.17}$$

Moving onto I_2:

$$I_2 = \int_{t_1=-\infty}^{\tau_2}\int_{t_2=-\infty}^{t_1} e^{-j\omega_L(t_1+t_2)}\langle \mathrm{G}|\tilde{a}_v(\tau_1)\tilde{a}_w(\tau_2)\tilde{a}_u^\dagger(t_1)\tilde{a}_u^\dagger(t_2)|\mathrm{G}\rangle dt_1 dt_2 \tag{B.18}$$

$$= \int_{t_1=-\infty}^{\tau_2}\int_{t_2=-\infty}^{t_1} e^{-j\omega_L(t_1+t_2)}\langle \mathrm{G}|a_v e^{-jH^{(1)}(\tau_1-\tau_2)}a_w e^{-jH^{(2)}(\tau_2-t_1)}a_u^\dagger e^{-jH^{(1)}(t_1-t_2)}a_u^\dagger|\mathrm{G}\rangle dt_1 dt_2 \tag{B.19}$$

$$= \sum_{k_3,k_4,k_5}\langle \mathrm{G}|a_v|r_{k_3}^{(1)}\rangle\langle l_{k_3}^{(1)}|a_w|r_{k_4}^{(2)}\rangle\langle l_{k_4}^{(2}|a_u^\dagger|r_{k_5}^{(1)}\rangle\langle l_{k_5}^{(1)}|a_u^\dagger|\mathrm{G}\rangle e^{-jE_{k_3}^{(1)}(\tau_1-\tau_2)}I_{\tau_2,k_4,k_5} \tag{B.20}$$

where

$$I_{\tau_2,k_4,k_5} = \int_{t_1=-\infty}^{\tau_2}\int_{t_2=-\infty}^{t_1} e^{-jE_{k_4}^{(2)}(\tau_2-t_1)}e^{-jE_{k_5}^{(1)}(t_1-t_2)}e^{-j\omega_L(t_1+t_2)}dt_1 dt_2 \tag{B.21}$$

$$= \int_{t_1=-\infty}^{\tau_2}\left\{e^{-jE_{k_4}^{(2)}(\tau_2-t_1)}e^{-jE_{k_5}^{(1)}t_1}e^{-j\omega_L t_1}\int_{t_2=-\infty}^{t_1} e^{-jt_2(\omega_L-E_{k_5}^{(1)})}dt_2\right\}dt_1 \tag{B.22}$$

$$= \int_{t_1=-\infty}^{\tau_2} e^{-jE_{k_4}^{(2)}(\tau_2-t_1)}e^{-jE_{k_5}^{(1)}t_1}e^{-j\omega_L t_1}\frac{e^{-jt_1(\omega_L-E_{k_5}^{(1)})}}{j(E_{k_5}^{(1)}-\omega_L)}dt_1 \tag{B.23}$$

$$= \int_{t_1=-\infty}^{\tau_2}\frac{e^{-jt_1(2\omega_L-E_{k_4}^{(2)})}e^{-jE_{k_4}^{(2)}\tau_2}}{j(E_{k_5}^{(1)}-\omega_L)}dt_1 = -\frac{e^{-j\tau_2(2\omega_L-E_{k_4}^{(2)})}e^{-jE_{k_4}^{(2)}\tau_2}}{(E_{k_4}^{(2)}-2\omega_L)(E_{k_5}^{(1)}-\omega_L)} \tag{B.24}$$

which leads to

$$I_2 = -\sum_{k_3,k_4,k_5} \frac{\langle \mathrm{G}|a_v|r^{(1)}_{k_3}\rangle\langle l^{(1)}_{k_3}|a_w|r^{(2)}_{k_4}\rangle\langle l^{(2}_{k_4}|a^\dagger_u|r^{(1)}_{k_5}\rangle\langle l^{(1)}_{k_5}|a^\dagger_u|\mathrm{G}\rangle e^{-j\epsilon^{(1)}_{k_3}(\tau_1-\tau_2)}e^{-j2\omega_L\tau_2}}{(E^{(2)}_{k_4}-2\omega_L)(E^{(1)}_{k_5}-\omega_L)} \tag{B.25}$$

Now of particular interest to us is the case when $\tau_2 = 0, \tau_1 - \tau_2 = 0$. $F_{u,v,w}(0,\omega_L) = 2(0+I_2)$ as $I_1 = 0$ when $\tau_1 - \tau_2 = 0$. Hence $F_{u,v,w}(0,\omega_L)$ can be written as

$$F_{u,v,w}(0,\omega_L) = \sum_{k_3,k_4,k_5} \frac{\langle \mathrm{G}|a_v|r^{(1)}_{k_3}\rangle\langle l^{(1)}_{k_3}|a_w|r^{(2)}_{k_4}\rangle\langle l^{(2}_{k_4}|a^\dagger_u|r^{(1)}_{k_5}\rangle\langle l^{(1)}_{k_5}|a^\dagger_u|\mathrm{G}\rangle}{-0.5(E^{(2)}_{k_4}-2\omega)(E^{(1)}_{k_5}-\omega)} \tag{B.26}$$

Substituting the above in Eq. B.2 then allows us to obtain the second-order auto-correlation function $g^{(2)}_{v,u}(0,\omega)$ as

$$g^{(2)}_{v,u}(0,\omega) = \frac{\gamma_v\gamma_u}{4|T_{v,u}(\omega)|^4}\left|\sum_{\alpha_1,\alpha_2,\alpha_3} \frac{\langle \mathrm{G}|a_v|r^{(1)}_{\alpha_1}\rangle\langle l^{(1)}_{\alpha_1}|a_v|r^{(2)}_{\alpha_2}\rangle\langle l^{(2}_{\alpha_2}|a^\dagger_u|r^{(1)}_{\alpha_3}\rangle\langle l^{(1)}_{\alpha_3}|a^\dagger_u|\mathrm{G}\rangle}{-0.5(E^{(2)}_{\alpha_2}-2\omega)(E^{(1)}_{\alpha_3}-\omega)}\right|^2 \tag{B.27}$$

where we have substituted for the specific case of interest where $v = w$ and changed the counting coefficients to α_ss for sake of clarity.

Fitting for the spectrum then additionally allows determination of the eigenenergies of H within two-photon subspace, $E^{(2)}_\alpha$, as well as the coefficients:

$$M^{(2)}_{\vec{\alpha},v,u} = \langle G|a_v|r^{(1)}_{\alpha_1}\rangle\langle l^{(1)}_{\alpha_1}|a_v|r^{(2)}_{\alpha_2}\rangle\langle l^{(2)}_{\alpha_2}|a^\dagger_u|r^{(1)}_{\alpha_3}\rangle\langle l^{(1)}_{\alpha_3}|a^\dagger_u|G\rangle \;\forall\; u,v \in \mathcal{V}_0. \tag{B.28}$$

where $\vec{\alpha}$ denotes a list of coefficients $(\alpha_1,\alpha_2,\alpha_3)$. Note that we know already know the values of $E^{(1)}_{\alpha_3}$ and $\langle G|a_v|r^{(1)}_{\alpha_1}\rangle\langle l^{(1)}_{\alpha_3}|a^\dagger_u|G\rangle \;\forall\; \alpha_1,\alpha_3$ and $v,u \in \mathcal{V}_0$.

B.2 Algorithm

In this section, we look at the two-photon scattering tomography algorithm in depth. Experimentally measuring $g^{(2)}_{v,u}(0,\omega)$ allows us to uniquely determine $M^{(2)}_{\vec{\alpha},v,u}$ and $E^{(2)}_{\alpha_2} \;\forall\; \vec{\alpha} = (\alpha_1,\alpha_2,\alpha_3),\; v,u \in \mathcal{V}_0$. This implies we can obtain the operators $O^{(2)}_{\alpha_2,v,u}$ of the form

$a_v|r^{(2)}_{\alpha_2}\rangle\langle l^{(2)}_{\alpha_2}|a^\dagger_u$ as:

$$O^{(2)}_{\alpha_2,v,u} = \sum_{\alpha_1,\alpha_3} |r^{(1)}_{\alpha_1}\rangle_{rc}\langle l^{(1)}_{\alpha_3}|_{rc} \frac{M^{(2)}_{\vec{\alpha},v,u}}{\langle G|a_v|r^{(1)}_{\alpha_1}\rangle_{rc}\langle l^{(1)}_{\alpha_3}|a^\dagger_u|G\rangle_{rc}} \tag{B.29}$$

$$O^{(2)}_{\alpha_2,v,u} = \sum_{\alpha_1,\alpha_3} |r^{(1)}_{\alpha_1}\rangle_{rc}\langle l^{(1)}_{\alpha_3}|_{rc} \frac{\langle G|a_v|r^{(1)}_{\alpha_1}\rangle\langle l^{(1)}_{\alpha_1}|a_v|r^{(2)}_{\alpha_2}\rangle\langle l^{(2)}_{\alpha_2}|a^\dagger_u|r^{(1)}_{\alpha_3}\rangle\langle l^{(1)}_{\alpha_3}|a^\dagger_u|G\rangle}{\langle G|a_v|r^{(1)}_{\alpha_1}\rangle_{rc}\langle l^{(1)}_{\alpha_3}|a^\dagger_u|G\rangle_{rc}} \tag{B.30}$$

$$= \sum_{\alpha_1,\alpha_3} |r^{(1)}_{\alpha_1}\rangle_{rc}\langle l^{(1)}_{\alpha_3}|_{rc}\langle l^{(1)}_{\alpha_1}|a_v|r^{(2)}_{\alpha_2}\rangle\langle l^{(2)}_{\alpha_2}|a^\dagger_u|r^{(1)}_{\alpha_3}\rangle \frac{\langle G|a_v|l^{(1)}_{\alpha_1}\rangle\langle r^{(1)}_{\alpha_3}|a_u|G\rangle}{\langle G|a_v|r^{(1)}_{\alpha_1}\rangle_{rc}\langle l^{(1)}_{\alpha_3}|a^\dagger_u|G\rangle_{rc}} \tag{B.31}$$

$$= \sum_{\alpha_1,\alpha_3} |r^{(1)}_{\alpha_1}\rangle_{rc}\langle l^{(1)}_{\alpha_1}|a_v|r^{(2)}_{\alpha_2}\rangle\langle l^{(2)}_{\alpha_2}|a^\dagger_u|r^{(1)}_{\alpha_3}\rangle\langle l^{(1)}_{\alpha_3}|_{rc} \left(e^{i\theta_{rc}}_{\text{Phase correction}}\right) \tag{B.32}$$

$$= P^{(1)}a_v|r^{(2)}_{\alpha_2}\rangle_{rc}\langle l^{(2)}_{\alpha_2}|_{rc}a^\dagger_u P^{(1)} = a_v|r^{(2)}_{\alpha_2}\rangle_{rc}\langle l^{(2)}_{\alpha_2}|_{rc}a^\dagger_u \tag{B.33}$$

where the label "rc" is used to refer to the vectors in the reconstructed global basis obtained after running the linear part of the algorithm. This is different from the measurement basis of $M^{(2)}_{\vec{\alpha},v,u}$ and we need to do this transformation before proceeding further. From here on out we will exclusively work in this reconstructed global basis and will hence drop the labels "rc". Additionally, $P^{(1)}$ denotes the projector onto 1^{st} excitation subspace (reconstructed basis). The projectors onto the 1^{st} and 2^{nd} excitation subspaces can in general be written as

$$\sum_{\alpha_1} |r^{(1)}_{\alpha_1}\rangle\langle l^{(1)}_{\alpha_1}| = P^{(1)} = \sum_m a^\dagger_m|\mathrm{G}\rangle\langle \mathrm{G}|a_m \tag{B.34}$$

$$\sum_{\alpha_2} |r^{(2)}_{\alpha_2}\rangle\langle l^{(2)}_{\alpha_2}| = P^{(2)} = \frac{1}{2}\sum_{n,p} a^\dagger_n a^\dagger_p|\mathrm{G}\rangle\langle \mathrm{G}|a_n a_p \tag{B.35}$$

Note that as we already know the values of $|r^{(1)}_{\alpha_1}\rangle$, $\langle l^{(1)}_{\alpha_3}|\ \forall\ \alpha_1, \alpha_3$ the experimentally obtained operators can then be used to calculate coefficients of the form of: $\langle l^{(1)}_{\alpha_1}|a_v|r^{(2)}_{\alpha_2}\rangle\langle l^{(2)}_{\alpha_2}|a^\dagger_u|r^{(1)}_{\alpha_3}\rangle$, $\langle l^{(1)}_{\alpha_1}|(a^\dagger_v a_v)a_v|r^{(2)}_{\alpha_2}\rangle\langle l^{(2)}_{\alpha_2}|a^\dagger_u|r^{(1)}_{\alpha_3}\rangle$, $\langle l^{(1)}_{\alpha_2}|a_v|r^{(2)}_{\alpha_2}\rangle\langle l^{(2)}_{\alpha_2}|a^\dagger_u(a^\dagger_u a_u)|r^{(1)}_{\alpha_3}\rangle\ \forall\ \alpha_1, \alpha_2, \alpha_3$.

Before going forward let's evaluate two more quantities that will be of used later on:

$$\sum_{\alpha_1,\alpha_2} \langle l^{(1)}_{\alpha_1}|a_p|r^{(2)}_{\alpha_2}\rangle\langle l^{(2)}_{\alpha_2}|a^\dagger_m|r^{(1)}_{\alpha_1}\rangle = \sum_{\alpha_1,\alpha_2} Tr\left(|r^{(1)}_{\alpha_1}\rangle\langle l^{(1)}_{\alpha_1}|a_p|r^{(2)}_{\alpha_2}\rangle\langle l^{(2)}_{\alpha_2}|a^\dagger_m\right) \tag{B.36}$$

$$= Tr\left(\sum_{\alpha_1,\alpha_2} |r^{(1)}_{\alpha_1}\rangle\langle l^{(1)}_{\alpha_1}|a_p|r^{(2)}_{\alpha_2}\rangle\langle l^{(2)}_{\alpha_2}|a^\dagger_m\right) = Tr\left(P^{(1)}a_pP^{(2)}a^\dagger_m\right) \tag{B.37}$$

$$= Tr\left(\sum_{\alpha} a^\dagger_\alpha|G\rangle\langle G|a_\alpha a_p\frac{1}{2}\sum_{\beta,\gamma} a^\dagger_\beta a^\dagger_\gamma|G\rangle\langle G|a_\beta a_\gamma a^\dagger_m\right) \tag{B.38}$$

$$= \frac{1}{2}Tr\left(\sum_{\alpha,\beta,\gamma} a^\dagger_\alpha|G\rangle\langle G|a_\alpha a_p a^\dagger_\beta a^\dagger_\gamma|G\rangle\langle G|a_\beta a_\gamma a^\dagger_m\right) \tag{B.39}$$

$$= \frac{1}{2}\sum_{\alpha,\beta,\gamma} Tr\left(a^\dagger_\alpha|G\rangle\langle G|a_\alpha a_p a^\dagger_\beta a^\dagger_\gamma|G\rangle\langle G|a_\beta a_\gamma a^\dagger_m\right) \tag{B.40}$$

$$= \frac{1}{2}\sum_{\alpha,\beta,\gamma}\langle G|a_\beta a_\gamma a^\dagger_m a^\dagger_\alpha|G\rangle\langle G|a_\alpha a_p a^\dagger_\beta a^\dagger_\gamma|G\rangle = \delta_{pm}(N^2+N) \tag{B.41}$$

for any p, m in the graph $\mathcal{G}$. Note that we used the fact that $\langle w_1|w_2\rangle = Tr(|w_2\rangle\langle w_1|)$. And secondly,

$$\sum_{\alpha_1,\alpha_2}\langle l^{(1)}_{\alpha_1}|a^\dagger_p a^2_p|r^{(2)}_{\alpha_2}\rangle\langle l^{(2)}_{\alpha_2}|a^\dagger_p|r^{(1)}_{\alpha_1}\rangle = \sum_{\alpha_1,\alpha_2} Tr\left(|r^{(1)}_{\alpha_1}\rangle\langle l^{(1)}_{\alpha_1}|a^\dagger_p a^2_p|r^{(2)}_{\alpha_2}\rangle\langle l^{(2)}_{\alpha_2}|a^\dagger_p\right) \tag{B.42}$$

$$= Tr\left(\sum_{\alpha_1,\alpha_2} |r^{(1)}_{\alpha_1}\rangle\langle l^{(1)}_{\alpha_1}|a^\dagger_p a^2_p|r^{(2)}_{\alpha_2}\rangle\langle l^{(2)}_{\alpha_2}|a^\dagger_p\right) = Tr\left(P^{(1)}a^\dagger_p a^2_p P^{(2)}a^\dagger_p\right) \tag{B.43}$$

$$= Tr\left(\sum_{\alpha} a^\dagger_\alpha|G\rangle\langle G|a_\alpha a^\dagger_p a^2_p\frac{1}{2}\sum_{\beta,\gamma} a^\dagger_\beta a^\dagger_\gamma|G\rangle\langle G|a_\beta a_\gamma a^\dagger_p\right) \tag{B.44}$$

$$= \frac{1}{2}Tr\left(\sum_{\alpha,\beta,\gamma} a^\dagger_\alpha|G\rangle\langle G|a_\alpha a^\dagger_p a^2_p a^\dagger_\beta a^\dagger_\gamma|G\rangle\langle G|a_\beta a_\gamma a^\dagger_p\right) \tag{B.45}$$

$$= \frac{1}{2}\sum_{\alpha,\beta,\gamma} Tr\left(a^\dagger_\alpha|G\rangle\langle G|a_\alpha a^\dagger_p a^2_p a^\dagger_\beta a^\dagger_\gamma|G\rangle\langle G|a_\beta a_\gamma a^\dagger_p\right) \tag{B.46}$$

$$= \frac{1}{2}\sum_{\alpha,\beta,\gamma}\langle G|a_\beta a_\gamma a^\dagger_p a^\dagger_\alpha|G\rangle\langle G|a_\alpha a^\dagger_p a^2_p a^\dagger_\beta a^\dagger_\gamma|G\rangle = 2 \tag{B.47}$$

Now for $v \in \mathcal{V}_0$ we can write:

$$a_v H|r^{(2)}_{\alpha_2}\rangle = E^{(2)}_{\alpha_2}a_v|r^{(2)}_{\alpha_2}\rangle \implies \langle l^{(1)}_{\alpha_1}|a_v H|r^{(2)}_{\alpha_2}\rangle = E^{(2)}_{\alpha_2}\langle l^{(1)}_{\alpha_1}|a_v|r^{(2)}_{\alpha_2}\rangle \tag{B.48}$$

Using the commutator relation of a_v, H gives

$$\langle l^{(1)}_{\alpha_1}|a_v H|r^{(2)}_{\alpha_2}\rangle = \langle l^{(1)}_{\alpha_1}|[a_v, H] + Ha_v|r^{(2)}_{\alpha_2}\rangle \tag{B.49}$$

$$\implies \langle l^{(1)}_{\alpha_1}|[a_v, H]|r^{(2)}_{\alpha_2}\rangle + E^{(1)}_{\alpha_1}\langle l^{(1)}_{\alpha_1}|a_v|r^{(2)}_{\alpha_2}\rangle = E^{(2)}_{\alpha_2}\langle l^{(1)}_{\alpha_1}|a_v|r^{(2)}_{\alpha_2}\rangle \tag{B.50}$$

Evaluating the commutator $[a_v, H]$:

$$[a_v, H] = [a_v, \sum_n \mu_n(a^\dagger_n a_n) + \frac{\chi_n}{2}a^{\dagger 2}_n a^2_n + \sum_{n,m} J_{m,n}(a^\dagger_m a_n)] = 0 \text{ when } m|n \neq v. \tag{B.51}$$

Hence,

$$[a_v, H] = [a_v, \mu_v a^\dagger_v a_v + \frac{\chi_v}{2}a^{\dagger 2}_v a^2_v + \sum_{n|m=v} J_{m,n}a^\dagger_m a_n] \tag{B.52}$$

Using the following commutator properties,

$$[a_v, a_p a^\dagger_v] = [a_v, a_p]a^\dagger_v + a_p[a_v, a^\dagger_v] = a_p \ \forall\ p \neq v. \tag{B.53}$$

$$[a_v, a_v a^\dagger_p] = [a_v, a_v]a^\dagger_p + a_v[a_v, a^\dagger_p] = 0 \ \forall\ p \neq v. \tag{B.54}$$

$$[a_v, a^\dagger_v a_v] = [a_v, a^\dagger_v]a_v + a^\dagger_v[a_v, a_v] = a_v. \tag{B.55}$$

$$\begin{aligned}[a_v, a^{\dagger 2}_v a^2_v] &= a_v a^{\dagger 2}_v a^2_v - a^{\dagger 2}_v a^3_v \\ &= [a_v a^{\dagger 2}_v - a^{\dagger 2}_v a_v]a^2_v = [a_v, a^{\dagger 2}_v]a^2_v \\ &= ([a_v, a^\dagger_v]a_v + a_v[a_v, a^\dagger_v])a^2_v = 2a^\dagger_v a^2_v.\end{aligned} \tag{B.56}$$

We obtain,

$$[a_v, H] = \mu_v a_v + \chi_v a^\dagger_v a^2_v + \sum_{u\in N_v} J_{v,u}a_u \tag{B.57}$$

Substituting into Eq. B.50 we have

$$J_{v,u}\sum_{u\in N_v}\langle l^{(1)}_{\alpha_1}|a_u|r^{(2)}_{\alpha_2}\rangle + \chi_v\langle l^{(1)}_{\alpha_1}|a^\dagger_v a^2_v|r^{(2)}_{\alpha_2}\rangle + (\mu_v + E^{(1)}_{\alpha_1} - E^{(2)}_{\alpha_2})\langle l^{(1)}_{\alpha_1}|a_v|r^{(2)}_{\alpha_2}\rangle = 0 \tag{B.58}$$

Similarly we can write the dual of the above set of equations as:

$$\langle l^{(2)}_{\alpha_2}|Ha^\dagger_v = E^{(2)}_{\alpha_2}\langle l^{(2)}_{\alpha_2}|a^\dagger_v \implies \langle l^{(2)}_{\alpha_2}|Ha^\dagger_v|r^{(1)}_{\alpha_3}\rangle = E^{(2)}_{\alpha_2}\langle l^{(2)}_{\alpha_2}|a^\dagger_v|r^{(1)}_{\alpha_3}\rangle \tag{B.59}$$

Using the commutator relation of $H, a^\dagger_v$ gives

$$\langle l^{(2)}_{\alpha_2}|Ha^\dagger_v|r^{(1)}_{\alpha_3}\rangle = \langle l^{(2)}_{\alpha_2}|[H, a^\dagger_v] + a^\dagger_v H|r^{(1)}_{\alpha_3}\rangle \tag{B.60}$$

$$\implies \langle l^{(2)}_{\alpha_2}|[H,a^\dagger_v]|r^{(1)}_{\alpha_3}\rangle + E^{(1)}_{\alpha_3}\langle l^{(2)}_{\alpha_2}|a^\dagger_v|r^{(1)}_{\alpha_3}\rangle = E^{(2)}_{\alpha_2}\langle l^{(2)}_{\alpha_2}|a^\dagger_v|r^{(1)}_{\alpha_1}\rangle \tag{B.61}$$

Evaluating the commutator $[H,a^\dagger_v]$:

$$[H,a^\dagger_v] = [\sum_n \mu_n(a^\dagger_n a_n) + \frac{\chi_n}{2}a^{\dagger 2}_n a^2_n + \sum_{n,m} J_{m,n}(a^\dagger_m a_n), a^\dagger_v] = 0 \text{ when } m|n \neq v. \tag{B.62}$$

Hence,

$$[H,a^\dagger_v] = [\mu_v a^\dagger_v a_v + \frac{\chi_v}{2}a^{\dagger 2}_v a^2_v + \sum_{n|m=v} J_{m,n}a^\dagger_m a_n, a^\dagger_v] \tag{B.63}$$

Also,

$$[a_p a^\dagger_v, a^\dagger_v] = a_p[a^\dagger_v, a^\dagger_v] + [a_p, a^\dagger_v]a^\dagger_v = 0 \;\forall\; p \neq v. \tag{B.64}$$

$$[a_v a^\dagger_p, a^\dagger_v] = a_v[a^\dagger_p, a^\dagger_v] + [a_v, a^\dagger_v]a^\dagger_p = a^\dagger_p \;\forall\; p \neq v. \tag{B.65}$$

$$[a^\dagger_v a_v, a^\dagger_v] = a^\dagger_v[a_v, a^\dagger_v] + [a^\dagger_v, a^\dagger_v]a_v = a^\dagger_v. \tag{B.66}$$

$$\begin{aligned}[a^{\dagger 2}_v a^2_v, a^\dagger_v] &= a^{\dagger 2}_v a^2_v a^\dagger_v - a^{\dagger 3}_v a^2_v = a^{\dagger 2}_v[a^2_v a^\dagger_v - a^\dagger_v a^2_v] = a^{\dagger 2}_v[a^2_v, a^\dagger_v] \\ &= a^\dagger_v([a_v, a^\dagger_v]a_v + a^\dagger_v[a_v, a^\dagger_v]) = 2a^{\dagger 2}_v a_v.\end{aligned} \tag{B.67}$$

Giving,

$$[H,a^\dagger_v] = \mu_v a^\dagger_v + \chi_v a^{\dagger 2}_v a_v + \sum_{u\in N_v} J_{u,v}a^\dagger_u \tag{B.68}$$

Substituting into Eq. B.61 we have

$$J_{u,v}\sum_{u\in N_v}\langle l^{(2)}_{\alpha_2}|a^\dagger_u|r^{(1)}_{\alpha_3}\rangle + \chi_v\langle l^{(2)}_{\alpha_2}|a^{\dagger 2}_v a_v|r^{(1)}_{\alpha_3}\rangle + (\mu_v + E^{(1)}_{\alpha_3} - E^{(2)}_{\alpha_2})\langle l^{(2)}_{\alpha_2}|a^\dagger_v|r^{(1)}_{\alpha_3}\rangle = 0 \tag{B.69}$$

We now define the coefficients $C^{(2)}_{\vec{\alpha},m,n} = \langle l^{(1)}_{\alpha_1}|O^{(2)}_{\alpha_2,m,n}|r^{(1)}_{\alpha_3}\rangle = \langle l^{(1)}_{\alpha_1}|a_m|r^{(2)}_{\alpha_2}\rangle\langle l^{(2)}_{\alpha_2}|a^\dagger_n|r^{(1)}_{\alpha_3}\rangle$.
To find χ_v we multiply Eq. B.58 by $\langle l^{(2)}_{\alpha_2}|a^\dagger_v|r^{(1)}_{\alpha_1}\rangle$ and sum over α_1, α_2 to get:

$$0 + 2\chi_v + \sum_{\alpha_1,\alpha_2}(\mu_v + E^{(1)}_{\alpha_2} - E^{(2)}_{\alpha_2})C^{(2)}_{\vec{\alpha},v,v} = 0 \text{ s.t. } \alpha_1 = \alpha_3 \tag{B.70}$$

$$\implies \chi_v = -\frac{1}{2}\sum_{\alpha_1,\alpha_2}(\mu_v + E^{(1)}_{\alpha_1} - E^{(2)}_{\alpha_2})C^{(2)}_{\vec{\alpha},v,v} \text{ s.t. } \alpha_1 = \alpha_3 \tag{B.71}$$

Note, that if we know the value of coefficients $C^{(2)}_{\vec{\alpha},m,n}$ at any point we can revert back to operators $O^{(2)}_{\alpha_2,m,n}$ at any time using the relations:

$$\sum_{\alpha_1,\alpha_3} |r^{(1)}_{\alpha_1}\rangle\langle l^{(1)}_{\alpha_1}|a_m|r^{(2)}_{\alpha_2}\rangle\langle l^{(2)}_{\alpha_2}|a^\dagger_n|r^{(1)}_{\alpha_3}\rangle\langle l^{(1)}_{\alpha_3}| = P^{(1)}a_m|r^{(2)}_{\alpha_2}\rangle\langle l^{(2)}_{\alpha_2}|a^\dagger_n P^{(1)} = O^{(2)}_{\alpha_2,m,n} \tag{B.72}$$

and consequently also calculate the coefficients $\langle l^{(1)}_{\alpha_1}|(a^\dagger_m a_m)a_m|r^{(2)}_{\alpha_2}\rangle\langle l^{(2)}_{\alpha_2}|a^\dagger_n|r^{(1)}_{\alpha_3}\rangle$, $\langle l^{(1)}_{\alpha_1}|a_m|r^{(2)}_{\alpha_2}\rangle\langle l^{(2)}_{\alpha_2}|a^\dagger_n(a^\dagger_n a_n)|r^{(1)}_{\alpha_3}\rangle$ which we will denote by $Q^{(2)}_{\vec{\alpha},m,n}, R_{\vec{\alpha},m,n}$ respectively going forward.

Now multiplying B.58 by $\langle l^{(2)}_{\alpha_2}|a^\dagger_v|r^{(1)}_{\alpha_1}\rangle$ and rearranging terms gives:

$$C_{\vec{\alpha},v',v} = -\frac{1}{J_{v,v'}}\left(\sum_{u\in N_v - v'} J_{v,u}C_{\vec{\alpha},u,v} + \chi_v Q_{\vec{\alpha},v,v} + (\mu_v + E^{(1)}_{\alpha_1} - E^{(2)}_{\alpha_2})C_{\vec{\alpha},v,v}\right) \tag{B.73}$$

where $v' \in \mathcal{V}_1$. Next multiplying B.58 by $\langle l^{(2)}_{\alpha_2}|a^\dagger_{u_1}|r^{(1)}_{\alpha_3}\rangle$ where $u_1 \in u$ and rearranging terms gives:

$$C_{\vec{\alpha},v',u_1} = -\frac{1}{J_{v,v'}}\left(\sum_{u\in N_v - v'} J_{v,u}C_{\vec{\alpha},u,u_1} + \chi_v Q_{\vec{\alpha},v,u_1} + (\mu_v + E^{(1)}_{\alpha_1} - E^{(2)}_{\alpha_2})C_{\vec{\alpha},v,u_1}\right) \tag{B.74}$$

For the duals, we multiply Eq. B.69 by $\langle l^{(1)}_{\alpha_1}|a_v|r^{(2)}_{\alpha_2}\rangle$ and rearranging the terms gives:

$$C_{\vec{\alpha},v,v'} = -\frac{1}{J^*_{v,v'}}\left(\sum_{u\in N_v - v'} J^*_{v,u}C_{\vec{\alpha},v,u} + \chi_v R_{\vec{\alpha},v,v} + (\mu_v + E^{(1)}_{\alpha_3} - E^{(2)}_{\alpha_2})C_{\vec{\alpha},v,v}\right) \tag{B.75}$$

And then multiplying Eq. B.69 by $\langle l^{(1)}_{x}|a_{u_1}|r^{(2)}_{y}\rangle$ and rearranging terms gives:

$$C_{\vec{\alpha},u_1,v'} = -\frac{1}{J^*_{v,v'}}\left(\sum_{u\in N_v - v'} J^*_{v,u}C_{\vec{\alpha},u_1,u} + \chi_v R_{\vec{\alpha},u_1,v} + (\mu_v + E^{(1)}_{\alpha_3} - E^{(2)}_{\alpha_2})C_{\vec{\alpha},u_1,v}\right) \tag{B.76}$$

Now to set up the recursion in the algorithm we first calculate $C_{\vec{\alpha},v',v'}$ by multiplying Eq. B.58 by $\langle l^{(2)}_{\alpha_2}|a^\dagger_{v'}|r^{(1)}_{\alpha_3}\rangle$ and rearranging terms to get

$$C_{\vec{\alpha},v',v'} = -\frac{1}{J_{v,v'}}\left(\sum_{u\in N_v - v'} J_{v,u}C_{\vec{\alpha},u,v'} + \chi_v Q_{\vec{\alpha},v,v'} + (\mu_v + E^{(1)}_{\alpha_1} - E^{(2)}_{\alpha_2})C_{\vec{\alpha},v,v'}\right) \tag{B.77}$$

where we used values obtained in Eqs. B.75, B.76. To complete the recursion now we need to find $C_{\vec{\alpha},v',u'}, C_{\vec{\alpha},u',v'}, C_{\vec{\alpha},u'_1,u'_2}$ where $u' \in N_{v'} - v'' = v \cup (N_{v'} \cap \mathcal{V}_1)$. First for $C_{\vec{\alpha},v',u'}$, we

know that:

$$\begin{aligned} C_{\vec{\alpha},v',v}C_{\vec{\alpha},v,u}C_{\vec{\alpha},u,u'} &= \langle l^{(1)}_{\alpha_1}|a_{v'}|r^{(2)}_{\alpha_2}\rangle\langle l^{(2)}_{\alpha_2}|a^\dagger_{v}|r^{(1)}_{\alpha_3}\rangle \\ &\quad \langle l^{(1)}_{\alpha_1}|a_{v}|r^{(2)}_{\alpha_2}\rangle\langle l^{(2)}_{\alpha_2}|a^\dagger_{u}|r^{(1)}_{\alpha_3}\rangle \\ &\quad \langle l^{(1)}_{\alpha_1}|a_{u}|r^{(2)}_{\alpha_2}\rangle\langle l^{(2)}_{\alpha_2}|a^\dagger_{u'}|r^{(1)}_{\alpha_3}\rangle \qquad \text{(B.78)} \\ \implies C_{\vec{\alpha},v',v}C_{\vec{\alpha},v,u}C_{\vec{\alpha},u,u'} &= \langle l^{(1)}_{\alpha_1}|a_{v'}|r^{(2)}_{\alpha_2}\rangle\langle l^{(2)}_{\alpha_2}|a^\dagger_{u'}|r^{(1)}_{\alpha_3}\rangle \\ &\quad \langle l^{(1)}_{\alpha_1}|a_{v}|r^{(2)}_{\alpha_2}\rangle\langle l^{(2)}_{\alpha_2}|a^\dagger_{v}|r^{(1)}_{\alpha_1}\rangle \\ &\quad \langle l^{(1)}_{\alpha_1}|a_{u}|r^{(2)}_{\alpha_2}\rangle\langle l^{(2)}_{\alpha_2}|a^\dagger_{u}|r^{(1)}_{\alpha_1}\rangle \qquad \text{(B.79)} \\ \implies C_{\vec{\alpha},v',v}C_{\vec{\alpha},v,u}C_{\vec{\alpha},u,u'} &= \langle l^{(1)}_{\alpha_1}|a_{v'}|r^{(2)}_{\alpha_2}\rangle\langle l^{(2)}_{\alpha_2}|a^\dagger_{u'}|r^{(1)}_{\alpha_3}\rangle C_{\vec{\alpha},v,v}C_{\vec{\alpha},u,u} \qquad \text{(B.80)} \\ \implies C_{\vec{\alpha},v',u'} &= \frac{C_{\vec{\alpha},v',v}C_{\vec{\alpha},v,u}C_{\vec{\alpha},u,u'}}{C_{\vec{\alpha},v,v}C_{\vec{\alpha},u,u}} \qquad \text{(B.81)} \end{aligned}$$

Similarly $C_{\vec{\alpha},u',v'}$ can be written as:

$$C_{\vec{\alpha},u',v'} = \frac{C_{\vec{\alpha},u',u}C_{\vec{\alpha},u,v}C_{\vec{\alpha},v,v'}}{C_{\vec{\alpha},u,u}C_{\vec{\alpha},v,v}} \qquad \text{(B.82)}$$

Finally for $C_{\vec{\alpha},u'_1,u'_2}$:

$$\begin{aligned} C_{\vec{\alpha},u'_1,v'}C_{\vec{\alpha},v',u'_2} &= \langle l^{(1)}_{\alpha_1}|a_{u'_1}|r^{(2)}_{\alpha_2}\rangle\langle l^{(2)}_{\alpha_2}|a^\dagger_{v'}|r^{(1)}_{\alpha_3}\rangle \\ &\quad \langle l^{(1)}_{\alpha_1}|a_{v'}|r^{(2)}_{\alpha_2}\rangle\langle l^{(2)}_{\alpha_2}|a^\dagger_{u'_2}|r^{(1)}_{\alpha_1}\rangle \qquad \text{(B.83)} \\ \implies C_{\vec{\alpha},u'_1,v'}C_{\vec{\alpha},v',u'_2} &= \langle l^{(1)}_{\alpha_1}|a_{u'_1}|r^{(2)}_{\alpha_2}\rangle\langle l^{(2)}_{\alpha_2}|a^\dagger_{u'_2}|r^{(1)}_{\alpha_3}\rangle \\ &\quad \langle l^{(1)}_{\alpha_1}|a_{v'}|r^{(2)}_{\alpha_2}\rangle\langle l^{(2)}_{\alpha_2}|a^\dagger_{v'}|r^{(1)}_{\alpha_1}\rangle \qquad \text{(B.84)} \\ \implies C_{\vec{\alpha},u'_1,v'}C_{\vec{\alpha},v',u'_2} &= \langle l^{(1)}_{\alpha_1}|a_{u'_1}|r^{(2)}_{\alpha_2}\rangle\langle l^{(2)}_{\alpha_2}|a^\dagger_{u'_2}|r^{(1)}_{\alpha_3}\rangle C_{\vec{\alpha},v',v'} \qquad \text{(B.85)} \\ \implies C_{\vec{\alpha},u'_1,u'_2} &= \frac{C_{\vec{\alpha},u'_1,v'}C_{\vec{\alpha},v',u'_2}}{C_{\vec{\alpha},v',v'}} \qquad \text{(B.86)} \end{aligned}$$

We can then repeat this process repeatedly until we have covered all the perimeters $\mathcal{V}_0 \cup \mathcal{V}_1 \cup \mathcal{V}_2 \cup \ldots = \mathcal{V}$ forming the graph $(\mathcal{V}, \mathcal{E})$ describing the photonic lattice. At the end of the algorithm we have now completely determined $H^{(0)} + H^{(1)} + H^{(2)}$.

B.3 Stability analysis

We define an error metric to study how the non-linear algorithm behaves in presence of measurement error in $C^{(2)}_{\vec{\alpha}}$:

$$\text{Error metric} = \log_{10}\left(\sum_{\vec{\alpha},v',u'}\left|\frac{\partial\chi_v}{\partial C^{(2)}_{\vec{\alpha},v',u'}}\right|^2\right) \tag{B.87}$$

where we have assumed that $\langle \delta C^{(2)}_{\vec{\alpha},v'_1,u'_1}\delta C^{(2)}_{\vec{\alpha},v'_2,u'_2}\rangle = 0$. This assumption again holds as we are dealing with errors at different frequencies. If the algorithm is stable with increasing number of sites N then the defined error metrics as in Ch. 4 should scale as $a + b\log(N)$ as this would imply a polynomial scaling in the number of measurements needed to attain a specific precision. We again use the SSH model to study the stability of algorithm in Fig. B.1.

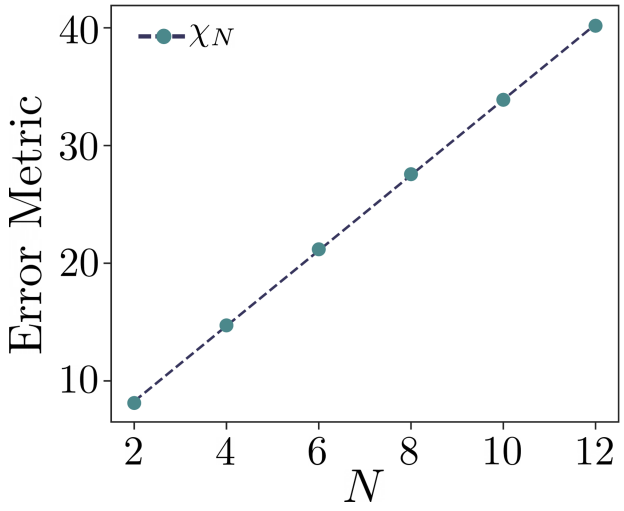

Figure B.1: Stability analysis where x-axis denotes number of sites in the array on a linear scale and y-axis denotes the error metric in χ_N for a SSH chain with $J_1/J_2 = 1.2$. Error metric scales linearly with N. The slope of the straight line fit $a' + b'N$ is $b' = 3.20$.

We notice that it scales linearly with N which implies that reconstructing the non-linear part of the Hamiltonian requires exponentially number of measurements as the number of sites N

increases. This indicates that this algorithm despite being applicable for lossy lattices with complex hopping rates is only practical when the size of the photonic lattice (characterized by N) is small.

Appendix C

QUANTUM ENHANCED TOMOGRAPHY

In Appendix B, the algorithm for obtaining the χs using $g^{(2)}$ measurements was found to be unstable. In this section, we will demonstrate that if we have the capability to control the non-linearity, enabling us to turn it on and off at will, there exists a protocol that overcomes this instability. The proposed protocol requires the initialization of a Fock state at the desired site to measure the non-linearity. While, initially, it might appear that accessing all sites of the lattice is necessary for this task, we can overcome this limitation even if we only have access to the boundary sites. The approach involves initializing P photons at the desired site by reversing the decay of photons to the output port and determining the required input wave packet by using the measured linear Hamiltonian. It is important to note that the non-linear terms are inactive during this process. Consequently, the input wave packet can be obtained using classical computation within polynomial time complexity ($poly(N)$). Furthermore, we can derive an upper bound on the error associated with initializing P photons at any lattice site, considering deviations from the true values of the linear coefficients in the Hamiltonian. Let's consider the precision ϵ_0 of the parameters $J_{u,v}$ and μ_u in the linear Hamiltonian $H^{(1)}$. We denote the measured linear Hamiltonian as $H_{rc}^{(1)}$. Suppose the computed input wavefunction is $|\psi_{\text{in}}\rangle$, and after a propagation time t_{prop}, the evolved wavefunction at site u^* (the site where we want to measure χ) is $|P\rangle$:

$$e^{-jH_{rc}^{(1)}t_{\text{prop}}}|\psi_{\text{in}}\rangle = \left|\psi_p'(t_{\text{prop}})\right\rangle = |P\rangle$$

However, the actual wavefunction results from the following equation using the real Hamiltonian:

$$e^{-iH^{(1)}t_{\text{prop}}}|\psi_{\text{in}}\rangle = |\psi_p(t_{\text{prop}})\rangle$$

Lemma 1 *For a photonic graph with N sites, and degree d, it is possible to initialize a P-photon Fock state at any site with a precision of ϵ_1 as follows:*

$$\| |P\rangle - |\psi_p\rangle \| \leq \epsilon_1 \quad , \quad \epsilon_1 = \sqrt{t_{prop} P N (d+1) \epsilon_0}$$

Proof: We can quantify the distance between $|\psi_P\rangle$ and $|P\rangle$ as:

$$\| |P\rangle - |\psi_p\rangle \|^2 = 2\,\mathrm{Re}(1 - \langle \psi_p | P \rangle)$$

using the derivative of $\langle \psi_P | P \rangle$ with respect to time,

$$\frac{\mathrm{d}\,\langle \psi_p | P \rangle}{\mathrm{d}s} = \frac{\mathrm{d}\,\langle \psi_{\mathrm{in}}|\, e^{jH_{rc}^{(1)}s} e^{-jH^{(1)}s}\, |\psi_{\mathrm{in}}\rangle}{\mathrm{d}s} = j\,\langle \psi_p(s)|\, H_{rc}^{(1)} - H^{(1)}\, |P(s)\rangle$$

Therefore,

$$\| |P\rangle - |\psi_p\rangle \|^2 \leq 2 \int_0^{t_{\mathrm{prop}}} \left| \langle \psi_p(s)|\, H_{rc}^{(1)} - H^{(1)}\, |P(s)\rangle \right| \mathrm{d}s$$

We can express the term in the integral as:

$$\begin{aligned} \langle \psi_p(s)|\, H_{rc}^{(1)} - H^{(1)}\, |P(s)\rangle &= \sum_{u,v \in \mathcal{E}} \delta J_{u,v}\, \langle \psi_p(s)|\, a_u^\dagger a_v\, |P(s)\rangle + \sum_u \delta\mu_u\, \langle \psi_p(s)|\, a_u^\dagger a_u\, |P(s)\rangle \\ &\leq 2\epsilon_0 \sum_{u,v \in \mathcal{E}} \left| \langle \psi_p(s)|\, a_u^\dagger a_v r\, |P(s)\rangle \right| + \epsilon_0 \sum_u \langle \psi_p(s)|\, a_u^\dagger a_u\, |P(s)\rangle \end{aligned}$$

Since $|P(s)\rangle$, and $|\psi_p(s)\rangle$ are P photon states,

$$\left| \langle \psi_p(s)|\, a_u^\dagger a_v\, |P(s)\rangle \right|^2 \leq \left| \langle \psi_p(s)|\, a_u^\dagger a_u\, |\psi_p(s)\rangle \right| \left| \langle P(s)|\, a_v^\dagger a_v\, |P(s)\rangle \right| \leq P^2$$

By substituting this into the integral:

$$\| |P\rangle - |\psi_p\rangle \|^2 \leq t_{\mathrm{prop}} P N (d+1) \epsilon_0$$

Now if we assume that ϵ_0 is $\mathrm{poly}(N, 1/P_L)$, with P_L the number of photons used to measure the linear part of the Hamiltonian, we can conclude that we need $\mathrm{poly}(N, 1/\epsilon_1)$ number of photons to obtain precision of ϵ_1.

After preparing the state $|P\rangle$, the non-linearity is activated for a duration of T_{on}. This time period should be sufficiently long to allow for the measurable accumulation of the phase induced by the non-linearity. However, it should also be short enough to prevent the P photons from diffusing to neighboring sites. To quantify the latter condition, let H be the full Hamiltonian that includes onsite anharmonicities, linear onsite terms, and coupling terms. We can define H_χ as the same Hamiltonian H without the coupling terms, that is:

$$H - H_\chi = \sum_{v,u \in \mathcal{E}} J_{v,u} a_v^\dagger a_u$$

In order to measure χ_u at site $u \in \mathcal{V}$, consider the initial wavefunction $\frac{1}{\sqrt{2}}(|P\rangle + |0\rangle)$. The evolved wavefunction at time T_{on} can be expressed as $\frac{1}{\sqrt{2}}(|\psi_\chi(T_{\text{on}})\rangle + |0\rangle)$, where:

$$|\psi_\chi(T_{\text{on}})\rangle = e^{-jH_\chi T_{\text{on}}} |P\rangle = e^{-j(\mu_u P + \chi_u \frac{P(P-1)}{2})T_{\text{on}}} |P\rangle$$

Since there are no coupling terms in H_χ, all P photons remain at site u and the evolved wavefunction simply acquires a phase. When the system evolves under the full Hamiltonian H, the wavefunction at time T_{on} is $\frac{1}{\sqrt{2}}(|\psi(T_{\text{on}})\rangle + |0\rangle)$, where:

$$|\psi(T_{\text{on}})\rangle = e^{-jHT_{\text{on}}} |P\rangle$$

Lemma 2 *The distance between $|\psi(T_{on})\rangle$ and $|\psi_\chi(T_{on})\rangle$ is bounded as:*

$$\| |\psi(T_{on})\rangle - |\psi_\chi(T_{on})\rangle \| \leq \epsilon_2 \quad , \quad \epsilon_2 = \sqrt{2P} J d T_{on}$$

Proof: Using the same technique as the previous lemma, we can write :

$$\begin{aligned}
\implies \| |\psi(T_{\text{on}})\rangle - |\psi_\chi(T_{\text{on}})\rangle \|^2 &\leq 2 \int_0^{T_{\text{on}}} \sum_{v,v'} |J_{v',v}| \Big(\Big| \langle \psi_\chi(s)| \, a_{v'}^\dagger a_v \, |\psi(s)\rangle \Big| \Big) \, \mathrm{d}s \\
&= 2 \int_0^{T_{\text{on}}} \sum_{v',v} |J_{v',v}| \Big(\Big| \langle P| \, a_{v'}^\dagger a_v \, |\psi(s)\rangle \Big| \Big) \, \mathrm{d}s \\
&= 2 \int_0^{T_{\text{on}}} \sum_{v \in \mathcal{N}_u} |J_{u,v}| \sqrt{P} \, |\langle P-1| \, a_v \, |\psi(s)\rangle| \, \mathrm{d}s \\
&\leq 2 \int_0^{T_{\text{on}}} \sum_{v \in \mathcal{N}_u} J \sqrt{P} \sqrt{\langle \psi(s)| \, a_v^\dagger a_v \, |\psi(s)\rangle} \, \mathrm{d}s
\end{aligned}$$

For the first equality we use the fact that without the coupling terms in the Hamiltonian, the evolved wavefunction is just a phase applied on the state $|P\rangle$. $\langle P| \, a_{v'}^\dagger$ is zero unless $v' = u$, therefore in the second equality, we just keep the terms that are neighbors of u, $v \in \mathcal{N}_u$. For the last inequality we use the Cauchy–Schwarz inequality, and we consider J to be the maximum value of $J_{u,v}$ over u, v.

$$\implies \| |\psi(T_{\text{on}})\rangle - |\psi_\chi(T_{\text{on}})\rangle \|^2 \leq 2J\sqrt{P} \int_0^{T_{\text{on}}} \sum_{v \in \mathcal{N}_u} \sqrt{N_v(s)} \, \mathrm{d}s \tag{C.1}$$

The number operator at site v is defined as:

$$\hat{N}_v = a_v^\dagger a_v \quad , \quad N_v(s) = \langle \psi(s)| \, a_v^\dagger a_v \, |\psi(s)\rangle$$

To find the upper bound on the number of photons at site v, we solve the differential equation for the operator $\hat{N}_v$ in the Heisenberg picture:

$$\frac{\mathrm{d}\hat{N}_v}{\mathrm{d}s} = -j[\hat{N}_v, H] = j \sum_{u \in \mathcal{N}_v} (J_{v,u} a_v^\dagger a_u + J_{u,v} a_u^\dagger a_v)$$

Therefore the upper bound for the derivative of number operator expectation is obtained as following:

$$\begin{aligned}
\implies \frac{\mathrm{d} \langle \psi| \, \hat{N}_v \, |\psi\rangle}{\mathrm{d}s} &\leq \sum_{u \in \mathcal{N}_v} J \big(\big| \langle \psi| \, a_v^\dagger a_u \, |\psi\rangle \big| + \big| \langle \psi| \, a_u^\dagger a_v \, |\psi\rangle \big| \big) \\
&\leq 2J \sum_{u \in \mathcal{N}_v} \sqrt{N_v(s) N_u(s)}
\end{aligned}$$

$$\implies \frac{\mathrm{d}\sqrt{N_v(s)}}{\mathrm{d}s} \leq 2J \sum_{u\in\mathcal{N}_v} \sqrt{N_u(s)}$$
$$\implies \sqrt{N_v(s)} \leq 2Jd\sqrt{P}s \tag{C.2}$$

in which d is the maximum number of couplings at each site (i.e. degree of the photonic graph $\mathcal{G}$). Inserting Eq. C.2 into Eq.C.1, the proof will be complete:

$$\| |\psi(T_{\text{on}})\rangle - |\psi_\chi(T_{\text{on}})\rangle \|^2 \leq 2J\sqrt{P} \int_0^{T_{\text{on}}} \sum_{v\in\mathcal{N}_u} 2Jd\sqrt{P}s \,\mathrm{d}s \leq 2J^2d^2PT_{\text{on}}^2 \tag{C.3}$$

To ensure that the distance does not grow as a function of P, the evolution time should scale as $T_{\text{on}} \propto \frac{1}{\sqrt{P}}$. This choice ensures that, for short durations of T_{on}, the diffusion of photons to other sites can be neglected. Thus, by measuring the phase, we can determine the value of the non-linearity. The measurement operators are given by:

$$\hat{O}^c = |P\rangle\langle 0| + |0\rangle\langle P|$$

$$\hat{O}^s = j(|P\rangle\langle 0| - |0\rangle\langle P|)$$

These operators yield the cosine and sine of the phase in $|\psi_\chi(T_{\text{on}})\rangle$, respectively, upon measurement.

Lemma 3 *The expectation value of the measurement operator $O \in \{O^s, O^c\}$ on the state $\frac{1}{\sqrt{2}}(|\psi_\chi\rangle + |0\rangle)$ can be obtained to a precision ϵ_3, with probability $1-\delta$:*

$$\left| O_k - \langle O \rangle_{\psi_\chi} \right| \leq \epsilon_3 \quad , \quad \epsilon_3 = 2\epsilon_2 + \frac{1}{\sqrt{\delta k}}$$

where O_k represents the average outcome of k measurements of O on the state $\frac{1}{\sqrt{2}}(|\psi\rangle + |0\rangle)$.

Proof: With a probability of at least $1-\delta$, we can derive the following using Chebyshev's inequality:

$$\text{Prob}(\left| O_k - \langle O \rangle_{\psi} \right| \leq \frac{1}{\sqrt{k\delta}}) \geq 1 - \delta \tag{C.4}$$

using the triangle inequality:

$$\left| O_k - \langle O \rangle_{\psi} \right| \geq \left| O_k - \langle O \rangle_{\psi_\chi} \right| - \left| \langle O \rangle_{\psi} - \langle O \rangle_{\psi_\chi} \right|$$

By using the result in Eq.C.3, and $\left\|\hat{O}\right\| = 1$,

$$\left|\langle O\rangle_{\psi} - \langle O\rangle_{\psi_\chi}\right| \leq 2\|O\|\||\psi\rangle - |\psi_\chi\rangle\| = 2\epsilon_2$$

Inserting this into Eq.C.4:

$$\text{Prob}(\left|O_k - \langle O\rangle_{\psi_\chi}\right| \leq \epsilon_3) \geq 1-\delta \quad , \quad \epsilon_3 = 2\epsilon_2 + \frac{1}{\sqrt{k\delta}}$$

which completes the proof. Note that we interpret O_k as sine or cosine of $(\mu P + \theta_P \chi_{\text{est}})$, with χ_{est} as the estimation of χ.

Lemma 4 *Considering the bounds:*

$$|\cos(\chi_1\theta) - \cos(\chi_2\theta)| \leq \epsilon_3 \quad , \quad |\sin(\chi_1\theta) - \sin(\chi_2\theta)| \leq \epsilon_3$$

imply the upper limit on the difference between χ_1 and χ_2:

$$\theta|\chi_1 - \chi_2| \leq 4\epsilon_3$$

It should be noted that ϵ_3 must be less than $1/4$.

Proof: If ϵ_3 is small enough, then either $|\cos(\chi_2\theta)| \leq 1-\epsilon_3$ or $|\sin(\chi_2\theta)| \leq 1-\epsilon_3$.

Suppose the case where $|\sin(\chi_2\theta)| \leq 1-\epsilon_3$. We define $\varrho_i = \cos(\chi_i\theta)$. Then we can conclude that:

$$\chi_1 = \frac{1}{\theta}\cos^{-1}(\varrho_1)$$

$$\theta|\chi_1 - \chi_2| = \int_{\varrho_1}^{\varrho_2} \frac{\mathrm{d}\varrho}{\sqrt{1-\varrho^2}}$$

$$\left|\varrho^2 - \varrho_2^2\right| \leq 2|\varrho - \varrho_2| \leq 2\epsilon_3$$

$$\implies \left|(1-\varrho^2) - (1-\varrho_2^2)\right| \leq 2\epsilon_3 \implies \left|(1-\varrho^2)\right| \geq \left|(1-\varrho_2^2)\right| - 2\epsilon_3 \geq (1-\epsilon_3)^2 - 2\epsilon_3$$

inserting into the first equation we get that:

$$\theta|\chi_1 - \chi_2| \leq \frac{\epsilon_3}{\sqrt{(1-\epsilon_3)^2 - 2\epsilon_3}}$$

Now, if you consider $\epsilon_3 \leq \frac{1}{4}$,

$$\implies \theta|\chi_1 - \chi_2| \leq 4\epsilon_3$$

The same result can be achieved in case $|\cos(\chi_2\theta)| \leq 1 - \epsilon_3$, which completes the proof.

C.0.1 Quantum enhancement protocol

Theorem 1 *Considering the precision ϵ_0 of the coefficients $J_{u,v}$ and μ_u in the linear Hamiltonian, the non-linearity parameter χ can be estimated to a precision Δ, with a probability of at least $1 - 2\delta$, using $O(\Delta^{-2/3})$ photons:*

$$\theta|\chi_{est} - \chi| \leq \Delta \quad , \quad \Delta = 16\sqrt{Pt_{prop}N(d+1)\epsilon_0} + 8\sqrt{2P}JdT_{on} + \frac{4}{\sqrt{\delta k}}$$

where for $P \gg 1$,

$$P \simeq \big(\frac{16}{T_{on}\Delta}\big[\sqrt{t_{prop}N(d+1)\epsilon_0} + \sqrt{2}JdT_{on}\big]\big)^{2/3} \propto O(\Delta^{-2/3})$$

This estimation requires a total of $2k$ measurements, where P photons evolve for a time T_{on}. Here, the graph degree is denoted as d, and J represents the maximum value of the coupling parameters in the Hamiltonian. It is important to note that t_{prop} determines the time to initialize the two-photon state at a site, which is finite. Additionally, $\theta = T_{on}\frac{P(P-1)}{2}$.

Proof: If we apply Lemma 1 twice and Lemma 2 in the case of two photons ($P = 2$), we can derive the following bound on the final wavefunction, which is the one we want to measure the phase of:

$$\||\psi_{\mathrm{f}}\rangle - |\psi_{\mathrm{f}\chi}\rangle\| \leq 2\epsilon_1 + \epsilon_2$$

Now, using Lemma. 3, and 4, we can obtain the precision in χ,

$$\theta|\chi_1 - \chi_2| \leq 4(2(2\epsilon_1 + \epsilon_2) + \frac{1}{\sqrt{\delta k}})$$

which completes the proof.